

Design and laboratory test of a Lorentz force flowmeter for pipe flows

DISSERTATION

zur Erlangung des akademischen Grades

DOKTORINGENIEUR

(Dr.-Ing.)

vorgelegt der

Fakultät für Maschinenbau der
Technischen Universität Ilmenau

von Herrn

Dipl.-Ing. Christian Weidermann

geboren am 28.04.1984

in Pössneck, Deutschland

Gutachter:

1. Gutachter: Prof. Dr. André Thess
2. Gutachter: Prof. Dr. Xiaodong Wang
3. Gutachter: Dr. Dirk Lieftucht

Tag der Einreichung: 19. Dezember 2012

Tag der wissenschaftlichen Aussprache: 28. Februar 2013

Danksagung

Die Ausarbeitung einer Dissertation erfordert viel Durchhaltevermögen, Disziplin und vor allem Nerven. Viele Promotionen im technischen Bereich benötigen vier, fünf oder sogar sechs Jahre bis zu ihrer Fertigstellung. Ein Grund dafür ist der enorme Zeitaufwand, der für einen gut durchdachten Versuchsaufbau entsteht. Häufig kommen unerwartete Rückschläge durch Lieferprobleme, defekte Geräte oder mysteriöse Störungen dazwischen und bremsen den Fortschritt der Arbeit.

Misserfolg ist lediglich eine Gelegenheit, mit neuen Ansichten noch einmal anzufangen. (Henry Ford)

In solchen Situationen haben mir meine Kollegen an der Technischen Universität Ilmenau und bei der SMS Siemag AG stets mit Rat und Tat zur Seite gestanden. Besonders möchte ich mich bei den Mitgliedern des EXIST-Teams: Dr. Rico Klein, Alexander Thieme und Mandy Guttzeit bedanken. In unserem Team herrscht stets ein angenehmes Arbeitsklima. Jeder hat ein offenes Ohr, eine Hand wäscht die Andere und jedes Team-Mitglied ist bereit den Kollegen bei Schwierigkeiten zu unterstützen. Nur durch diese Harmonie innerhalb des Teams, war es möglich, die Promotion innerhalb von drei Jahren abzuschließen.

Ein besonderer Dank gilt auch Dr. Dirk Lieftucht, der mit seiner fundierten praktischen Erfahrung im Stahlwerk maßgeblich zum Erfolg der Industrietests beigetragen hat. Ohne seine Hinweise und Tipps wären wir in viele Fettnäpfchen getreten.

Weiterhin möchte ich mich bei meinem Mentor Prof. André Thess bedanken. Trotz seiner unzähligen Aufgaben als Fachgebietsleiter, konnte ich jederzeit mit Fragen zu ihm kommen. Von ihm konnte ich während

meiner Promotion viel lernen und mich fachlich und persönlich weiterentwickeln.

Darüber hinaus möchte ich mich bei Michael Werner, Andre Wegfraß und Christiane Heinicke bedanken. Diese Kollegen haben nicht nur die Dienstreisen des Graduiertenkollegs zum Erlebnis gemacht. Auch die Kaffeerunden und Lorentz Biere werden mir in guter Erinnerung bleiben.

Über allem stehen natürlich meine lieben Eltern Thomas und Heike Weidemann. Nur durch ihre Unterstützung konnte ich mich ausschließlich auf mein Studium konzentrieren und im Anschluss zügig die Promotion bearbeiten. Ich denke diese Zeit war ein Nehmen und Geben. Jeder konnte etwas vom Anderen lernen.

In Zukunft müssen sich die Utopien beeilen, wenn sie nicht von der Realität eingeholt werden wollen. (Wernher von Braun)

Kurzfassung

Lorentzkraft-Anemometrie ist ein universelles Verfahren zur kontaktlosen Durchflussmessung elektrisch leitfähiger Fluide. Das Verfahren beruht auf dem Prinzip der Magnetofluidodynamik, welches besagt, dass durch die Bewegung eines elektrisch leitfähigen Materials in einem externen Magnetfeld eine Lorentzkraft entsteht, die der Bewegungsrichtung des Fluids entgegenwirkt. Die Lorentzkraft kann mit Hilfe eines Kraftsensors messtechnisch erfasst und daraus die mittlere Strömungsgeschwindigkeit des Fluids abgeleitet werden. Das Ziel der Dissertation ist es, ein neuartiges Durchflussmessgerät zur kontaktlosen Messung von Strömungsgeschwindigkeiten in Rohren zu entwickeln und im Labor zu testen. Um dieses Ziel zu erreichen, wurde ein theoretisches Modell erarbeitet, welches die Reaktionsgeschwindigkeit des Messverfahrens beschreibt. Weiterhin wurden im Rahmen der Dissertation umfangreiche Designstudien für verschiedene Teilkomponenten des Messgerätes durchgeführt. Unter anderem wurden verschiedene Varianten für Magnetsysteme mittels Finiter Elemente Methode untersucht. Dabei konnte der Halbach-Zylinder mit 16 Segmenten als derzeit effektivstes Magnetsystem gefunden werden. Weiterhin wurde eine umfassende Analyse der thermischen Randbedingungen im Stahlwerk durchgeführt. Das Ergebnis der Studie zeigt, dass eine hinreichende Kühlung des Messgerätes auf weniger als 60°C Innentemperatur möglich ist. Zum Test der Messgeräte und zur Überprüfung der Modelle und Designkonzepte wurden zwei Versuchsstände konzipiert, konstruiert und aufgebaut. Das erste Experiment dient dem experimentellen Nachweis der Reaktionsgeschwindigkeit der Lorentzkraft. Das zweite Experiment dient der Kalibrierung der

Messgeräte. In einer umfangreichen Studie wurden die Kalibrierkonstanten eines ausgewählten Systems für unterschiedliche Materialien und Durchmesser der Probekörper bestimmt. Über den Rahmen der Promotion hinaus wurde der erste Prototyp eines Lorentzkraft-Anemometers erfolgreich unter Industriebedingungen im Stahlwerk getestet.

Abstract

Lorentz force velocimetry (LFV) is a universal flow measurement method for electrically conducting fluids. The interaction of an electrically conducting fluid with an externally applied magnetic field leads to a force that acts upon the magnetic field generating system and drags it along the flow direction [Thess et al. *New J. Phys.* 9 (2007) 299]. This force linearly depends on the mean velocity of the fluid flow and can be measured using force sensors. The aim of the present study is to carry out the design and laboratory test of a LFF for pipe flows. To reach this goal, a comprehensive design study of different proposals for magnet systems has been performed. A Halbach cylinder is more efficient for generating a strong magnetic field inside the area of fluid flow and increasing the quality of the measured signal. An optimization of the geometry of the Halbach cylinder for a given problem could increase the performance of the magnet system again. In order to measure the mass flux dynamically, it is important to have fundamental knowledge about the time response of the device. In this study, a simplified mathematical model has been developed and an analytical solution for the canonical problem of a sudden jump in the flow velocity has been found. The response time of the device is governed by two characteristic time constants: the electromagnetic time constant τ_{emag} , which depends on the material properties of the fluid and the geometry of the considered problem, and the mechanical time constant τ_{mech} , which depends on force sensors. Two laboratory experiments has been performed to proof the results of the conceptual study and the mathematical model. The first experiment is dedicated toward determining the response time, and the second experiment is for

calibration of the device. The experiments show that the device is feasible for dynamical flow measurement of pipe flows. In the calibration experiment, different materials and geometries have been studied. Moreover, a nonlinear correlation between the diameter of the pipe and the Lorentz force could be observed. An additional industrial test with the first Lorentz force flowmeter for pipe flows has been performed. It seems that flow measurement is feasible, but currently, the signal is heavily disturbed by many influences. Herein, we distinguish among mechanical, electromagnetic, and thermal influences.

Contents

| | |
|---|-----------|
| 1. Introduction | 1 |
| 2. Lorentz force velocimetry | 3 |
| 2.1. Governing equations | 4 |
| 2.2. Theory of Lorentz force velocimetry | 7 |
| 2.3. Current state of research | 8 |
| 2.4. Patent situation | 11 |
| 3. Design of the Lorentz force flowmeter | 13 |
| 3.1. Design and optimization of magnet systems | 13 |
| 3.1.1. Mechanism of magnetic field generation | 14 |
| 3.1.2. Numerical model | 15 |
| 3.1.3. Proposals for magnet systems | 19 |
| 3.1.3.1. Proposal 1: Permanent magnets with iron yoke | 19 |
| 3.1.3.2. Proposal 2: The ring magnet | 22 |
| 3.1.3.3. Proposal 3: Halbach cylinder | 25 |
| 3.1.3.4. Proposal 4: One-sided fluxes or Halbach array | 27 |
| 3.1.4. Optimization of magnet systems for pipe flows . . | 32 |
| 3.1.4.1. Optimization of the ring magnet | 32 |
| 3.1.4.2. Optimization of the Halbach cylinder . . | 35 |
| 3.2. Heat protection and housing | 37 |

| | | |
|-----------|--|-----------|
| 3.2.1. | Requirements for the heat shield | 38 |
| 3.2.2. | Scaling analysis on the estimated heat flux and volume flux of cooling liquid | 40 |
| 3.2.3. | Proposals for cooling systems | 43 |
| 3.2.3.1. | Proposal 1 - Cylinder into cylinder | 44 |
| 3.2.3.2. | Proposal 2 - Bore holes | 47 |
| 3.2.3.3. | Proposal 3 - Cooling pipe | 47 |
| 3.3. | Force measurement system | 50 |
| 3.3.1. | Requirements for the force measurement | 50 |
| 3.3.2. | Dynamics of the force measurement system | 53 |
| 4. | Time response of the Lorentz force | 59 |
| 4.1. | Analytical solution for a canonical problem | 60 |
| 4.2. | Numerical solution using finite difference method | 68 |
| 5. | Laboratory experiments | 75 |
| 5.1. | Experimental investigation of the response time | 75 |
| 5.1.1. | Experimental setup | 75 |
| 5.1.2. | Results and discussion | 77 |
| 5.2. | Experimental investigation of calibration constant | 81 |
| 5.2.1. | Experimental setup | 81 |
| 5.2.2. | Results and discussion | 84 |
| 6. | Plant test | 93 |
| 6.1. | Test of cooling and housing | 93 |
| 6.1.1. | Preparation for the test | 93 |
| 6.1.2. | Results and conclusion | 96 |
| 6.2. | Test of flow measurement | 100 |
| 6.2.1. | Preparation for the test | 100 |
| 6.2.2. | Results and conclusion | 101 |

| | |
|--|------------|
| 7. Summary and outlook | 107 |
| 7.1. Summary | 107 |
| 7.2. Outlook | 109 |
| A. Tables | 113 |
| B. Figures | 117 |
| Bibliography | 123 |
| List of Figures | 131 |
| List of Tables | 135 |
| Nomenclature | 137 |
| Declaration of Originality - Abschlusserklärung | 139 |

1. Introduction

Today, flow measurement is very important in our daily life. A vane anemometer at a petrol station ensures that the payment correlates with the tapped amount of petrol. The water consumption in domestic houses all over the world is measured using any kind of flowmeter to determine the annual amount of tapped fresh water. For these applications, a large variety of different flow measurement techniques are available. Nevertheless, in some industry sectors, flow measurement is still an unsolved problem. Fluids used in the heavy industry often are opaque, aggressive, or extremely hot, and common flow measurement devices cannot withstand these harsh conditions for a sufficiently long time. There is a great interest in flow measurement for liquid metals or semiconductors [1]. In particular, there is an increasing level of automation and control in production plants. However, every feedback control system needs a reference and a measured output to operate. For instance, a mold level control in continuous casting machines actually needs the mass flux through the submerged entry nozzle to operate efficiently. Fluids used in the chemical and pharmaceutical industry require a high purity. Simultaneously, acids or other kinds of fluids are aggressive and corrode parts of the flowmeter or the entire flowmeter. Subsequently, the level of purity decreases drastically. Because of these problems, there is a demand for noncontacting flow measurement techniques. The novel flow measurement technique called Lorentz force velocimetry (LFV) offers for the first time a reliable method for noncontacting flow measurement.

The basic theory of LFV has been previously studied. However, the feasibility of LFV in different metal melts is not sufficiently investigated yet. In particular, the current state of development is still in the early stages for pipe flows. The aim of the present PhD thesis is concerned with the design of a novel Lorentz force flowmeter (LFF) for pipe flows and tests under laboratory conditions. Because a majority of conceivable applications are related to liquid metals and casting technology, the novel flowmeter is designed on the basis of concrete boundary conditions typical for continuous casting of steel. The PhD thesis describes both academic research and industrial product design. After a brief introduction into the physics behind the method, a comprehensive literature study about the current state of research is explained. In chapter 3, the subsystems of a LFF for pipe flows designed according to KEP are discussed. Herein, the dynamics of the measurement method is investigated for the first time. An analytical solution for a canonical case has been obtained and numerical investigations for complex input functions have been done to describe the time-dependent behavior of the Lorentz force and the power dissipation. Then, an important parameter called reaction time T_{98} , which characterizes the dynamical properties of the flowmeter, is found. Moreover, the different subsystems of a Lorentz force flowmeter, namely the magnet system, force measurement system, heat shield, housing and data processing unit, are discussed. In chapter 5, results of the laboratory tests are presented. This chapter describes two different experimental setups: one for the experimental investigation of the reaction time T_{98} and the other for calibration purposes. In addition, chapter 6 describes the results of a plant test, that was performed to test the housing and the heat shield of the flowmeter.

2. Lorentz force velocimetry

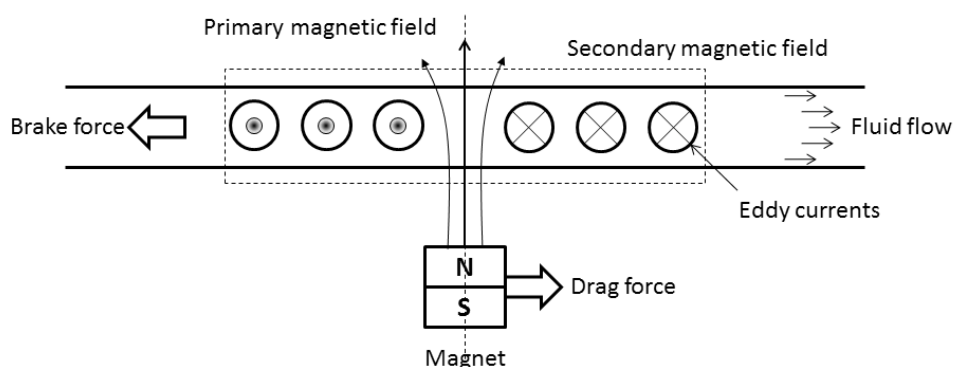


Figure 2.1.: Principle of Lorentz force velocimetry.

Basically, the idea of Lorentz force velocimetry goes back to experiments of M. Faraday and a patent of A. Shercliff. Faraday tried to measure the velocity of the Thames river near Waterloo Bridge in London in 1832 by the use of the earth's magnetic field [2]. Unfortunately, he failed because devices with sufficiently high precision for detecting weak signals were not available then. Of course, today, Faraday's experiment would work because technology has made remarkable progress and accurate devices are commercially available. In fact, the experiment works very well and the principle of an electromagnetic flowmeter is an approved standard in flow measurement. In 1962, A. Shercliff built the first version of a simple magnetic flywheel [3]. Today, we would call it a rotary LFF. Flow velocity can be derived from the angular velocity ω of the flywheel. The basic physics of LFF is classified in the research area

of magnetohydrodynamics. Magnetohydrodynamics is the science for investigating the mutual interaction of magnetic fields with electrically conducting, nonmagnetic fluids [4]. This interaction arises partially as a result of Maxwell's equations, Ohm's law and the Lorentz force acting on the moving conductor [4, 5, 6].

2.1. Governing equations

Maxwell's equations of electrodynamics The equations formulated by Professor James Clerk Maxwell (see Eq.2.1 - Eq.2.4) successfully combine two fundamental interactions in physics, namely, electricity and magnetism. He published his theory of electromagnetism in 1865 [7]. The Maxwell equations are a set of partial differential equations that describe the generation of electric and magnetic fields due to electric charges and electric currents. Moreover, the equations explain the generation of a time varying magnetic field due to a time varying electrical field and the propagation of an electromagnetic wave.

$$\nabla \cdot \vec{E} = \frac{\rho}{\epsilon_0} \quad (2.1)$$

$$\nabla \cdot \vec{B} = 0 \quad (2.2)$$

$$\nabla \times \vec{B} = \mu_0 \vec{J} + \mu_0 \epsilon_0 \frac{\partial \vec{E}}{\partial t} \quad (2.3)$$

$$\nabla \times \vec{E} = -\frac{\partial \vec{B}}{\partial t} \quad (2.4)$$

The first Maxwell equation (Eq.2.1) is known as Gauss's law. The meaning of this equation is that electrical charges are sources/sinks of electrical fields. By using the Gauss integral transformation, we obtain another notation of the equation and conclude that the electric displace-

ment current through the surface of a volume V equals the electrical charge inside this volume. The immediate consequence is that the electrical field lines must not be closed, which allows the existence of electrical monopoles. Moreover, it is a kind of continuity equation in electrodynamics. The second Maxwell equation (Eq.2.2) is called Gauss's law for magnetism and means that there are no magnetic monopoles. The magnetic field lines are always closed because the magnetic field is free of sources. By using the Gauss integral transformation, we notify that the magnetic flux density through the surface of a volume V equals the magnetic charge inside this volume; hence, it is zero because of the first conclusion that there are no magnetic monopoles. The third Maxwell equation (Eq.2.3) is commonly known as Faraday's law of induction. Its physical meaning is significant for many industrial applications, e.g., electric drives, generators, and electromagnetic flowmeters. A change in the magnetic field leads to a field that acts in the opposite direction. The vortexes of the electrical field directly depend on the intensity of the periodic change in the magnetic field. The use of Stokes integral transformation yields the integral notation of Faraday's law of induction. The electrical circulation along the closed curve that defines an area A equals a negative periodic change of the magnetic field. However, note that the equation is also valid for periodically changing areas, because of the relativistic invariance of the Maxwell theory. The fourth Maxwell equation (Eq.2.4) is named as Ampere's law with Maxwell's correction. The vortexes of a magnetic field depend on the free current density and the partial derivation of an electric displacement vector with respect to time. This partial derivative is also referred to as electric displacement current density. By using Stokes integral transformation, we obtain the formulation in terms of the total charge and currents. The physical meaning of this term is that the magnetic circulation along a closed curve that defines an area A equals the sum of an electric current

and the derivation of electrical flux through the area with respect to time [8, 9, 10].

Navier-Stokes equation for incompressible fluids The Navier-Stokes equation is named after scientists Claude-Luis Navier and George Gabriel Stokes. The equation describes the the motion of fluids, and it states the equilibrium between the acceleration of an element of the fluid (left term) and the sum of forces acting on this element (pressure, viscous friction, and, for example, Lorentz force). It is the most important equation in fluid dynamics [11]. Coupled with Maxwell's equations, it is the basis of all models in magnetohydrodynamics [4]. Because it has not been mathematically proven that a solution in three dimensions always exists and that this solution is free of singularity, the Clay Mathematics Institute records this problem in their list of the seven most important open problems in mathematics.

$$\frac{\partial \vec{v}}{\partial t} + (\nabla \cdot \vec{v}) \vec{v} = \frac{1}{\rho} \left[-\nabla \cdot p + \nu \nabla^2 \vec{v} + \vec{f} \right] \quad (2.5)$$

Ohm's law for a moving conductor From Ohm's law for a moving conductor, it is possible to draw conclusions about the induced eddy currents inside an electrically conducting material [12, 13]. It arises from the gradient of the electrical potential and the motion of the conductor in the presence of a magnetic field. Here, σ is the electrical conductivity. For liquid metals, it is of the order of 10^6S/m , and for solids it is of the order 10^7S/m .

$$\vec{J} = \sigma \left[-\nabla \cdot \Phi + (\vec{v} \times \vec{B}) \right] \quad (2.6)$$

Taking the curl of Ohm's law and replacing \vec{J} by Ampere's law yield one of the most important equations in magnetohydrodynamics: the

magnetic induction equation. It is previously known from literature and needs no further discussion [6, 4] in this section. A detailed description of the meaning of the equation is given in chapter 4.

$$\frac{\partial \vec{B}}{\partial t} + (\vec{B} \cdot \nabla) \vec{v} = (\vec{v} \cdot \nabla) \vec{B} + \frac{1}{\lambda} \nabla^2 \vec{B} \quad (2.7)$$

Lorentz force The first derivation of Lorentz force is a question that historians differ about. However, in 1889, Oliver Heaviside derived a vector notation of the force and applied it to Maxwell's equations of electrodynamics. Hendrik Lorentz modified the formula in such a way that the contributions of both electric and magnetic fields are included [14]. Generally, the Lorentz force acts upon a particle of electric charge that moves with a velocity and passes an external electric field and magnetic field. It is a volumetric force, and the magnitude of the vector needs to be determined by integration of $\vec{J} \times \vec{B}$ over the volume of interest [13, 9].

$$\vec{F}_L = \int_V (\vec{J} \times \vec{B}) dV \quad (2.8)$$

2.2. Theory of Lorentz force velocimetry

When electrically conducting materials move across magnetic field lines, eddy currents are induced inside the electrical conductor according to Ohm's law (see Eq.2.6). These eddy currents carry a secondary magnetic field that influences the primary magnetic field. It tends to be deformed because of the motion of the electrical conductor. In consequence, the interaction of the magnetic field with the induced eddy currents generates a Lorentz force that breaks the motion of the electrical conductor (breaking force) and that drags the magnetic field generating system along flow

direction (drag force) [15]. In 2007, Thess et al. investigated the theory of LFV in detail [16]. In the study, they distinguished between a longitudinal flux flowmeter and a transverse flux flowmeter. The longitudinal flux flowmeter uses a single coil to generate an antisymmetric magnetic field whose symmetry axis is parallel to flow direction. On the other hand the transverse flowmeter uses a permanent magnet and the magnetic field is predominantly transverse to flow direction. In both cases, an analytical solution for the Lorentz force density could be found. In the case of the transverse flowmeter, however, it is assumed that a single magnetic dipole exists above an infinitely large sheet with thickness d and electrical conductivity σ . It turns out that an analytical solution exists for this special problem and it is a proven fact that Lorentz force is proportional to the mean velocity of the moving conductor, the electrical conductivity, and the square of the magnetic induction. The calibration factor k is a constant and needs to be determined experimentally or numerically for each application [16, 17].

$$F_L = k \cdot v \cdot \sigma \cdot B^2 \quad (2.9)$$

2.3. Current state of research

The flow measurement technique LFV is a subject of intensive academic research. In 2010, a Research Training Group (RTG) "Lorentz Force Velocimetry and Lorentz Force Eddy Current Testing" that had international participants and that is sponsored by the Deutsche Forschungsgemeinschaft (DFG) was formed at the Ilmenau University of Technology. The RTG involves twelve permanent doctoral students and a various number of associated students. The academic research activities are divided into three groups. Research area A deals with liquid metals; re-

search area B, with electrolytes; and research area C, with solid bodies. Both numerical and experimental investigations are in progress.

The feasibility of LFV for global flow measurement in liquid metals has been successfully demonstrated by Thess et al. [16, 17], Kolesnikov et al. [18], Klein et al. [19] and Weidermann et al. [20]. The possibilities of performing measurements of the local velocity in a turbulent pipe or duct flows have not been investigated extensively. Heinicke et al. [21, 22] have performed a comprehensive set of measurements to investigate the forces and torques acting on a small permanent magnet. In order to realize the specific measurement task, a multi-component force measurement system has been developed by Rahneberg et al. [23]. Here the novel high precision six-degrees-of-freedom force/torque transducer combines a low level of measurement uncertainty with a large amount of dead mass due to the weight of the magnet system.

Nevertheless, Fluid-Magnetic Structure Interaction (FMSI) has not been investigated sufficiently. Fundamental research on this subject has been done by Kirpo et al. [24] and Tympel et al. [25]. Both these groups numerically investigated the interaction of a magnetic dipole with a moving electrical conductor in order to attain an improved understanding of the correlation between the Lorentz force and the position of the magnetic dipole. The work of G. Pulugundla is closer to real applications [26]. He studied numerically the interaction of a liquid metal flow with real geometrically complex magnet systems that are typically used for LFV. Simultaneously, Alferenok et al. and Werner et al. investigated several concepts for sophisticated magnet systems, particularly for LFV in electrolytes [27, 28, 29]. Extensive research activities are going on in the field of LFV in electrolytes. Wegfraß et al. demonstrated the feasibility of LFV in electrolytes for the first time. In their study a special experimental was developed to measure the tiny Lorentz forces

with an order of magnitude of 10^{-6} N for salt water with an electrical conductivity in a range of $2S/m \leq \sigma \leq 8S/m$ [30, 31, 32, 33].

Further, scientists have worked on special modifications of LFV to improve the performance of LFV and eliminate the influence of the electrical conductivity. Vire et al. numerically investigated an LFF that uses time of flight measurements. The Lorentz force is generated by current carrying coils and is measured in time. Autocorrelation or crosscorrelation can be used to determine the flowrate [34]. Jian et al. designed such a device and performed a set of measurements using the time of flight LFV. The feasibility of this special device was experimentally demonstrated [35, 36]. A similar method for noncontacting flow measurement has been developed by Priede et al. [37, 38, 39, 40, 41]. In this method, a rotary single magnet was used to detect the flowrate of electrically conducting liquids. There exists another method based on measurements of the deformation of the induced secondary magnetic field. This method is called flow tomography and has been investigated by Eckert et al. and Stefani et al. [42, 43].

LFV is not restricted to flow measurement. Uhlig et al. used LFV for determining the electrical conductivity of materials [44]. This method is called Lorentz force sigmometry (LFS). It is currently part of fundamental research, but it has a great potential for the investigation of thermophysical properties of liquid metals. Moreover, Lorentz force eddy current testing is another promising application of the method. The Lorentz force is used as an indicator for cracks in solid material [45, 46]. Conventional eddy current testing methods are limited to penetration depth of about 20mm depending on the material. Lorentz force eddy current testing could offer the possibility of detecting deep material defects [47, 48].

2.4. Patent situation

According to patents *DE 33 47 190 A1* (INTERATOM GmbH; has been nonexistent since 1994), *DE 43 16 344 A1* (AMEPA Engineering GmbH), *DE 199 22 311 C2*, and *DE 100 26 052 B4* (both Forschungszentrum Dresden-Rossendorf e.V.), contactless electromagnetic flow measurement methods using primary magnetic fields are available. The induced eddy currents are used to determine the mean flow velocity and the space distributed velocity. All of the methods mentioned above have three disadvantages

1. They are not suitable for measuring slowly moving fluids, because of their low sensitivity.
2. The accuracy of measurement is influenced by electromagnetic noise because the magnetic field sensors are impaired by parasitic fluctuation.
3. Increasing the primary magnetic field does not directly result in a higher accuracy of measurement.

These disadvantages are partially overcome by patents *JP 57199917 A* (Hitachi Ltd), *US 6538433 B1* (MPC AB), and *JP 07181195 A* (Kobe Steel Ltd). Instead of direct measurement of the secondary magnetic field the force generated by the secondary magnetic field is measured. However, despite the several advantages of these patents over the above mentioned, these proposals are not suitable for some special applications in flow measurement. For example, the patent *JP 57199917 A* describes a device that uses a current carrying coil enclosing the pipe. This system is heavy, needs an additional power supply and is difficult to install because of the closed system. The patents *US 6538433 B1* and *JP 07181195 A* operate with any kind of local sensors that measure the

flow velocity in their immediate environment. This is not sufficient for determining the mass flux or volume flux in larger pipes, because the magnetic field of local sensors does not seed the entire pipe. In consequence, the measurement accuracy decreases because the sensitivity depends on the fourth power of the distance to the electrically conducting material. Based on the existing patents the researchers at the Ilmenau University of Technology developed a novel measurement device that overcomes the above mentioned problems (*DE 10 2007 038 653 B3*, *DE 10 2005 046 910 B4*, and *WO 2007/033982 A1*).

3. Design of the Lorentz force flowmeter

This chapter presents the design of a LFF. Each device basically consists of three subsystems, namely, a magnet system, a force measurement system, and a housing. Depending on the application, further subsystems are implemented. In the specific case of continuous casting of steel, an additional cooling system is required because of the extremely high temperatures. Other applications may need a separate data processing unit with monitoring for autarkic devices. From all the listed subsystems, the magnet system is the most important. It is responsible for the quality of the measured signal. An optimization could improve the performance of the device significantly.

3.1. Design and optimization of magnet systems

Magnetism is a physical phenomenon that is only visible in the form of a force acting between magnets, magnetized materials, and moving electrical charges [9, 49]. According to Maxwell's second Equation (Eq.2.2), the magnetic field is divergence-free, which implies no magnetic monopoles and closed lines of force at all time. Hence, the basic magnetic object is a single magnetic dipole [9]. It is possible to calculate the magnetic field of a single magnetic dipole analytically [8].

$$\vec{B}(\vec{r}) = \frac{\mu_0}{4\pi} \left(\frac{3 [\vec{m} \cdot \vec{r}] \vec{r}}{|\vec{r}|^5} - \frac{\vec{m}}{|\vec{r}|^3} \right) \quad (3.1)$$

Assume that the magnetic dipole moment \vec{m} has only one component $m_x \cdot \vec{e}_x$ in the x-direction and the space vector is given by $\vec{r} = x \cdot \vec{e}_x$. It can be shown that the magnetic flux density decreases with the third power of x.

$$B(x) = \frac{\mu_0 m_x}{4\pi x^3} \quad (3.2)$$

This fact is significant for the design of magnet systems. Magnetic systems in practice, for instance, in the casting industry, have large diameters mostly in a range of $160 \text{ mm} \leq D \leq 180 \text{ mm}$. Hence the magnetic flux must be pushed through huge air gaps. Sophisticated magnet system are required to realize a sufficiently strong magnetic field at the inner domain of the pipe. Since Lorentz force is proportional to the square of a magnetic field, the magnetic field contributes the most to the total amount of Lorentz force. The challenge in the design of magnet systems is to maximize the magnitude of the magnetic field at the center of a pipe. Of course, increasing the mass of the magnets leads to a higher magnetic field and consequently to a higher Lorentz force. However, because of practical reasons, the total weight of the magnet system must not exceed 20 kg. Otherwise, it is impossible to lift the magnet system without a crane.

3.1.1. Mechanism of magnetic field generation

In principle, source of magnetic fields can be electric currents and time depending electric fields such as those in coils or magnetic materials such as permanent magnets. Today, static magnetic fields of $3 \cdot 10^7 \text{ A/m}$ can be created in a diameter of $d = 3.2 \text{ cm}$ by using hybrid coils, supercon-

ducting materials, or copper-conducting coils [49]. The strongest commercially available permanent magnets are made of neodymium-ferrite-boron (NdFeB) and have an energy product higher than 320 kJ/m^3 [50, 51, 52, 53]. Each method has its own advantages and disadvantages. Of course, current-carrying coils can produce high magnetic fields, but additional heat is generated because of the electric current in the copper wire of the coil. Further, very high electric currents are necessary to push the magnetic flux inside the submerged entry nozzle (SEN). In contrast, permanent magnets create a static magnetic field without any supply voltage, and consequently, no additional heat is generated. However, the magnetic field cannot be switched off in case of an emergency, as in electromagnets. Magnetic materials such as NdFeB are currently more suitable for application in LFV as electric current carrying coils. To reinforce that decision, permanent magnets can be manufactured in various and complex geometries, and therefore it is easier to design sophisticated flux-guiding magnet systems.

3.1.2. Numerical model

A magnetic dipole is a considerable theoretical model that allows physicists to understand fundamental laws and correlations (see Thess et al. [16]). However, for practical applications, it is not advisable to use analytical formulas for calculating the magnetic field distribution of sophisticated magnet systems. It is more convenient to use finite elements (FE) for investigation and optimization. The finite element method (FEM) is a numerical technique for obtaining an approximated solution of partial differential equations allowing for consideration of complex geometry within the calculation [54, 55]. The commercial software package ANSYS Workbench 14 provides a powerful environment for multiphysics simulations. The tool ANSYS MAXWELL 3D uses finite element analy-

sis (FEA) to solve three-dimensional electrostatic, magnetostatic, eddy current, and transient problems. Within the ANSYS Workbench, fully coupled MHD simulations including turbulent two phase flows are possible. But it is time consuming, it requires a lot of computing power, and the calculation takes ages. Therefore it is strongly recommended to replace the liquid metal by a solid body to estimate the generated Lorentz forces. This approximation is called "The Dry Calibration" of an LFF [56] and is explained in detail in section 5.2. Since Lorentz force linearly depends on electrical conductivity and the mean velocity of the fluid flow, it is possible to achieve identical forces by increasing the electrical conductivity and simultaneously decreasing the velocity.

$$F_{steel} = F_{alu} \quad (3.3)$$

$$\sigma_{st} \cdot v_{st} \cdot B^2 = \sigma_{al} \cdot v_{al} \cdot B^2 \quad (3.4)$$

$$v_{al} = \frac{\sigma_{st}}{\sigma_{al}} \cdot v_{st} \quad (3.5)$$

This simplification enables the replication of the production process in the laboratory and in the numerical model without violating the basic physics. In the numerical model, an aluminum rod (material AlSiMg) with a diameter of $d = 80mm$, a length of $L = 1000mm$ and an electrical conductivity of $\sigma = 22 \cdot 10^6 S/m$ moves with constant velocity v_{rod} through the considered magnet system. According to the transformation law (Eq.3.5) the equivalent moving velocity for liquid steel in the SEN can be calculated. In continuous casting of steel, the mass flux through the submerged entry nozzle is specified by the operators in a range of $2t/min \leq \dot{m}_{steel} \leq 8t/min$ while the machine runs in a steady state. Hence, the mean velocity of the liquid steel can be calculated from the mass flux and the cross section.

$$\bar{v}_{steel} = \frac{4\dot{m}_{steel}}{\pi d^2 \rho_{steel}} \quad (3.6)$$

Liquid steel has an electrical conductivity in the order of $\sigma_{steel} = 0.25 \cdot 10^6 S/M$ [57]. Substituting Eq.3.6 into Eq.3.5 yields the equivalent velocity of $\bar{v}_{rod} \approx 10mm/s$ of the aluminum rod. ANSYS MAXWELL 3D uses a second order ansatz function and tetrahedral elements to solve the given problem. A transient solution type is selected. To reduce the numerical effort, symmetry properties are regarded as far as possible. The element size is restricted by the length to a maximum of 15mm. A mesh study has been performed to ensure that slight mesh changes do not significantly affect the results. Maxwell uses sliding mesh technology in the calculation.

The Lorentz force depends on time during a transient phase, and the governing time constant is given by $\tau = 4\mu_0\sigma d^2/\pi^2$ (see section 4.2). For the considered material properties, τ equals 70ms. Therefore, the simulation time must be longer than τ to obtain a Lorentz force value at steady state. In the numerical model, the simulation time set to $t = 160ms$ with a step size of $\Delta t = 40ms$. This is sufficient to calculate the Lorentz force at steady state after a sudden jump in the velocity at time step $t = 0ms$. The investigation of the transient response would require a higher resolution in time ($\Delta t \leq 10ms$) to resolve the time-dependent behavior. This would drastically increase the numerical effort. The magnetic material is NdFeB with a quality of N52. These magnets have a typical residual induction of $B_R = 1.445T$ and a coercive magnetic field strength of $H_c = 927.5kA/m$ [58].

Every numerical code needs verification or validation based on either an analytical solution or experimental data, or both. Thess et al. provided an analytical solution for a magnetic dipole located above an infinite plate with thickness d (see 3.7) [17, 16].

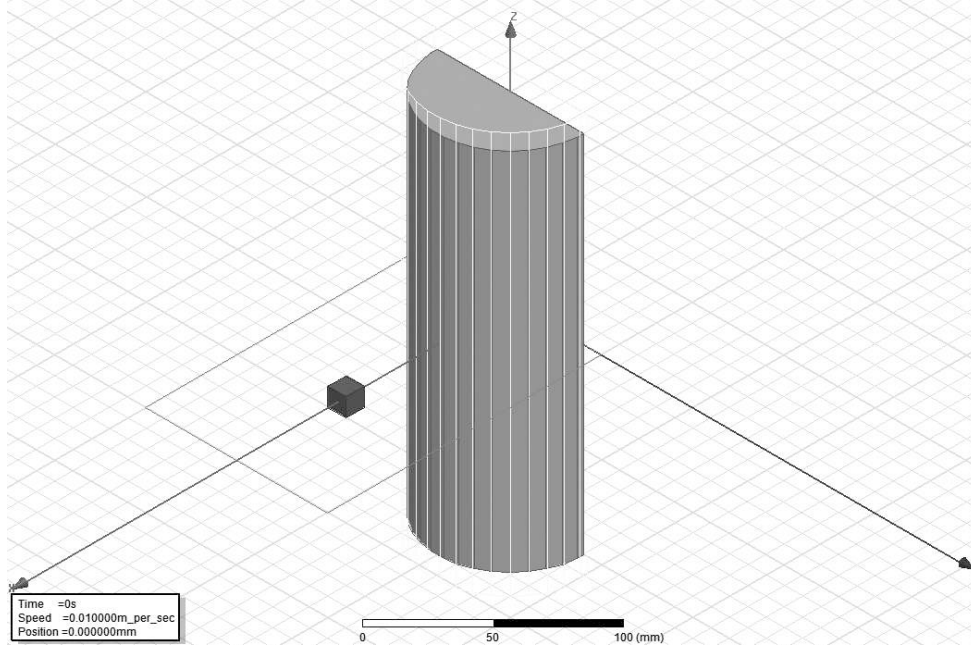


Figure 3.1.: Isometric view of the FEM model. A tiny permanent magnet located at a distance of 85mm above a moving aluminum rod. The aluminum rod has a diameter of 80mm and length of 1000mm. The moving velocity is 10mm/s.

$$F_L = \frac{\mu_2 \sigma v m^2}{128 \pi x^3} \quad (3.7)$$

A magnetic dipole is difficult to implement in FEA because it has no dimensions. However, the theory can be used to validate the FEM code. We assume a tiny permanent magnet with dimensions $10\text{mm} \times 10\text{mm} \times 10\text{mm}$. This kind of permanent magnet has a typical magnetization of $M = 10^6 \text{A/m}$. The magnet is located at a distance of 85mm above a solid aluminum rod (see Figure 3.1). The aluminum rod measures 80mm in diameter and 1000mm in length.

The analytical solution gives a Lorentz force of $F_L = 1.4\mu\text{N}$ and the numerical solution with ANSYS MAXWELL 3D, a Lorentz force of

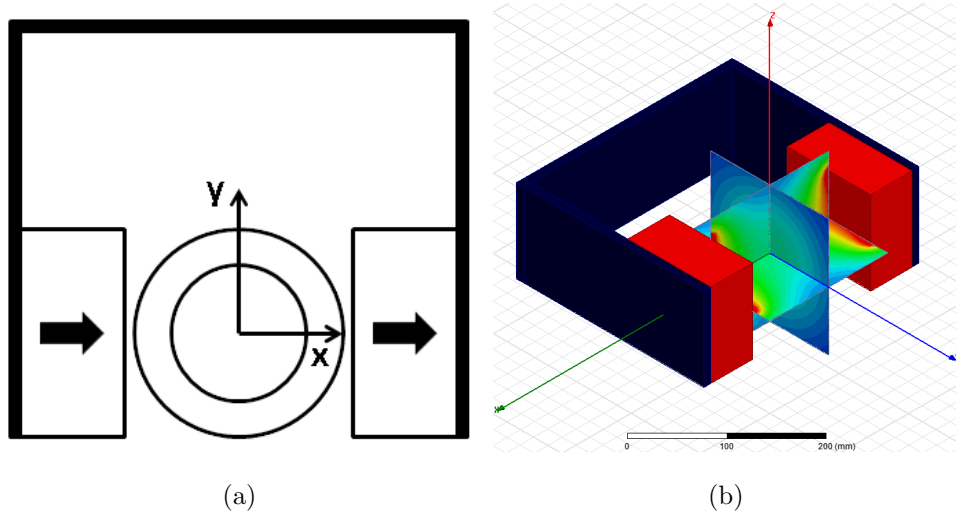


Figure 3.2.: Proposal 1: Permanent magnet with iron yoke. (a) Illustration of proposal 1 including the direction of magnetization. (b) Screen shot of the FEM model. The colored domains indicate magnitude of the magnetic induction.

$F_L = 1.35\mu N$. Both the analytical solution and the numerical solution are of the same order of magnitude, which implies that the numerical model produces considerable results. Slight variations in the mesh size and also in the number of elements do not significantly affect the results. Experiments of C. Heinicke show that tiny permanent magnets considerably match the values calculated with the dipole theory of Thess et al. [22].

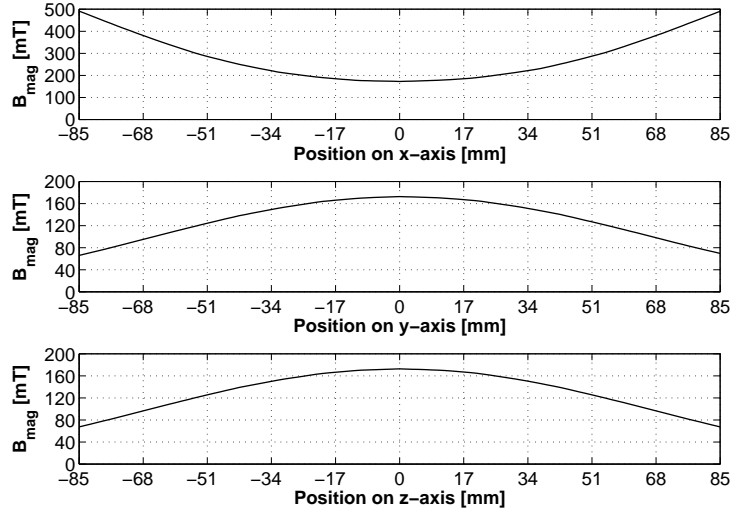
3.1.3. Proposals for magnet systems

3.1.3.1. Proposal 1: Permanent magnets with iron yoke

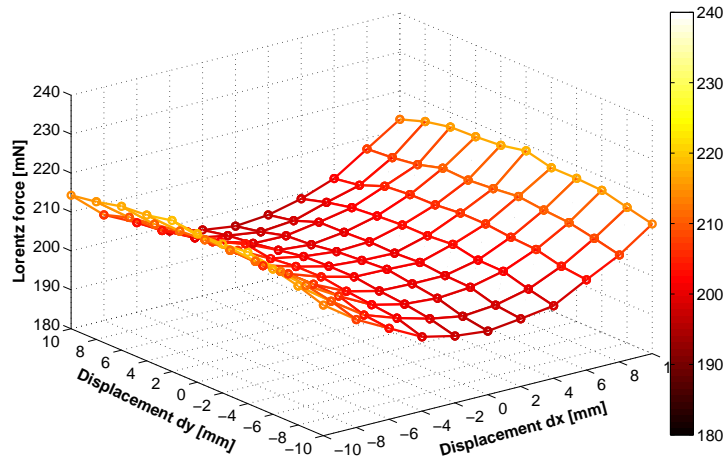
Proposal A uses two permanent magnets and an iron yoke to guide the magnetic flux (see Figure 3.2a). Each magnet has large pol faces of

120mm × 120mm and a thickness of $\delta_{mag} = 60mm$. The direction of magnetization is perpendicular to the large surface. Iron is a good magnetic conductor because of the large relative permeability $\mu_r \gg 1$ [58]. Nevertheless, it loses its properties when the iron reaches saturation. To avoid this effect the iron yoke needs to have large dimensions. The iron yoke has a thickness of $\delta_{iron} = 10mm$. The magnetic field produced by two magnet blocks is roughly twice as large as for one block. Adding a yoke reduces the magnetic resistance of the air effectively to zero and increases the magnetic field roughly by a factor of two. The total weight of the magnet system is given by the sum of all iron parts and all magnetic parts. Therefore the effective magnetic material is less than 20kg in weight. This proposal has only weak potential for optimization. It is possible to vary the geometry or to perform pol shaping, but no significant improvements are expected [29].

With NdFeB magnets with a quality N52, we achieve a magnetic induction of 172mT at the center of the pipe ($x = 0, y = 0, z = 0$). Figure 3.3a shows the magnitude of the magnetic field along the x-,y-, and z-axes. It can be seen that the magnetic field has moderate gradients in all directions. The minimum is located at the center. Proposal 1 generates a Lorentz force of $F_L = 240mN$ while the aluminum rod moves with a constant velocity of $v = 10mm/s$. This proposal needs no additional framework to stabilize the magnets. Magnetic forces of more than $F_{mag} = 2500N$ make the magnets self-adhesive on the iron yoke. Moreover, it is conceivable to design a semi-closed device using two permanent magnets and an iron yoke. The results agree with the results of Stelian et al., and it is a proven fact that magnet systems using an additional iron yoke are suboptimal for LLV because of the high dead load caused by the yoke [59]. Figure 3.3b shows the results of the sensitivity analysis of Proposal 1. In this sense, sensitivity analysis means that the aluminum rod passes the magnetic field with a small offset from



(a)



(b)

Figure 3.3.: Results of the numerical simulation for proposal 1. (a) Illustration of the magnitude of the magnetic induction along the x-, y- and z-axes. (b) 3D plot of the Lorentz force for off-center position dx and dy of the moving rod.

the center. Therefore, the symmetry axis of the rod and the magnet system are not coincident. Here, dx is the displacement of the rod in the x-direction and dy in the y-direction. From Figure 3.3b, it can be seen that the Lorentz force depends on the position given by the displacement vector $\vec{u} = dx \cdot \vec{e}_x + dy \cdot \vec{e}_y$. The center position is located at $dx=dy=0\text{mm}$. The displacement of the rod along $\pm dx$ causes stronger changes in the Lorentz force as a displacement along $\pm dy$. An off-axis position of $dx = \pm 10\text{mm}$ increases the Lorentz force roughly by +7%. In contrast an off-axis position of $dy = \pm 10\text{mm}$ decreases the force roughly by -3%. The dependence between the deviation of Lorentz force and displacement along the x- and y-axes is a highly non-linear effect. A fourth degree polynomial fit seems to be suitable to approximate the correlation in a range of $-10\text{mm} \leq dx \leq 10\text{mm}$ and $-10\text{mm} \leq dy \leq 10\text{mm}$ around the center position (see B.3). Comparing the curve progression of the magnetic induction in Figure 3.3a and the sensitivity curve in figure 3.3b, we assume a direct relation between sensitivity and magnetic field distribution.

3.1.3.2. Proposal 2: The ring magnet

Proposal 2 is called the ring magnet. It has been inspired by a current-carrying coil. The inner radius of the ring R_i is 85mm, and the outer radius R_o is 127.5mm (see Figure 3.4). The ring has a height of $L = 95\text{mm}$ to match the mass restriction of 20kg. The magnet system is completely free of iron, and it is symmetric around the z-axis. As can be seen in Figure (3.4a) the direction of magnetization is perpendicular to the x-y plane.

Figure 3.5a shows the magnitude of the magnetic induction along the x-, y- and z-axes. It can be seen that the minimum of the magnetic flux density $B = 196\text{mT}$ is located at the center of the pipe ($x =$

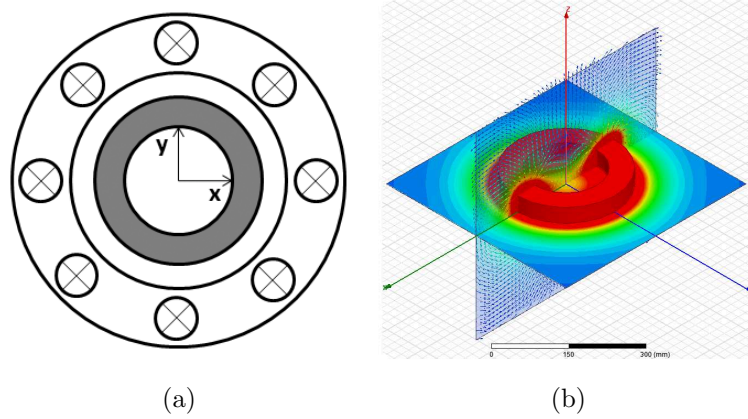
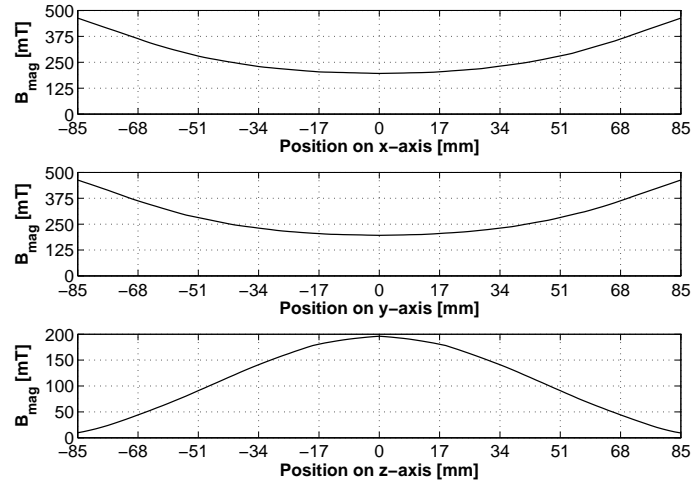
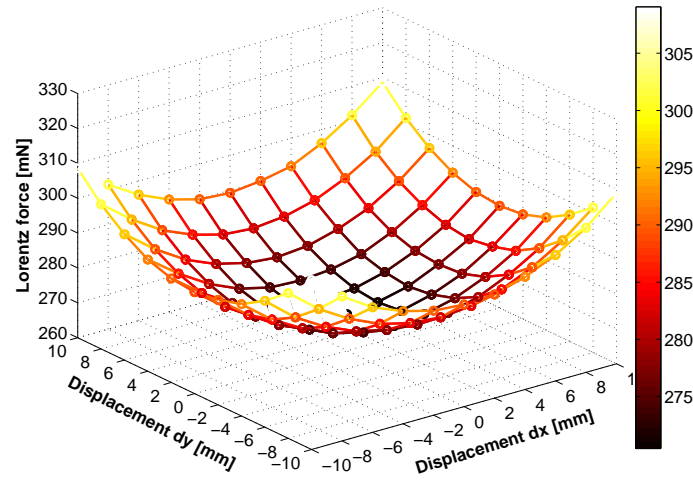


Figure 3.4.: Proposal 2: Ring magnet. (a) Illustration of proposal 2 including the direction of magnetization. The ring is magnetized perpendicular to the x-y plane. (b) Screen shot of the FEM model. The colored domains indicate magnitude of the magnetic induction.

0mm, $y = 0\text{mm}$, $z = 0\text{mm}$). The gradients of the magnetic field in the x- and y-directions are moderate. Stronger gradients can be observed in z-direction. On the z-axes, the maximum of the flux density is located at $z=0\text{mm}$. Proposal 2 produces a reasonable Lorentz force of $F_L \approx 280\text{mN}$. Such large permanent magnet rings are not commercially available and need to be constructed by using either multiple layers of flat discs or segments of a circle. The interaction between the single magnetic blocks causes strong forces of more than $F_{mag} = \pm 5000\text{N}$ during assembly. Basically, the magnets can be bonded. However, because of safety reasons, additional framework is required to stabilize the magnets if the bond cracks. Here, special equipment made of nonferromagnetic material (titanium or surgical steel) is compulsory to work with. Figure 3.5b shows the results of the sensitivity analysis of the ring magnet. It can be seen that a displacement along the x-axis and along the y-axis cause



(a)



(b)

Figure 3.5.: Results of the numerical simulation for proposal 2. (a) Illustration of the magnitude of the magnetic induction along the x-, y-, and z-axes. (b) 3D plot of the Lorentz force for off-center position dx and dy of the moving rod.

deviations in the generated Lorentz force. The Lorentz force increases for all combinations (dx, dy) in a range between -10mm and $+10\text{mm}$. The response surface is a paraboloid of revolution and the Lorentz force generated at the position $dx = \pm 10\text{mm}$ and $dy = \pm 10\text{mm}$ differs by a factor of roughly $+12\%$. Moreover, the correlation between displacement and Lorentz force is highly nonlinear. In this case, a quadratic fit is suitable to approximate the effect (see Figure B.3b). This proposal has a large potential for optimization. For example, the ring can be cut in two single rings, which are aligned parallel along a common axis and magnetized in different directions. If both rings have identical directions of magnetization along the common axis, then the alignment is well known as Helmholtz coil [60]. If the magnetization of the rings is in opposite directions, then the alignment is known as the Maxwell coil [61].

3.1.3.3. Proposal 3: Halbach cylinder

A Halbach cylinder is a special type of magnet system developed and studied by K. Halbach in 1980. The background of this magnet system goes back to experiments with particle beams. For those experiments, Halbach needed to have a very strong and homogenous magnetic field, without using coils to focus particle beams. He found an analytical solution for the distribution of the magnetic field for an infinitely long cylinder [62, 63].

$$B = B_R \ln\left(\frac{R_o}{R_i}\right) \quad (3.8)$$

At least eight symmetrically aligned trapezoidal permanent magnets, which have a typical magnetization pattern (see Figure 3.6a), form a simple Halbach cylinder. The permanent magnets guide the magnetic flux and push it perpendicular to the liquid metal flow through the SEN.

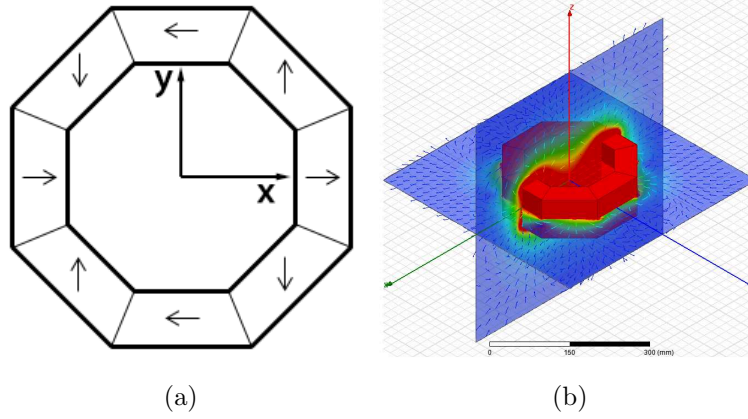


Figure 3.6.: Proposal 3: Halbach cylinder. (a) Illustration of the magnetization pattern of a Halbach cylinder. (b) Screen shot of the FEM model. The colored domains indicate magnitude of the magnetic induction.

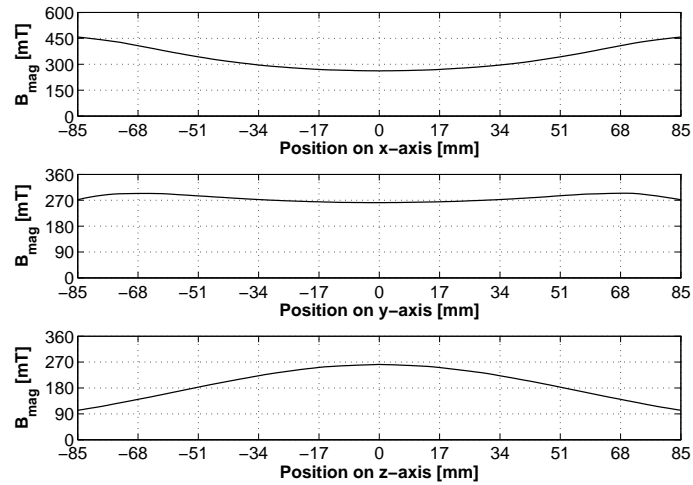
Because there are no air gaps between the magnets only weak magnetic flux leakage occurs. The inner radius of the cylinder is $R_i = 85\text{mm}$ and the outer radius is $R_o = 150\text{mm}$. To match the 20-kg mass restriction, the length of the cylinder is chosen to be 80mm. From FEA, we obtain a magnetic flux density of $B = 261\text{mT}$ at the central position ($x = 0\text{mm}$, $y = 0\text{mm}$, $z = 0\text{mm}$). As can be seen in Figure 3.7a, the magnetic induction shows moderate gradients along the x-axis and strong gradients along the z-axis. Along the y-axis, the magnetic induction is reasonably constant. In particular, in the inner domain of the SEN $x^2 + y^2 = r_{\text{pipe}}^2$, a homogenous magnetic field can be observed. The estimated Lorentz force sums up to $F_L = 402\text{mN}$, which is a reasonable improvement in comparison with the estimates from all other proposals. Halbach cylinders are difficult to assemble. Depending on the size, magnetic forces up to $F_{\text{mag}} \geq 10\text{kN}$ act between the magnets. Special equipment and know-how are required to manufacture such a magnet system. It is ad-

visible to declare it as a bought-in part. For instance, the company Vacuumschmelze Hanau GmbH manufactures such magnet system for renewable energy.

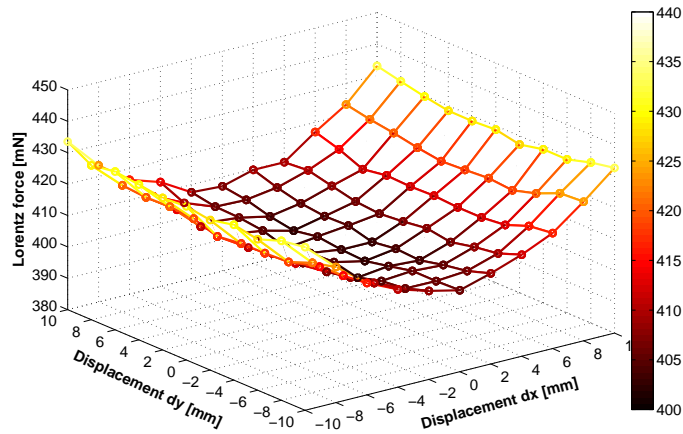
Figure 3.7b shows the results of the sensitivity analysis of proposal 3. It can be seen that the Lorentz force is relatively insensitive towards a displacement along the y-axis. Further, the deviation of Lorentz force along the x-axis is moderate. A displacement of $dx = \pm 10\text{mm}$ roughly changes the Lorentz force by a factor of 7%, and a displacement of $dy = \pm 10\text{mm}$, by a factor of less than 1%. This is a great advantage compared to proposal 1 and proposal 2. From Figure B.4a, it can be seen that a sixth degree polynomial fit is suitable to approximate the sensitivity. This proposal has a large potential for optimization. It is possible to vary the dimensions of the Halbach cylinder and the number of segments. Moreover, it could be interesting to vary the direction of magnetization by an angle ϕ_{mag} in order to find better magnetization patterns.

3.1.3.4. Proposal 4: One-sided fluxes or Halbach array

Proposal 4 is a very special magnet system that guides the magnetic flux only on one side of the magnet system. The effect of one-sided fluxes was described for the first time by J. Mallinson in 1973. He demonstrated that there are magnetization patterns in a planar structure and these patterns realize that all the fluxes exit from one surface with none leaving the other side (see Figure 3.8a)[64]. This configuration is useful for magnetic levitation tracks or improved magnetic clamps [65]. In 1981, K. Halbach also studied this kind of magnet system and from that time, has been named the Halbach array [63, 66]. The configuration used by J. Mallinson or K. Halbach could offer a good magnet system for LFV, because of the one-sided flux. Figure 3.8a shows the proposed Halbach



(a)



(b)

Figure 3.7.: Results of the numerical simulation for proposal 3. (a) Illustration of the magnitude of the magnetic induction along the x-, y- and z-axis. (b) 3D plot of the Lorentz force for off-center position dx and dy of the moving rod.

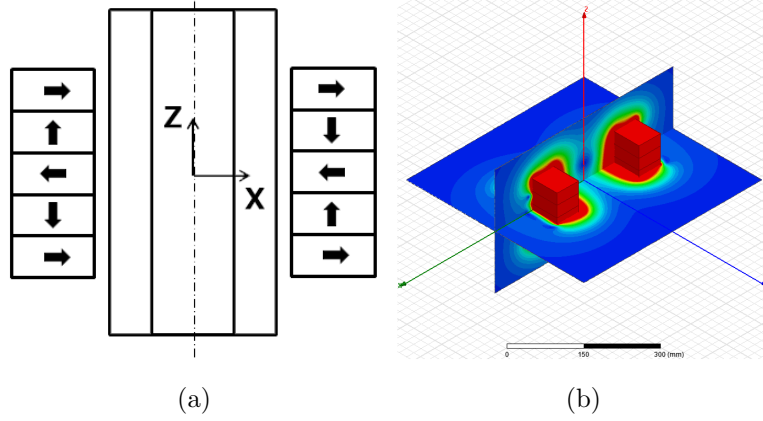


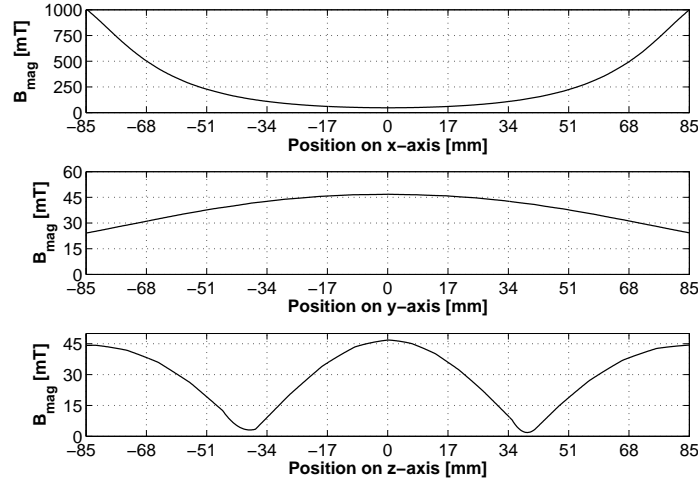
Figure 3.8.: Proposal 4: Halbach array. (a) Illustration of the magnetization pattern of a classical Halbach array as proposed by K. Halbach. (b) Screen shot of the FEM model. The colored domains indicate magnitude of the magnetic induction.

array. One single array consists of five permanent magnets. Each magnet measures $140\text{mm} \times 60\text{mm} \times 30\text{mm}$. The direction of magnetization of each magnet is chosen according to K. Halbach and J. Mallinson and is shown in Figure 3.8a. Two Halbach arrays aligned face to face at a distance $s = 170\text{mm}$ complete proposal 4 (see figure 3.8b).

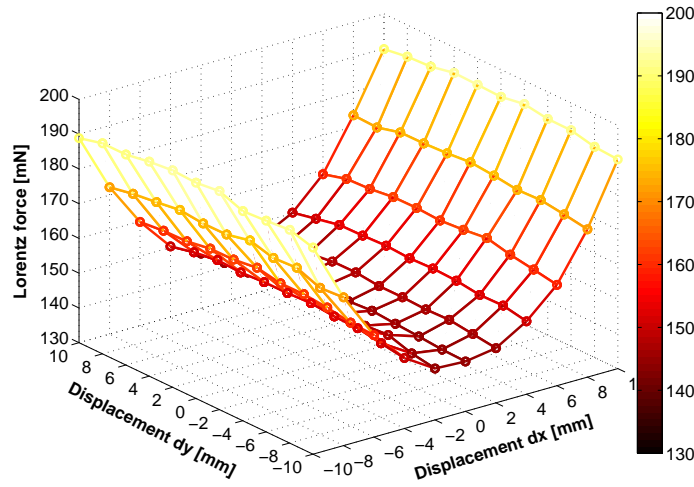
The results of FEA are in agreement with the results of K. Halbach and J. Mallinson. The magnetic flux exits only on one side of the array, and the other side is almost free of magnetic flux. The combination of two Halbach array as proposed, produces a magnetic field distribution with strong gradients in the x- and z-directions (see Figure 3.9a). It should be noted that the magnetic flux density equals zero in the center position at $x = 0\text{mm}$, $y = 0\text{mm}$ and $z = 0\text{mm}$. In the area of fluid flow ($x^2 + y^2 = r_{pipe}^2$), the magnitude of the magnetic field decreases to less than $B = 50\text{mT}$ because of the strong gradients. In the y-direction the magnitude of the magnetic flux density decreases. Along the z-axis,

the magnitude of the magnetic induction alternates. However, proposal 4 produces a Lorentz force of $F_L = 140mN$ and does not match the expectations. This result is astonishing because Halbach arrays have been investigated and suggested by Alferenok et al. and Werner et al. for a rectangular channel with a cross section of $50mm \times 50mm$ [67, 68, 28, 69, 29]. It seems that either the distance s between the Halbach arrays or the dimensions in combination with the magnetic configuration influences the generation of Lorentz force drastically. It is not sufficient to put two Halbach arrays face to face around the pipe. It is important to realize a closed magnetic circuit with sufficiently large distances between the pole faces. Halbach arrays of this size are hard to assemble. The different directions of magnetization leads to strong magnetic force in all direction of space. It needs special equipment and devices to achieve an assembly comparable with those of proposal 2 and proposal 3.

Figure 3.9b shows the results of the sensitivity analysis of proposal 4. Here, it can be seen that the Halbach array is relatively insensitive to a displacement along the y-axis. A displacement of $dy = \pm 10mm$ changes the Lorentz force roughly by a factor of -1% . This means the Lorentz force decreases because the magnetic field weakens in the y-direction. In contrast, there is a very strong influence on the Lorentz force along the x-direction. A displacement of $dx = \pm 10mm$ increases the Lorentz force drastically by a factor of up to $+23\%$. This is significant and a major disadvantage for practical applications. From Figure B.4a, it can be seen that a fourth degree polynomial fit is sufficient to approximate the sensitivity curve. Proposal 4 might have a potential for optimization. However, because of the restriction regarding the construction space, there is no possibility for further optimization in the present application.



(a)



(b)

Figure 3.9.: Results of the numerical simulation for proposal 4. (a) Illustration of the magnitude of the magnetic induction along the x-, y-, and z-axes. (b) 3D plot of the Lorentz force for off-center position dx and dy of the moving rod.

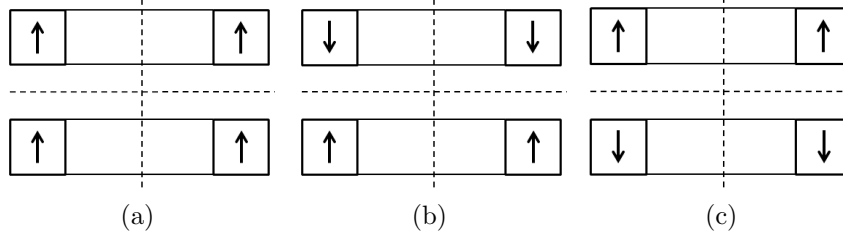


Figure 3.10.: Sketch of the possible magnetization patterns for two single rings. (a) Magnetization pattern of Maxwell coil. (b) Magnetization pattern of Helmholtz coil. (c) Magnetization pattern of inverse Maxwell coil.

3.1.4. Optimization of magnet systems for pipe flows

The results show that all proposals generate a reasonable Lorentz force and would be suitable for LFV. However, proposal 2 and proposal 3 might be the most efficient ones. Both magnet systems have a large potential for optimization. A priori, it is not clear which one produces the highest Lorentz forces. In the present study, a detailed optimization with strong mathematical background is not possible. However, a comprehensive parameter study using finite elements has been performed to elaborate the influence of geometry parameters on the total amount of Lorentz force. The mass is still restricted to 20kg. The magnet system must not exceed a height of $L = 100mm$ and a diameter $D = 400mm$.

3.1.4.1. Optimization of the ring magnet

The ring magnet has an annulus cross section with inner radius R_i and outer radius $R_o = \gamma \cdot R_i$. Here, γ is a nondimensional shape factor defined as the ratio of R_o/R_i . The height of the ring is $L/2$. Then the mass is defined by Eq. 3.9.

$$m_{Ring}(L, \gamma) = \rho_{Mag} \cdot \pi R_i^2 (\gamma^2 - 1) \cdot L \quad (3.9)$$

When R_i is fixed, the parameters γ and L can be varied to achieve an optimal configuration in the dimensions of the ring magnet. Solving Eq. 3.9 for L yields a function $L(k, m)$ that describes the height of the ring depending on the total mass m and the shape factor γ . The mass density of NdFeB is $\rho_{mag} = 7450 \text{ kg/m}^3$ (see material database ANSYS Workbench 14).

$$L_{Ring} = \frac{m_{Ring}}{\rho_{Mag} \cdot \pi \cdot R_i^2 (\gamma^2 - 1)} \quad (3.10)$$

The direction of magnetization \vec{M} has only one component in the z -direction. However, when the ring is cut into half, three different magnetization patterns can be distinguished (see Figure 3.10). The height of each ring reduces to $L/2$, and the rings can be located at $z = \pm s/2$. The first configuration is known as the Helmholtz coil (see Figure 3.10a). Here, the upper and the lower rings have identical magnetization. The second one is known as the Maxwell coil. Here, the magnetization of the upper and lower rings is in opposite directions. The third configuration completes the possible combinations, but it is basically an inverse Maxwell coil. The Helmholtz coil produces a homogenous magnetic field when the distance s between the rings is identical to the mean ring radius $\bar{R} = 0.5 \cdot (R_i + R_o)$. The Maxwell coil produces inhomogeneous magnetic fields with strong gradients [61].

Figure 3.11 shows the results of the parameter study. Two parameters are changed, namely, γ and s . Changing γ automatically includes changes in L and R_o because mass is considered to be constant. In terms of Lorentz force, the Maxwell coil and the inverse Maxwell coil are identical. In contrast, the Helmholtz coil and the Maxwell coil yield

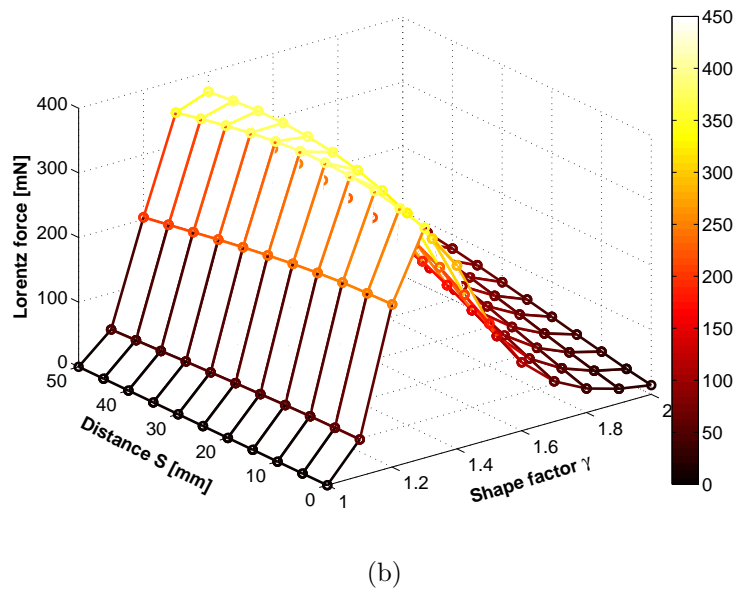
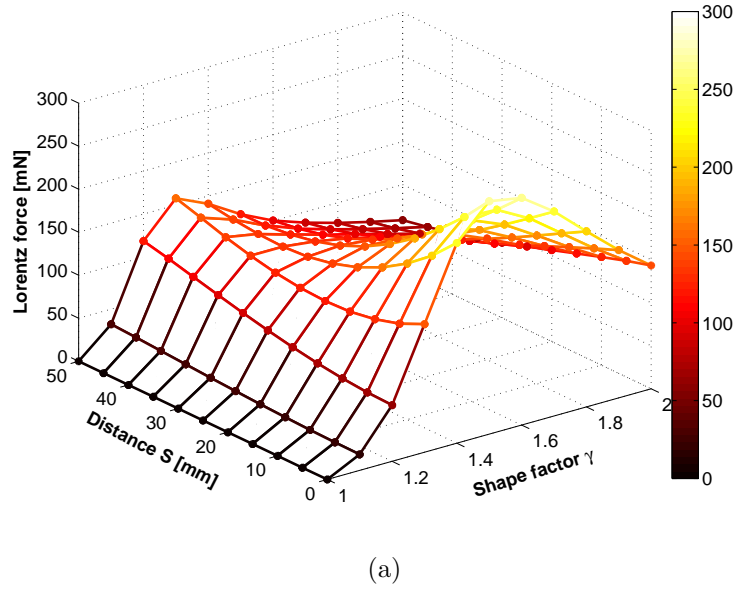


Figure 3.11.: Results of the optimization of proposal 2. The simulations are performed with a velocity of 10mm/s and an electrical conductivity of $22 \cdot 10^6 S/m$. (a) Magnetization pattern of Maxwell coil. (b) Magnetization pattern of Helmholtz coil.

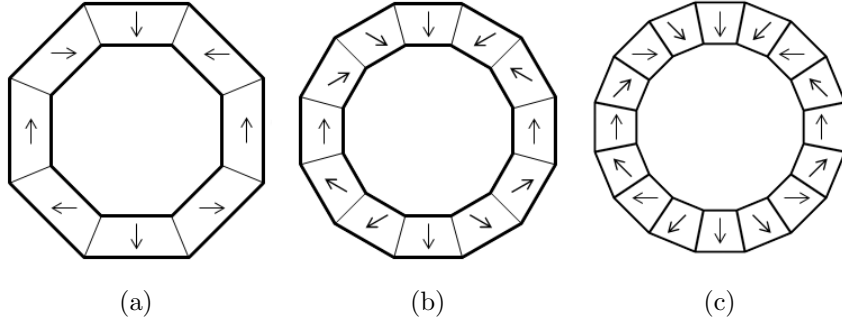


Figure 3.12.: Sketch of the magnetization pattern of Halbach cylinders with different number of segments. (a) Halbach cylinder with 8 segments. (b) Halbach cylinder with 12 segments. (c) Halbach cylinder with 16 segments.

considerably different Lorentz forces. A Maxwell coil arrangement with a shape factor $\gamma = 1.3$ and a distance of $s = 20\text{mm}$ between the rings produces a maximal Lorentz force of $F_L = 384\text{mN}$. In contrast a Helmholtz coil arrangement with a shape factor of $\gamma = 1.5$ and no distance between the rings ($s = 0\text{mm}$) produces a Lorentz force of $F_L = 271\text{mN}$. Nevertheless, the performance of the optimized ring magnet is still lower than that of the Halbach cylinder in proposal 3.

3.1.4.2. Optimization of the Halbach cylinder

Halbach cylinders have a polygonal cross section enveloped from an inner circle with radius R_i and an outer circle with radius $R_o = \gamma \cdot R_i$. Again, γ is a nondimensional shape factor. At least eight trapezoidal segments are required to form a Halbach cylinder, but the number of segments N can vary and may influence the generated Lorentz force. The direction of magnetization \vec{M} of each segment is defined by a vector with x- and y-components, which depends on an angle ϕ_{mag} . In order to maintain the classic magnetization pattern proposed by K. Halbach, the angle

ϕ_{mag} also depends on the the number of segments (see Figure 3.12). The length of the Halbach cylinder is denoted by L . The mass of the Halbach cylinder can be calculated as follows:

$$m_{Halbach}(L, \gamma, N) = \rho_{Mag} \cdot R_i^2 \tan\left(\frac{360^\circ}{N}\right) (\gamma - 1)(\gamma + 1) \cdot L \cdot N \quad (3.11)$$

When R_i and the mass $m_{Halbach}$ are fixed, the parameters γ , L , and N can be changed to find the optimal dimensions of a Halbach cylinder for the considered problem. In order to keep the numerical work at a moderate level, three different configurations, namely, $N = 8$, $N = 12$ and $N = 16$ are considered. Since the basic physics is scale invariance, the optimal value for γ must be valid for all values of R_i . Because of the fixed mass, the correlation between γ and L (see Eq.3.12 is given by

$$L_{Halbach}(\gamma, N) = \frac{m_{Halbach}}{\rho_{Mag} \cdot R_i^2 \tan\left(\frac{360^\circ}{N}\right) (\gamma - 1)(\gamma + 1) \cdot N} \quad (3.12)$$

There are two limiting cases. The first case is $\gamma = 1$, which means that the Halbach cylinder is infinitely large and that the outer radius is identical to the inner radius. The second case is $\gamma \rightarrow \infty$, which means that the length of the Halbach cylinder vanishes and the outer radius becomes infinitely large. Both cases negatively affect the Lorentz force. Figure 3.13 shows the results of the parameter study. It can be seen that the Lorentz force reaches a maximum for a shape factor of $\gamma = 1.5$ for different numbers of segments. An increasing number of segments N seems to positively affect the Lorentz force. The highest Lorentz force of $F_L = 525mN$ could be achieved with a Halbach cylinder that has 16 trapezoidal segments, a length of $L = 92.2mm$, and an outer radius of $1.5 \cdot R_i$. For smaller and larger values of γ the Lorentz force decreases

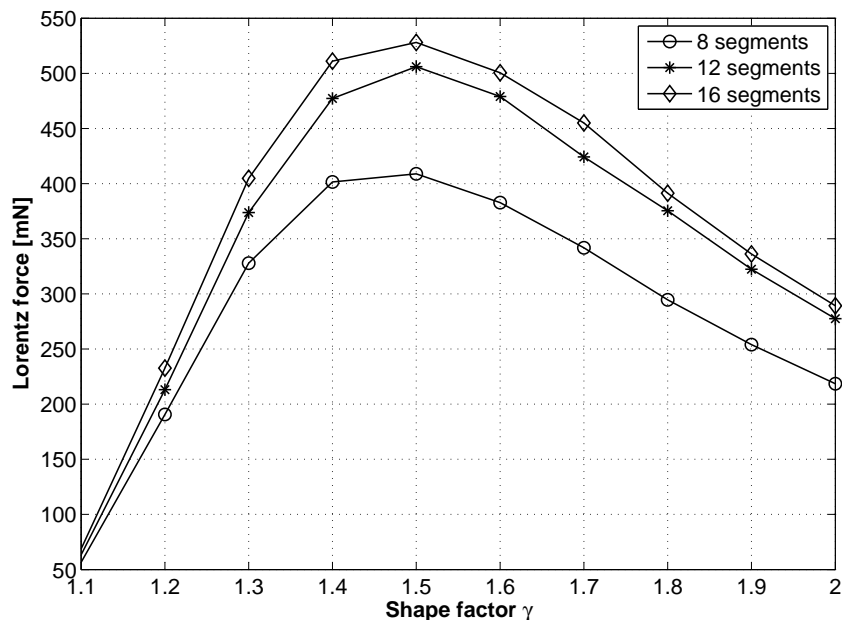


Figure 3.13.: Optimization of Lorentz force generation using Halbach cylinder magnet system. Three magnetization patterns with 8, 12, and 16 trapezoidal segments.

and tends to be zero in the limiting cases of $\gamma = 0$ and $\gamma \rightarrow \infty$. These results agree with investigations of M. Werner and A. Alfernok for a rectangular channel [68][67].

3.2. Heat protection and housing

LFV can be used for flow measurement in any electrically conducting fluid. Here, a large variety of applications are possible, but each production process is individual. Hence, it is impractical to design a universal heat protection system or housing for the device. For example, in continuous casting of steel, the SEN of a thick slab caster measures 180mm

in diameter (including the insulation layer). The surface temperature is in a range of $T_s = 350^\circ\text{C} - 450^\circ\text{C}$ (see Figure 3.14). In contrast, the tube of a dose system for an aluminum die caster measures 160mm in diameter, but the surface temperature is merely $T_s \approx 100^\circ\text{C}$. Therefore, the requirements for a cooling system differ. It seems that some applications require active cooling using pressurized air or water, whereas in other applications, it might be sufficient to use passive cooling via fins. However, the production process with the highest temperatures is the starting point for the design and a benchmark for the performance of the cooling system. Currently, the feasibility of LFV in different industrial applications is under investigation. In continuous casting of steel, high temperatures of more than 1500°C could be observed. In this section, different proposals for cooling systems are investigated with the background of future application in continuous casting of steel. First we elaborate on a simplified model of the thermal situation and carry out scaling analysis to estimate the heat fluxes and the demand of coolant. Subsequently, three proposals for cooling systems are discussed and finally investigated using computational fluid dynamics (CFD) in ANSYS CFX.

3.2.1. Requirements for the heat shield

Electronic devices as well as the permanent magnets have maximal working temperatures. NdFeB-magnets with a quality N52 have Curie temperatures of $T_c = 80^\circ\text{C}$. The single point load cells have service temperatures in a range of $-10^\circ\text{C} \leq T \leq 80^\circ\text{C}$. To protect both electronic components and magnets against overheating, the temperature inside the device should not exceed a maximum value of 60°C . Liquid steel has a temperature of $T_{st} = 1550^\circ\text{C}$. To avoid freezing during the casting process a 20-mm-thick insulation layer is wrapped around the SEN. The

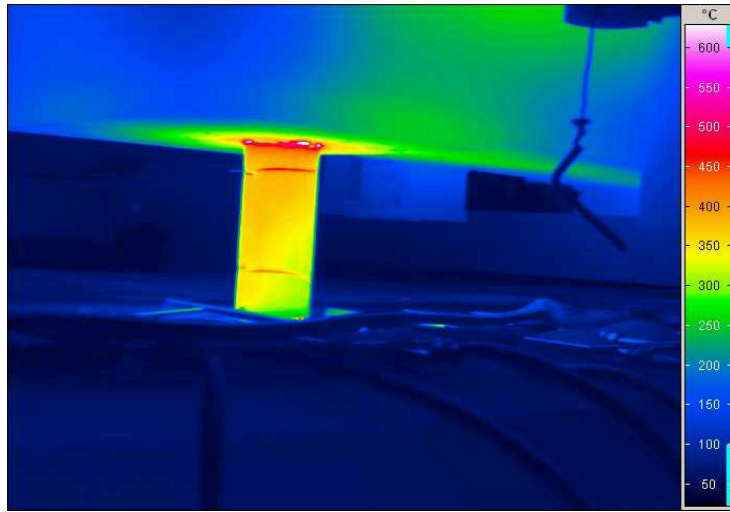


Figure 3.14.: Infrared photograph of a thick slab caster. It illustrates the thermal situation during the casting process.

surface temperature reduces from $T_s \approx 900^\circ\text{C}$ to $T_1 = 450^\circ\text{C}$ (see Figure 3.14). The surface of the tundish has a temperature of $T_2 = 250^\circ\text{C}$. The mold again contains liquid steel but on the top of the mold level, a blanketing material provides a good insulation. The temperature above the mold is around $T_4 = 100^\circ\text{C}$. In conclusion, the highest thermal load during stable caster sequence is caused by the SEN. During the start and end of casting, an increased thermal load is applied to the device because flames burst out of the mold, but this event is temporary. The device is located between the tundish and the mold entry. In this area the coolant can come in contact with liquid steel. For that reason, water, oil, or any other reactive coolant is strictly prohibited for safety reasons. For instance, the reaction of water with liquid steel causes heavy explosions and liquid metal could be discharged from the mold. This poses a safety hazard for foundry men. Therefore the operators request the use of dehumidified pressurized air. The supply is available by default ($T_{air} \approx 20^\circ\text{C}$), and no additional pipes need to be installed. Moreover,

dehumidified pressurized air does not react with liquid steel in the event of pipe leakage. The construction space between the tundish car and the mold entry is restricted. The entire device (including the components for fastening) must not exceed a height of $H = 300\text{mm}$ and a diameter of $D = 500\text{mm}$. Standard fittings employed in a steel plant are used to realize a simple connection to the supply of pressurized air and power supply. This reduces complexity, avoids additional adapters, and makes it easier to implement the device in the existing infrastructure.

3.2.2. Scaling analysis on the estimated heat flux and volume flux of cooling liquid

It is very important to estimate the heat flux going into the device. Therefore, we assume a simple one-dimensional problem and use a thermal equivalent network to describe the given problem. The main source of heat is the submerged entry nozzle. Heat conduction, thermal convection, and radiation have to be considered.

The heat flux through concentric cylinder walls is a classical problem of heat diffusion in cylindrical coordinates. Start with Fourier's law of conduction in cylinder coordinates (see Eq.3.13) [70, 71, 9].

$$\dot{Q} = \lambda A (\nabla \cdot T) = \alpha A \frac{\partial T}{\partial r} \quad (3.13)$$

Here, λ is the thermal diffusion coefficient and it limits the heat flux Q driven by a temperature gradient ΔT . A is the area involved in heat transfer. In the case of a cylindrical body, $A(r)$ can be expressed as

$$A(r) = 2\pi Lr \quad (3.14)$$

If we assume a constant heat flux over the surface, it is possible to

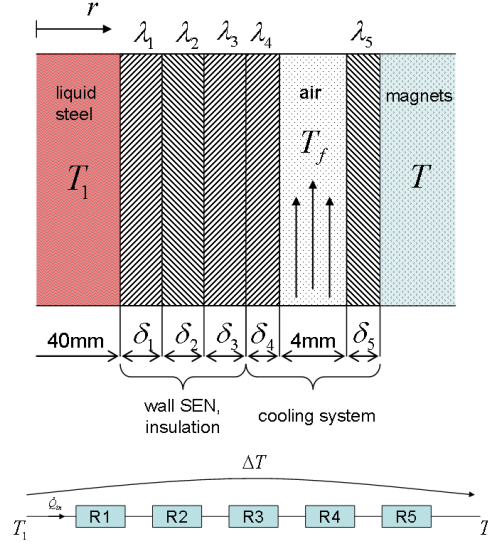


Figure 3.15.: Thermal equivalent network for the cooling of the device. Heat fluxes from the SEN to the device and heat transportation.

integrate over the radius r , and this yields an equation for calculating the temperature as a function of r . Subsequently, the heat flux can be determined from the temperature gradient.

$$\dot{Q} = \lambda 2\pi \cdot L \frac{T_h - T_c}{\ln \frac{R}{r}} = \frac{\Delta T}{R_{hc}} \quad (3.15)$$

This equation is analogous to Ohm's law in electrical circuits. Hence, the thermal resistances $R_1 - R_3$, namely, ceramic wall with thickness δ_1 , ceramic fibre with thickness δ_2 , and insulation layer with thickness δ_3 , can be reduced to one single thermal resistance R_{hc} .

$$R_{hc} = 2\pi \cdot L \sum \frac{\ln \frac{r_k}{r_{k-1}}}{\lambda_k} \quad (3.16)$$

Here, the ceramic wall has a thermal conductivity of $\lambda_1 = 5W/mK$. The ceramic fiber and the refractory coating have a thermal conductivity

of $\lambda_2 = 0.22W/mK$. Hence, the combined thermal resistance is $R_{hc} = 0.999K/W$. Now, the heat flux Q can be easily calculated using the combined thermal resistance R_{hc} and the temperature gradient ($T_h - T_c$) between the liquid steel and the surface of the submerged entry nozzle. The estimated heat flux is about $Q \approx 1200W$.

To realize sufficient cooling, the thermal resistance for convection (R_5) needs to be varied such that the core temperature of the coolant $T_f = 40^\circ C$. The thermal resistance for convection is a function of α .

$$R_{conv} = \frac{1}{\alpha \cdot A} \quad (3.17)$$

Here, the convection heat transfer coefficient α depends on the kind of cooling fluid and the mean velocity of the fluid flow. In particular, α is a function of the so called Nusselt number Nu , which again depends on two non dimensional numbers, namely, the Reynolds number Re and the Prandtl number Pr .

$$\alpha = \frac{Nu(Pr, Re)\lambda}{d} = \frac{1}{R_{conv} \cdot A} \quad (3.18)$$

With this equation, we can derive the required convection heat transfer coefficient and, subsequently, the associated Nusselt number as follows:

$$Nu(Pr, Re) = \frac{d}{R_{conv} \cdot \lambda \cdot A} \quad (3.19)$$

For further calculation, it is important to know the definition of both nondimensional numbers.

$$Re = \frac{v \cdot L_c}{\nu} \quad (3.20)$$

$$Pr = \frac{\eta \cdot c_p}{\lambda} \quad (3.21)$$

The Reynolds number depends on the mean velocity of the fluid flow v , a characteristic length L_c scale, and the kinematic viscosity ν of the fluid. If the Reynolds number exceeds a critical value $Re \geq 2300$ the flow tends to be turbulent [72]. The Prandtl number only depends on the material properties of the fluid, namely, the dynamic viscosity η , the specific heat capacity c_p , and the heat transfer coefficient λ . For air, the Prandtl number is approximately 0.71 [72]. To obtain large Nusselt numbers, a turbulent flow is required. For a turbulent flow, the Nusselt Number can be calculated as [72]

$$Nu(Pr, Re) = \frac{\frac{\xi(Re) \cdot Re \cdot Pr}{8}}{1 + 12.7 \cdot \sqrt{\frac{\xi(Re)}{8}}} \cdot \left(Pr^{\frac{2}{3}} - 1 \right) \cdot \left[1 + \left(\frac{d_a - d_i}{L} \right)^{\frac{2}{3}} \right] \quad (3.22)$$

Here, $\xi(Re)$ is a function that describes the friction and the pressure loss [72].

$$\xi(Re) = [1.8 \log Re - 1.5]^{-2} \quad (3.23)$$

The calculation demonstrates the feasibility of a heat shield for the LFF. If we use dehumidified pressurized air with an initial temperature of $T_0 = 20^\circ C$ as a cooling medium, an average volume flux of approximately 8l/s is required to keep the temperature at a constant level during the casting process.

3.2.3. Proposals for cooling systems

An optimal cooling system for the considered case should have a good insulation layer between the SEN and the cooling liquid. The wall between the cooling liquid and the measurement chamber, which is the area where the electronic devices and the magnets are located, should

have a good thermal conductivity to maximize the heat flux into the cooling fluid.

3.2.3.1. Proposal 1 - Cylinder into cylinder

Proposal 1 consists of two concentric pipes with a thickness of $\delta = 2.5mm$. The inner radius of the first pipe is $r_1 = 100mm$ and the outer radius of the second pipe is $R_2 = 110mm$. The area involved in heat exchange is $A = 0.068m^2$. Between the pipes, there is an air gap of $\delta_{air} = 5mm$ through which the coolant flows. The material of the pipe is aluminum with a thermal conductivity $\lambda_{hc} = 240W/m \cdot K$. This proposal is simple and low budget.

From the results of the numerical simulation, proposal 1 seems to be feasible for cooling the device. However, this proposal produces strong temperature gradients along the perimeter of the inner cylinder (see Figure 3.16). Here, it can be seen that the best cooling is observed in the area around the air inlet. Temperature gradients lead to mechanical stress, which might be influence the measurements. Figure 3.17 gives a good overview about the fluid flow between the cylinders. A jet with preferred direction appears in the upper corner of the cooling system and the majority of air flow passes this way. In the downward direction, there is a merely weak flow of coolant. In consequence, the least cooling is observed in the lower area of the cooling system. At the outlet, the stream velocity is high again, but the cooling performance is poor. This is because the coolant is already heated on the way from the inlet to the outlet. The cooling system is part of the housing and reasonable for the stability of the entire device. Here, proposal 1 has a disadvantage. The thin walls of the pipes are not very solid and the construction tend to oscillate.

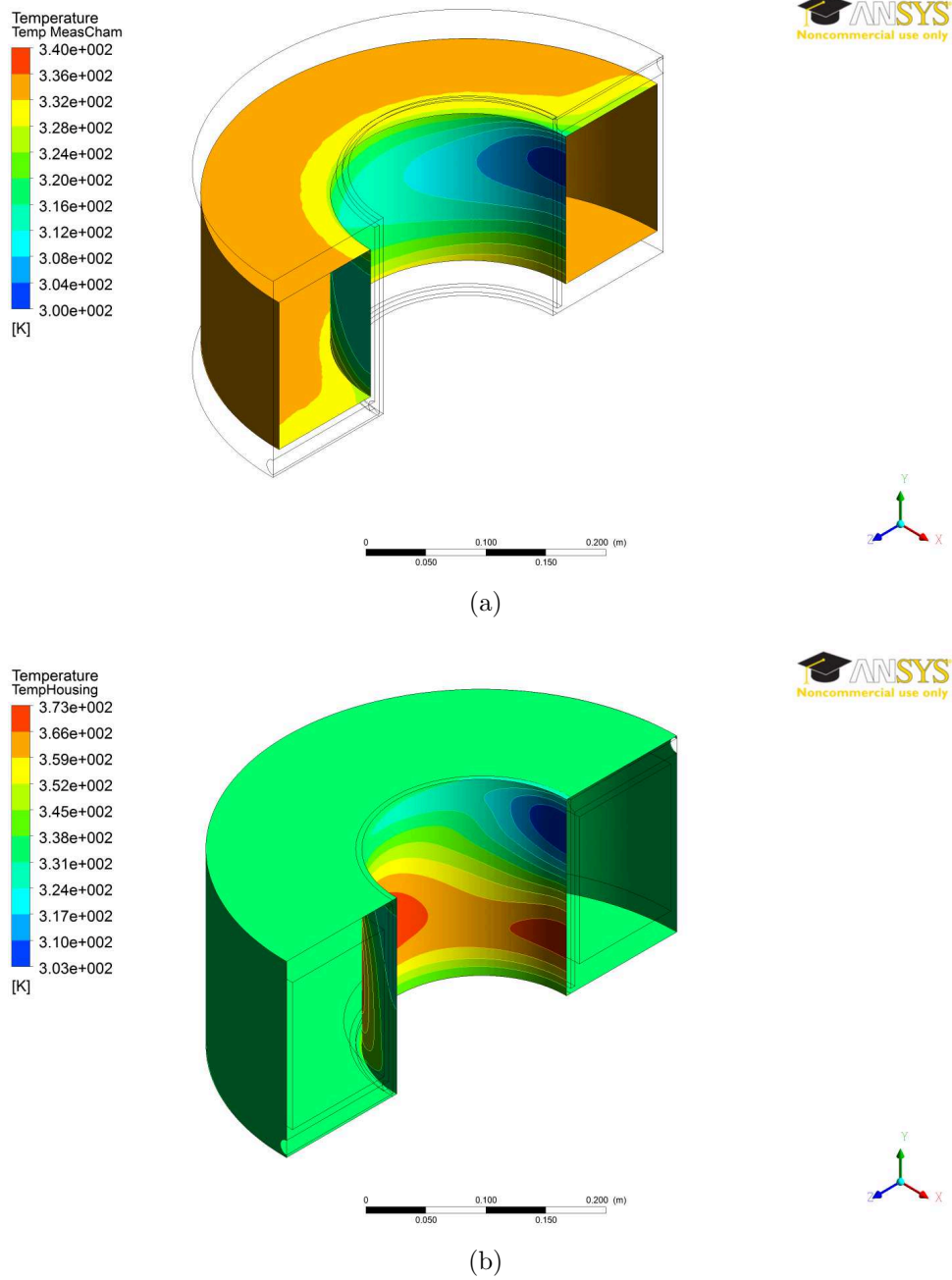


Figure 3.16.: Temperature distribution of proposal 1: (a) Inner areas of the device. (b) Outer area of the device.

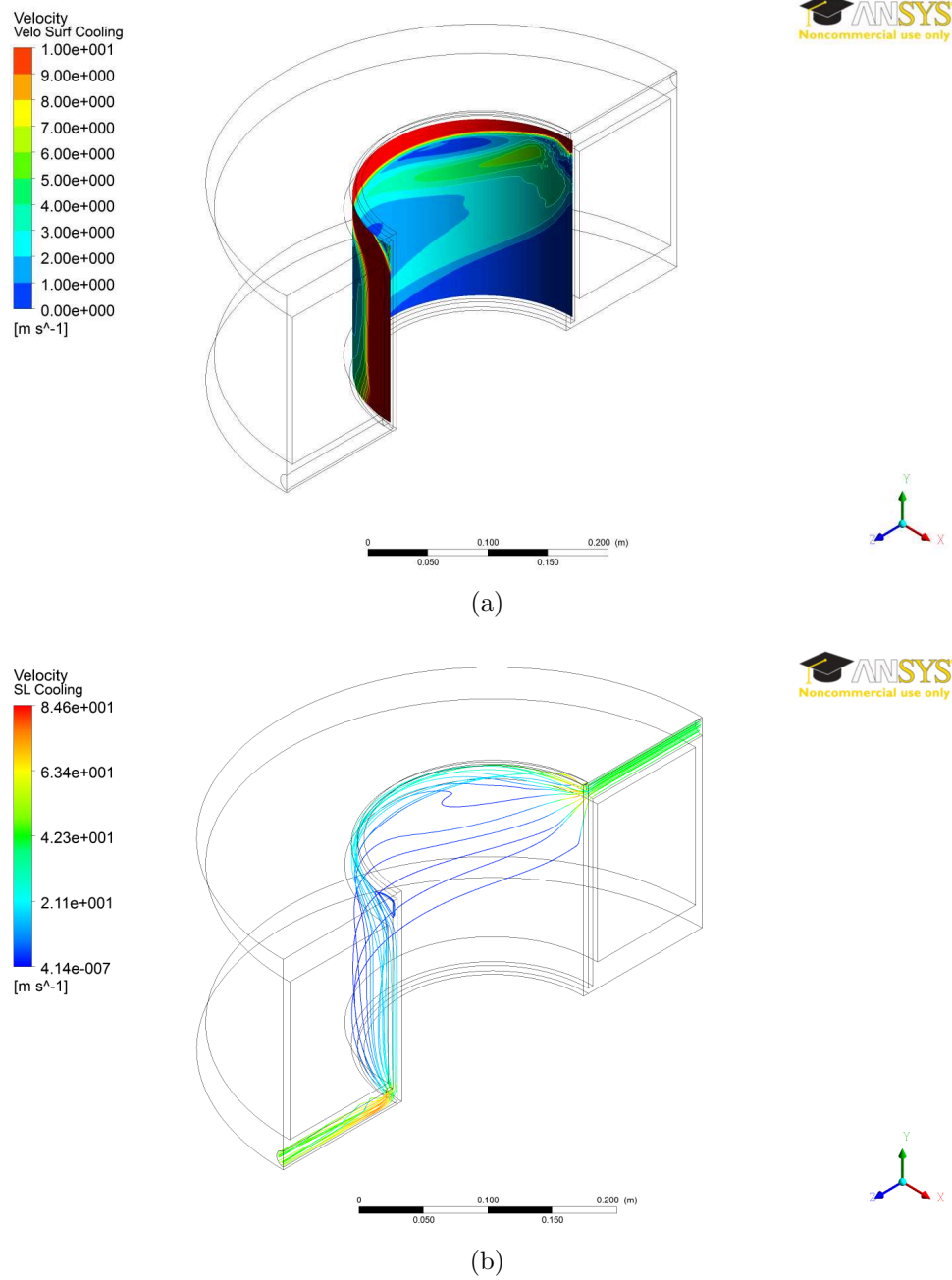


Figure 3.17.: Velocity distribution of proposal 1: (a) Velocity streamlines. (b) Velocity at the middle of the cooling system.

3.2.3.2. Proposal 2 - Bore holes

Proposal 2 is a circular aluminum pipe with an inner radius of $r = 100mm$ and a wall thickness of $\delta = 10mm$. Along the perimeter of the pipe, 36 bore holes with a diameter of $d = 5mm$ are drilled. The coolant flows from the inlet through the long bore holes to the outlet. The surface involved in heat exchange is $A = 0.057m^2$. This is less than in proposal 1, and it can be assumed that the cooling performance is poorer. Because of the large wall thickness of the pipe, proposal 1 provides sufficient stability for the device. However, the performance of proposal 1 is poorer than those of proposal 3 and proposal 2. From the simulation, it can be seen that there is a jet in the supply slot of the cover plate from the inlet to the outlet. The fluid flow in the bore holes near the inlet and outlet is at a moderate level, but there is almost no fluid flow through the bore holes in the middle. In consequence, a hotspot is expected at this position. Proposal 2 seems to be feasible for the application. It is possible to achieve a temperature of $60^\circ C$ inside the device. At the inlet and outlet, we achieve considerable cooling. In the middle, a hotspot occurs with a maximum temperature of more than $70^\circ C$. The temperature differences lead to mechanical stress and, subsequently, to a deformation of the ring. This effect may influence the measurement.

3.2.3.3. Proposal 3 - Cooling pipe

Proposal 3 consists of two parts. The first part is a circular aluminum sheet with an inner radius of $r = 100mm$ and a thickness of $\delta = 2.5mm$, which is part of the housing and separates the device from the SEN. The second part consists of two copper coils with rectangular cross sections of $10mm \times 10mm$, and the wall thicknesses $\delta = 1mm$. Both coils have special alignment. The inlet of the first coil is at the top, and the inlet

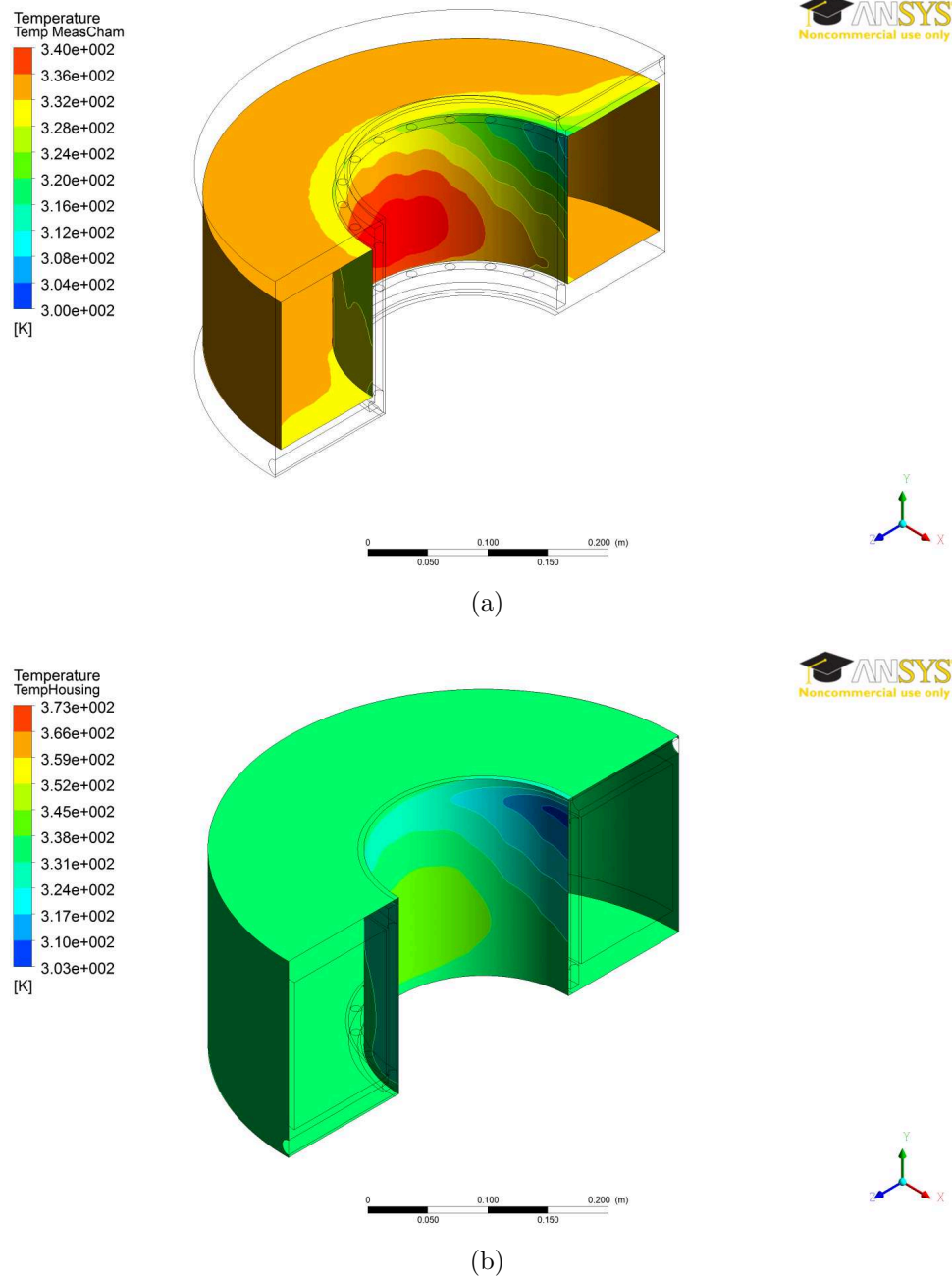


Figure 3.18.: Temperature distribution of proposal 2: (a) Inner areas of the device. (b) Outer area of the device.

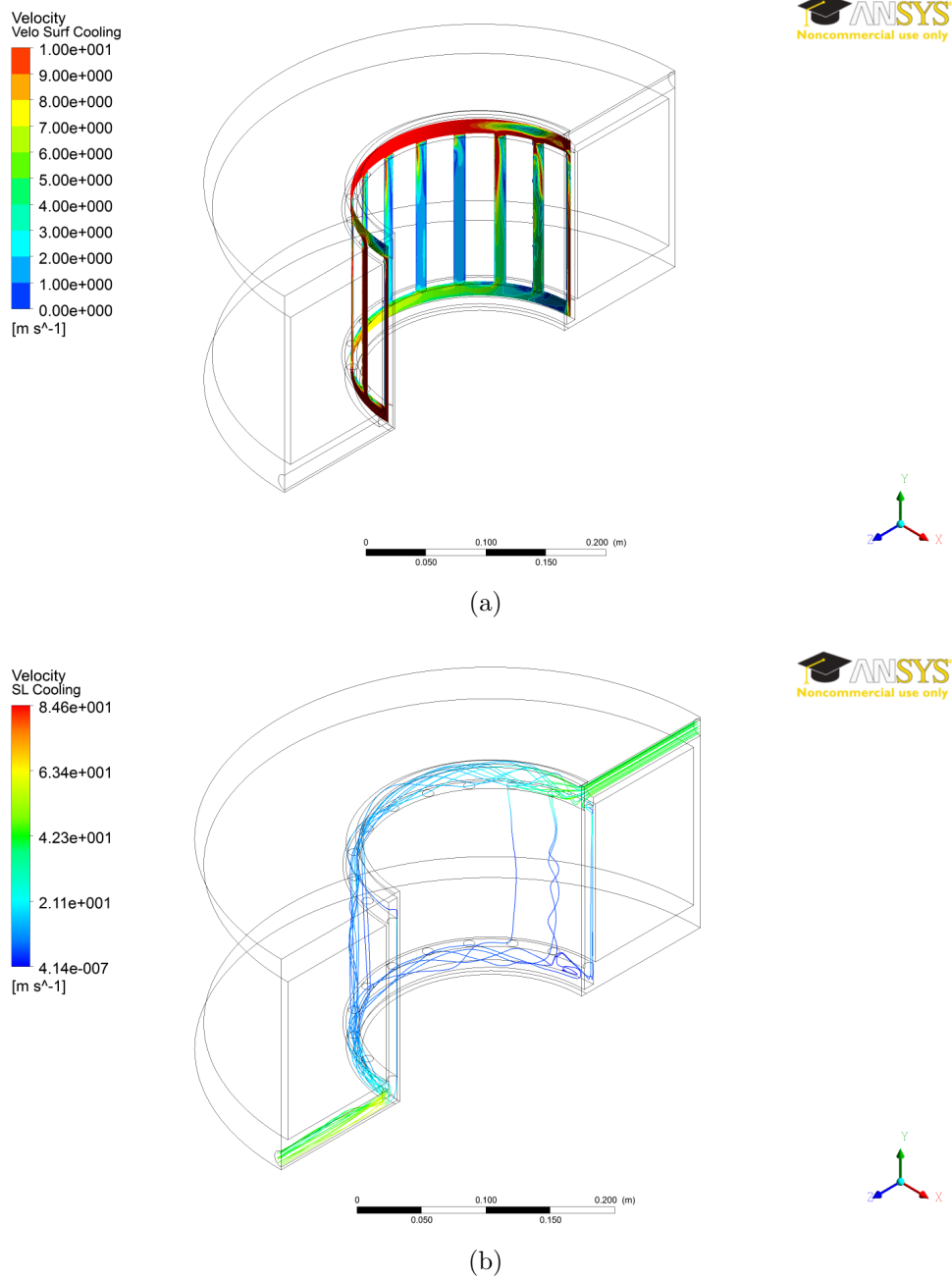


Figure 3.19.: Velocity distribution of proposal 2: (a) Velocity streamlines. (b) Velocity at the middle of the cooling system.

of the second coil is at the bottom. Here, the windings are designed such that the first coil fits into the second. In consequence, both coils result in almost a closed surface. The surface for the heat exchange is $A \approx 0.25m^2$. This system is expected to be the most efficient one. Moreover, we expect lower temperature gradients and a more homogeneous temperature distribution. From Figure 3.21 it can be seen that there is a constant fluid flow inside the coil from the inlet to the outlet. The air enters the device with an initial temperature of $T_f = 20^\circ C$ and heats up to $35^\circ C$ at the outlet. Figure 3.20 emphasizes a homogeneous temperature distribution. The gradients along the perimeter of the inner sheet are weak. Nevertheless, there are temperature gradients in the z-direction because the air heats up from the inlet to the outlet and the cooling performance decreases. Finally, proposal 3 is feasible for the application in continuous casting, too. In comparison with proposals 1 and 2 it is the most efficient one. However, the small aluminum sheet causes the device to have low stability.

3.3. Force measurement system

3.3.1. Requirements for the force measurement

A major challenge is the high dead load ($m = 30kg$) caused by the mass of the magnet system. In contrast, there is a small Lorentz force of $F_L \approx 0.5N$. Keeping in mind that LFV should be used to control the production process and the level of liquid steel in the mold, we find that it is necessary to measure the Lorentz force dynamically and very accurately. Here, a resolution of less than 1% and a response time of $T_{98} = 100ms$ are requested by the operators. It is advisable that the sensor material is nonmagnetic. This implies that there should be no influence on measurement by the external magnetic field. Furthermore

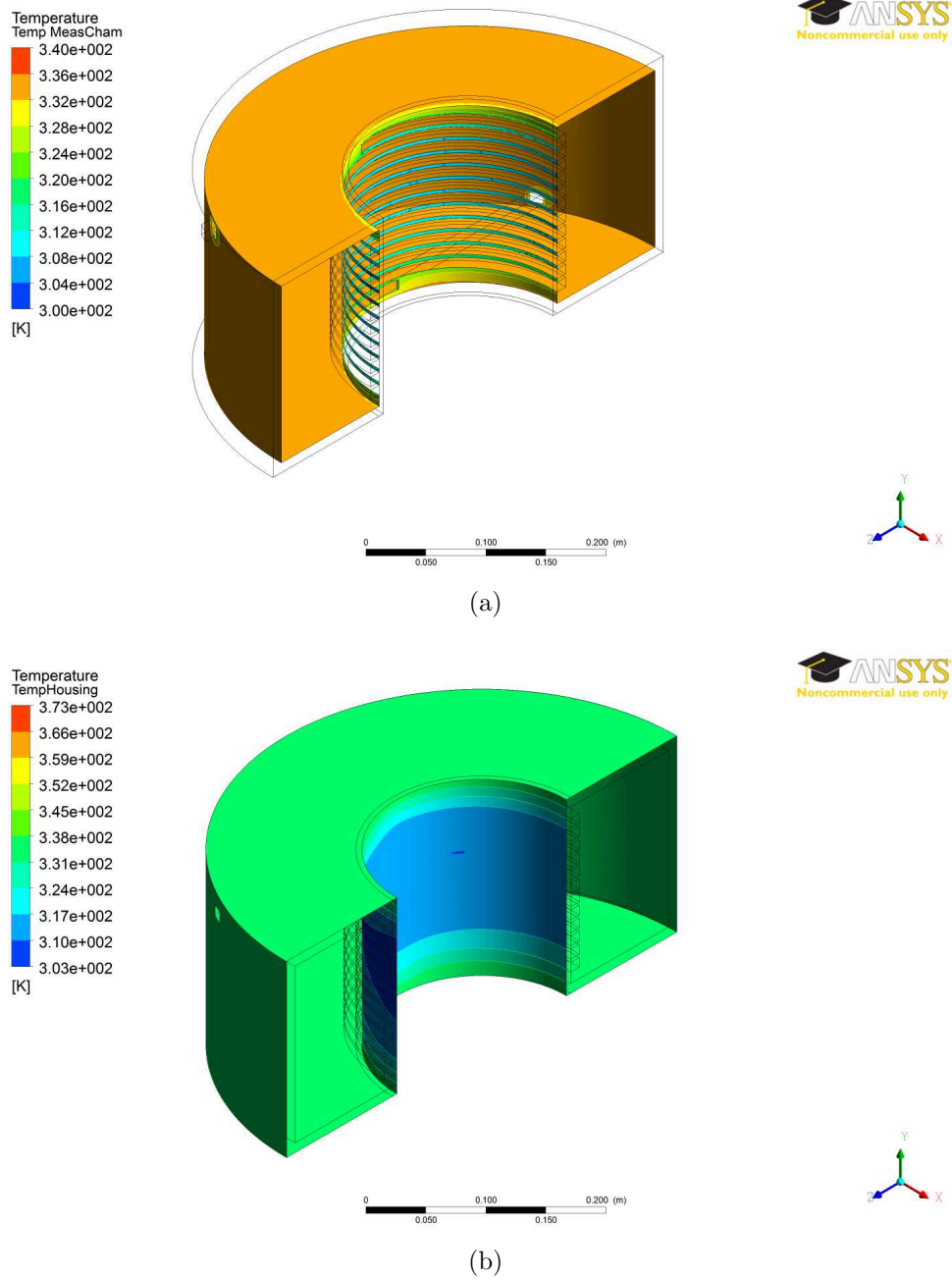


Figure 3.20.: Temperature distribution of proposal 3: (a) Inner areas of the device. (b) Outer area of the device.

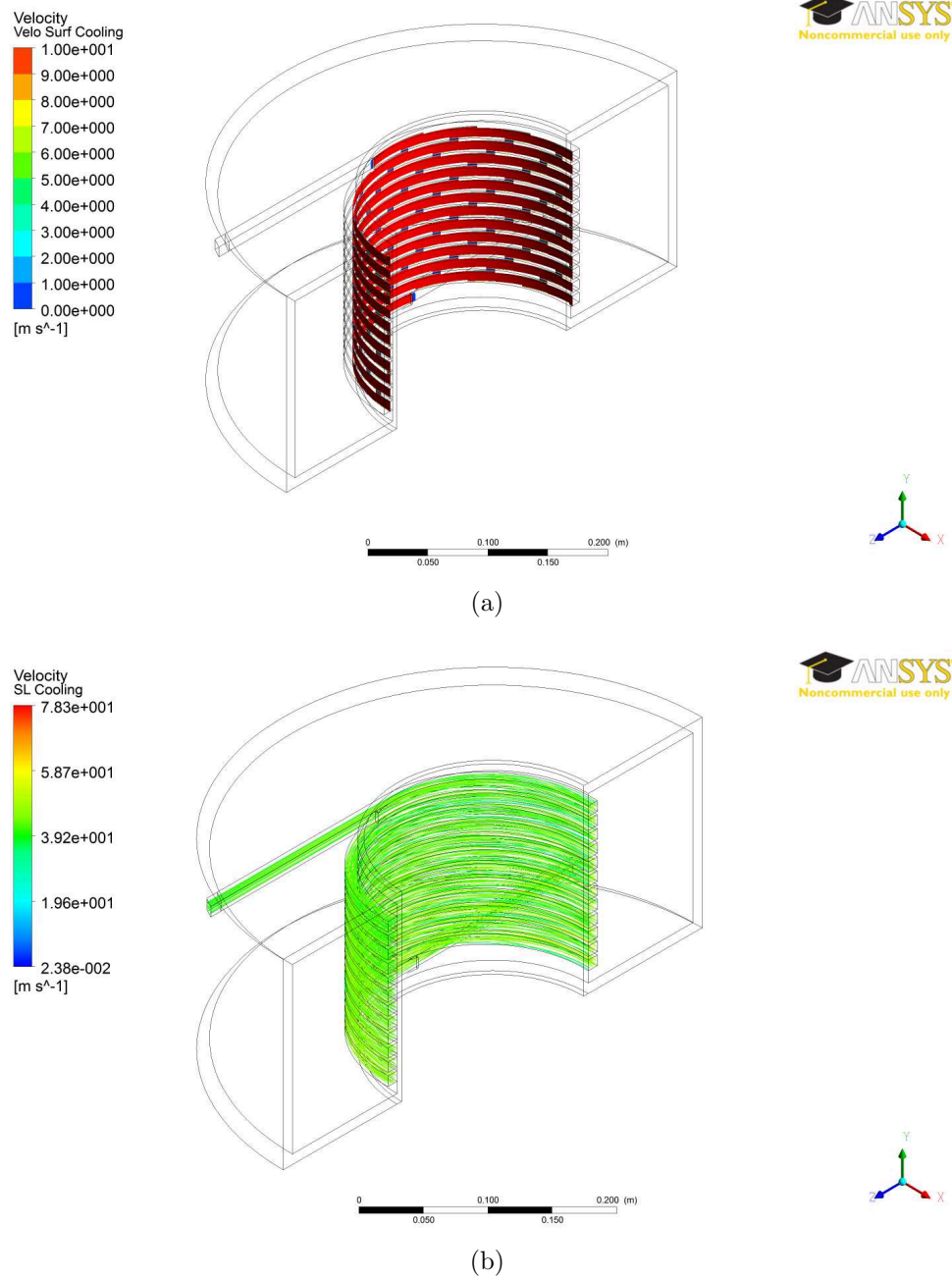


Figure 3.21.: Velocity distribution of proposal 2: (a) Velocity streamlines. (b) Velocity at the middle of the cooling system.

all inductive, capacitive, and piezoelectric sensors could be influenced by the external magnetic field. Hence, only mechanical or optical sensors, i.e., those using a deflection bar and strain gauges to measure the force, are considered. Only sensors made of nonferrous material such as titan, aluminum, stainless steel, or copper beryllium alloys have been considered for the present application in an LFF.

3.3.2. Dynamics of the force measurement system

Force sensors have a typical response time and a characteristic transfer function. In order to classify the response time of the single point load cell, we assume a classical spring-mass-damper system. It is typified by the motion of a mass on a spring when it is subjected to the linear elastic restoring force given by Hooke's Law. A spring is not purely elastic, because of the motion energy dissipated (energy dissipation in the spring and friction). We derive a second-order differential equation to describe the force measurement system. This equation is already known from literature [73].

$$\ddot{x} + \frac{k}{m} \cdot \dot{x} + \frac{c}{m} \cdot x = \frac{F(t)}{m} \quad (3.24)$$

Using Laplace transform, we find the following:

$$F(s) = Lf(t) = \int_0^{\infty} \exp^{-st} f(t) dt = \underbrace{\lim}_{\tau \rightarrow \infty} \int_0^{\tau} \exp^{-st} f(t) dt$$

which yields the transfer function of the system [74]. The system has a transfer function of the second order with the time constants $\tau_1 = \frac{c}{m}$ and $\tau_2 = \frac{k}{m}$. Here, $X_i(t)$ is the input signal and $X_o(t)$ is the corresponding output signal [75, 76].

$$H(s) = \frac{X_o(s)}{X_i(s)} = \frac{\frac{1}{m}}{s^2 + \frac{k}{m}s + \frac{c}{m}} \quad (3.25)$$

The solution of the equation is well known from literature. From Eq.3.25, it can be seen that the motion is sinusoidal in time and demonstrates a single resonant frequency $\omega = \sqrt{\frac{c}{m}}$. To produce reliable measurements, it is advisable to investigate the resonant frequency of the force sensor. If the input signal includes vibrations with a frequency in the range of the resonant frequency of the force sensor, then the sensor starts to oscillate. Consequently, it is challenging or even impossible to measure the Lorentz force. The resonant frequency depends on the applied mass and the elastic properties of the sensor. The higher the spring constant, the higher is the resonant frequency, or the lower the mass, the higher is the resonant frequency. The elastic properties of the force sensor sometimes are specified in data sheets. However, suppliers often do not specify these data in the documentation of their products. Nevertheless, it is advisable to determine the properties of each force sensor experimentally. Figure 3.22 shows the experimental setup used to investigate the properties of a single point load cell (Siemens Siwarex WL260). Here, the load cell is fixed with aluminum profiles on a stiff basement. A special path sensor measures the deflection caused by different standardized weights that are applied to the load cell. According to Hooke's law $F = c \cdot \Delta s$, there is a linear correlation between force and deflection [77] and the slope of the force-deflection curve gives the spring constant c of the load cell. Figure 3.23 shows the measured force-deflection curve of a Siemens Siwarex WL260 load cell. From the measurement data, we obtain a spring constant of $c = 79.79N/mm$ by linear regression.

In a second experiment, the damping factor η has been determined. Here, the same experimental setup (see Figure 3.22) is used. In order to measure the damping factor of the load cell, we induce vibration

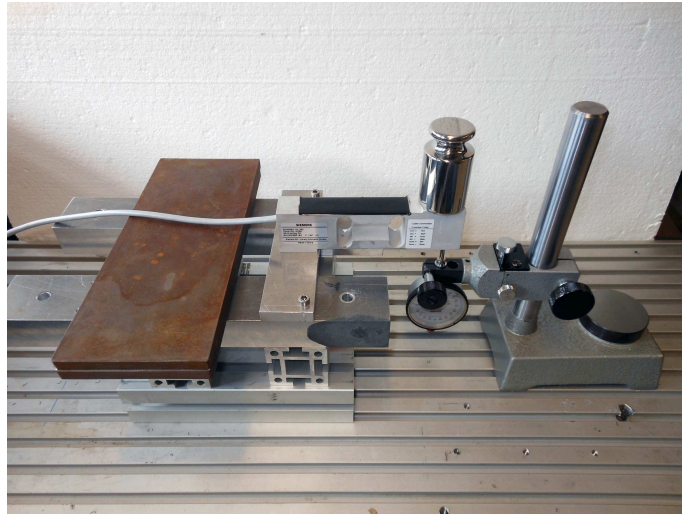


Figure 3.22.: Experimental setup for the investigation of spring constant and damping factor of a load cell.

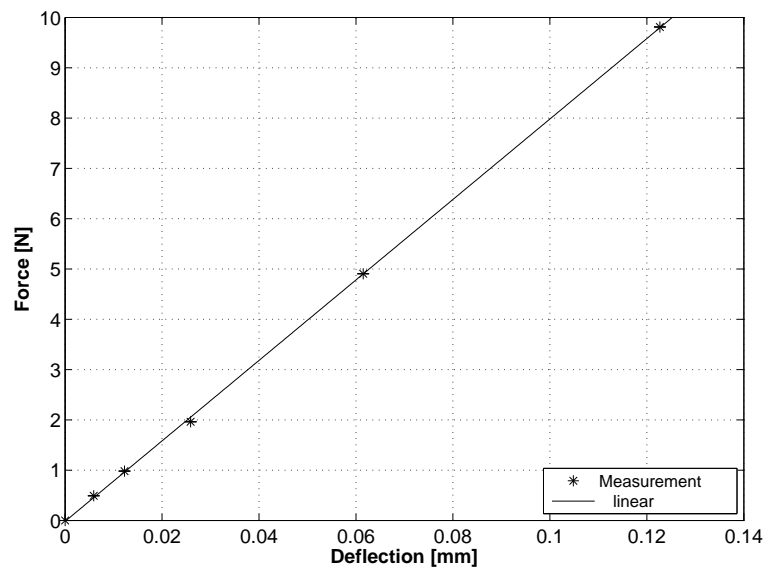
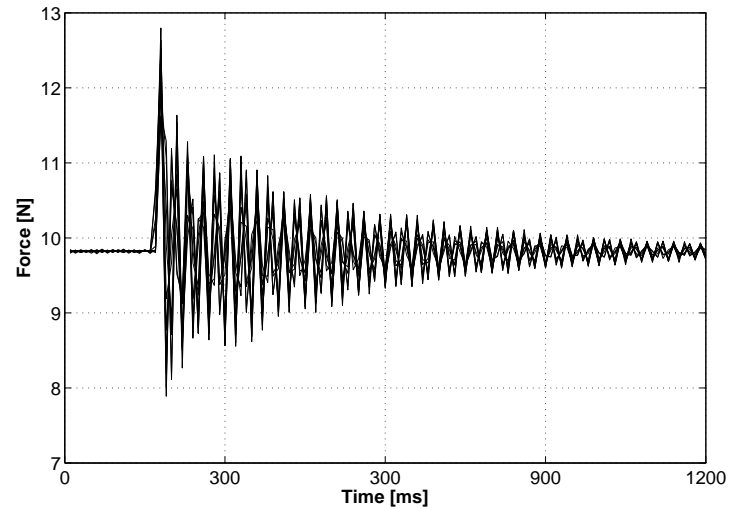
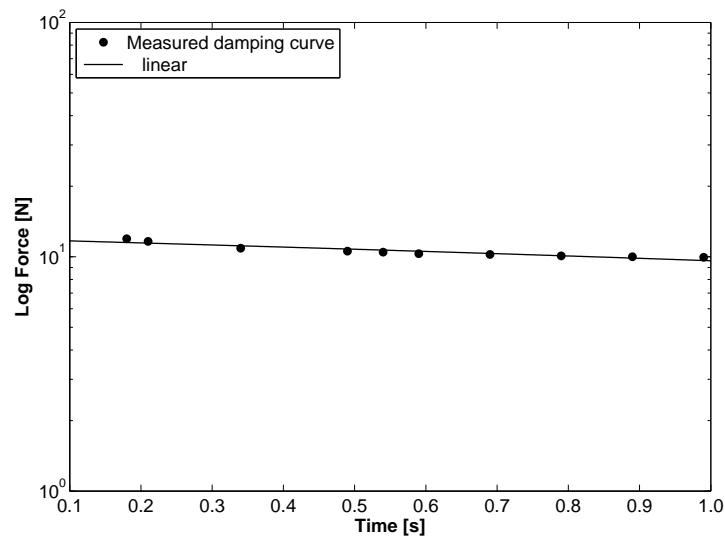


Figure 3.23.: Force-deflection curve of a Siemens SIWAREX WL260 single point load cell.



(a)



(b)

Figure 3.24.: Investigation of the damping characteristics of a Siemens SIWAREX WL260 load cell. (a) Raw data of the measurement drawn all in one plot to demonstrate the good repeatability. (b) Decaying characteristic of the load cell plotted on logarithmic scale.

using the impact of a hammer. The force signal is recorded in time to see the damping characteristics of the sensor. Figure 3.24a shows the results of the measurement for 10 repetitions. As can be seen, there is a good repeatability in the measurement. Plotting the force for several instants of time on a logarithmic scale yields the damping factor $\eta = 2.33 \pm 0.13N/s$.

Because of the symmetry of the present problem, we propose to use three sensors. The weight on each sensor reduces to one-third of the total weight. Moreover, the system becomes redundant. If one sensor breaks down, a signal is still available from other sensors. With three sensors, it also could be possible to detect a off-center position of the device and avoid errors during measurement. A beam load cell has been selected for the cold prototype and laboratory experiments, but in real industrial application, it might be advisable to use round-shaped load cells to reduce construction space.

4. Time response of the Lorentz force

Generally, the interaction between magnetic fields and electrically conducting materials is bidirectional and fully coupled. The intensity of the coupling and the interaction between both is expressed by a non dimensional parameter called the Magnetic Reynolds number Rm . The magnetic Reynolds number can be explained as the ratio of convection of the magnetic field to the diffusion of the magnetic field. For small values of $Rm \ll 1$ magnetic diffusion is dominant. There is almost no deformation of the magnetic field. For large values of $Rm \gg 1$ convection of magnetic field is dominant and magnetic diffusion is weak for instance the earth magnetic field exposed to a solar storm [4, 6, 78, 79, 5].

Parker et.al intensively studied the effect of reconnection of lines of magnetic force in 1966 for a rotating cylinder in an initially uniform magnetic field. He found an analytical solution for a simplified mathematical model and has shown that lines of magnetic force reconnect to form closed loops during the transient phase [80]. Perry et al. investigate the induction of eddy currents in a solid conducting cylinder [81]. All studies are primarily concerned with deformation of the magnetic field due to rotational movement of a cylindrical conductor. But there are only weak contributions regarding the transient of Lorentz force and Joule heat. After intensive literature research there is no scientific contribution that investigates the time-dependence of the Lorentz force and the Joule heat when a moving metal sheet interacts with a uniform magnetic field. It appears that the effect has not been sufficiently studied.

The aim is the investigation of the transient response of the Lorentz force and the Joule heat for different velocity functions of the moving slab. Therefore, we achieve an analytical solution for a canonical problem and apply a finite difference code to obtain the transient response for sophisticated motion setups. The outcome is a characteristic nondimensional time T_{98}^* , called the response time. It is a significant indicator for the dynamics of the flow measurement method of LFV.

4.1. Analytical solution for a canonical problem

In general, the interaction of a magnetic field \vec{B} with an electrically conducting material that moves with a velocity \vec{v} can be described using the magnetic induction equation. This equation is previously known from literature [4, 6, 82, 5]. It includes the effects of time-varying magnetic fields and the material motion.

$$\frac{\partial \vec{B}}{\partial t} + (\vec{B} \cdot \nabla) \vec{v} = (\vec{v} \cdot \nabla) \vec{B} + \frac{1}{\lambda} \nabla^2 \vec{B} \quad (4.1)$$

The first term on the left-hand side is the transient part of the equation. For very large time scales, this term can be neglected. This ansatz is called "quasi-static approximation". For small time scales, this term needs to be considered in the calculation. The second term of the left-hand side and the first term on the right-hand side of the induction equation describe the convection of the magnetic field. It is the rate of change in the flux density caused by the motion. The second term on the right-hand side describes the magnetic diffusion. If we transform the induction equation to a nondimensional form, then a remarkable param-

eter called the magnetic Reynolds number Rm occurs in the equation.

$$\frac{\partial \vec{B}_*}{\partial t_*} + \left(\vec{B}_* \cdot \nabla_* \right) \vec{v}_* = (\vec{v}_* \cdot \nabla_*) \vec{B}_* + \frac{1}{Rm} \nabla_*^2 \vec{B}_* \quad (4.2)$$

This nondimensional parameter is defined as

$$Rm = \frac{v_0 L_c}{\lambda} = \mu \sigma \bar{v} L_c \quad (4.3)$$

and linearly depends on electrical conductivity σ , the mean velocity \bar{v} of the moving conductor, and a characteristic length scale L_c . As can be seen in Eq.4.2, for small values of Rm ($Rm \ll 1$) magnetic diffusion is dominant. The convection term can be neglected, and the equation simplifies to a diffusion equation (see Eq.4.4).

$$\frac{\partial \vec{B}_*}{\partial t_*} = \frac{1}{Rm} \nabla_*^2 \vec{B}_* \quad (4.4)$$

For large values of ($Rm \gg 1$), convection of magnetic field lines is more dominant and magnetic diffusion can be neglected, which means that magnetic fields are strongly stretched or compressed because of the motion of the conductor, as a secondary magnetic field is induced in the conductor and interacts with the externally applied one, $\vec{B} = \vec{B}_0 + \vec{b}$. Problems with very large magnetic Reynolds numbers are mostly related to geophysics and astrophysics because of the large length scales and high velocities. A very popular example is the deformation of earth's magnetic field during solar storms [83, 84] or the generation of earth's magnetic field due to the motion of the liquid core of the earth (geodynamo)[85, 86]. The complete induction equation is fully coupled. The velocity influences the magnetic field (deformation of magnetic field), and the magnetic field itself influences the velocity of the moving conductor (braking force). A fully coupled analysis of the inter-

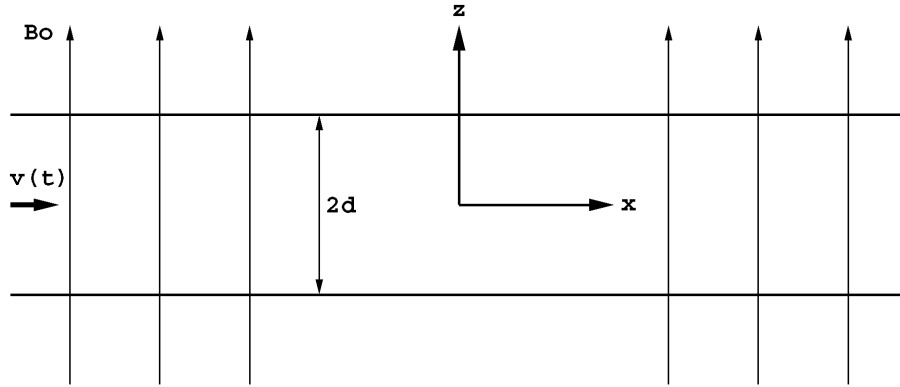


Figure 4.1.: Interaction of an infinite electrically conducting plate with a homogeneous magnetic field.

action between an electrically conducting finite plate with an externally applied magnetic field is nontrivial and requires time-consuming and expensive numerical simulations. For this reason, we provide a simple mathematical model that sufficiently represents the physics of the considered problem and takes only a few seconds for calculation. We assume an infinite plate that extends from $z = -d$ to $z = +d$. The plate is electrically conducting, and its electrical conductivity is expressed by σ . An externally applied uniform magnetic field with a magnitude B_0 penetrates the electrically conducting plate (see Figure 4.1).

At time $t = 0$, the plate remains at rest, and at time $t > 0$, the plate starts moving with a time-dependent velocity $v(t)$. From a mathematical point of view, there are two different cases, namely, the domains inside the plate and outside the plate. The difference between the domains inside and outside is given by the electrical conductivity, the velocity, and the magnetic field vector. First, the equations and boundary conditions

for the domain outside the plate are given. Here, the divergence and curl of the magnetic flux density are equal to zero.

$$\nabla \cdot \vec{B}_* = 0 \quad (4.5)$$

$$\nabla \times \vec{B}_* = 0 \quad (4.6)$$

However, this domain is not investigated further, because outside the metal sheet, no Lorentz Force and ohmic loss occur. The major object of investigation is the domain inside the plate. Here, the electrical conductivity $\sigma > 0$ and the velocity $v_* > 0$ cause a perturbation in the magnetic field (see Eq.4.8).

$$\vec{v}_* = v_*(t_*)\vec{e}_x \quad (4.7)$$

$$\vec{B}_* = \vec{e}_z + Rm b_*(z_*, t_*)\vec{e}_x. \quad (4.8)$$

Substituting Eq.4.8 and Eq.4.7 into the induction equation Eq.4.2 yields a one-dimensional diffusion equation. Finally, the one-dimensional diffusion equation is obtained as shown in Eq.4.9.

$$\frac{\partial b_*}{\partial t_*} = \frac{\partial^2 b_*}{\partial z_*^2} \quad (4.9)$$

Boundary conditions are required to solve the Eq.4.9. At time $t_* = 0$, no perturbation of the initial magnetic field occurs, because the plate is still at rest and no secondary magnetic field is induced. We formulate the initial condition as follows:

$$b_*(z_*, t_* = 0) = 0 \quad (4.10)$$

The second type of boundary conditions is related to the border between the plate and the vacuum. Subsequently, two matching conditions,

one at the upper boundary $z_* = +1$ and one at the lower boundary $z_* = -1$ are necessary. The matching condition implies that the normal component of the electrical field vector must be continuous at $z_* = \pm 1$. Moreover, fringing at the edges is neglected.

$$\left. \frac{\partial b_*}{\partial z_*} \right|_{z_*=\pm 1} = \pm v_*(t_*). \quad (4.11)$$

The third type is a symmetry condition. The entire problem is symmetric, and therefore the magnetic field induced at the center of the moving plate remains zero at all times.

$$b_*(z_* = 0, t_*) = 0 \quad (4.12)$$

In the case of a sudden jump in the velocity $v_*(t_*)$ is defined as follows:

$$v_*(t_*) = \begin{cases} 1, & \text{for } t_* > 0 \\ 0, & \text{for } t_* \leq 0 \end{cases} \quad (4.13)$$

The general solution for one-dimensional diffusion equation is previously known from literature [87, 82]. Nevertheless, it needs some modification to implement the given boundary conditions. In the mathematical model, Neumann or second-order boundary conditions are given. This specifies the values of the derivative of a solution at the boundary of the domain (see Eq.4.11). We obtain the solution of the flux density and the solution of the eddy current distribution as follow:

$$b_*(z_*, t_*) = \left[z_* - \frac{8}{\pi^2} \sum_n \frac{(-1)^n}{(2n+1)^2} \sin(n\pi z_*) \exp^{-(2n-1)^2 t_*} \right] \quad (4.14)$$

$$j_*(z_*, t_*) = \left[1 - \frac{4}{\pi} \sum_n \frac{(-1)^n}{(2n+1)} \cos(n\pi z_*) \exp^{-(2n-1)^2 t_*} \right] \quad (4.15)$$

$$(4.16)$$

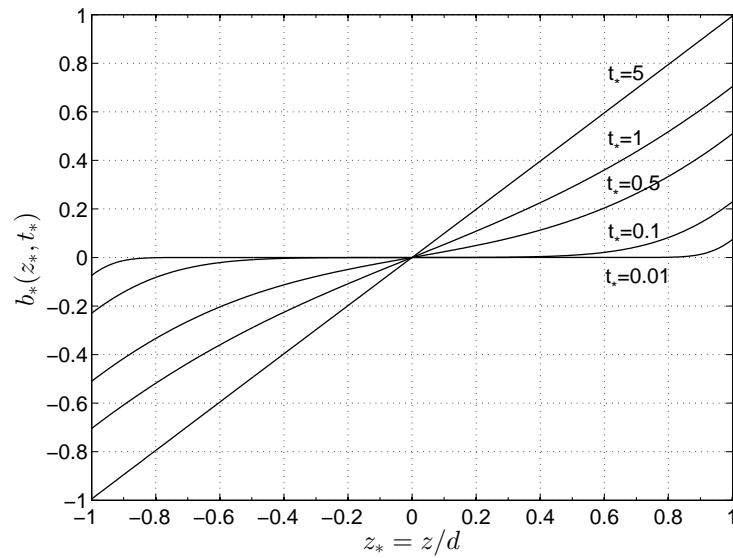
The analytical solution for several instants of time for the flux density and for the eddy currents is plotted in Figure 4.2. As can be seen easily the flux density is antisymmetric about the origin of the coordinates. The eddy currents are symmetric over the thickness of the plate. Both flux density and eddy currents are equal to zero at $t_* = 0$. When the plate starts motion, a secondary magnetic field due to the motion is induced. Here, the magnitude of the secondary magnetic field continuously increases during the transient phase and the distribution of the flux density tends to depend linearly on z after a typical reaction time T_{98} . The reaction time T_{98} indicates when 98% of the transient phase is completed. The eddy currents, which flow to oppose the flux change, must reach a constant value after the transient phase and remain constant at steady state while the plate is moving with constant velocity. The duration of the transient phase is related to the physical process of magnetic diffusion.

Once the magnetic field $b_*(z_*, t_*)$ has been determined, the nondimensional y-component of the electric current density is given by $j_*(z_*, t_*) = -\partial b_*/\partial z_*$. From these two quantities the x-component of the Lorentz force density can be derived as $f_*(z_*, t_*) = j_*(z_*, t_*)b_*(z_*, t_*)$ and the volumetric generation of Joule heat is $q_*(z_*, t_*) = j_*^2(z_*, t_*)$. By integrating these two quantities over the thickness of the plate, we obtain the nondimensional time-dependent total Lorentz force $\xi(t_*)$ and the total Joule heat $\psi(t_*)$ as

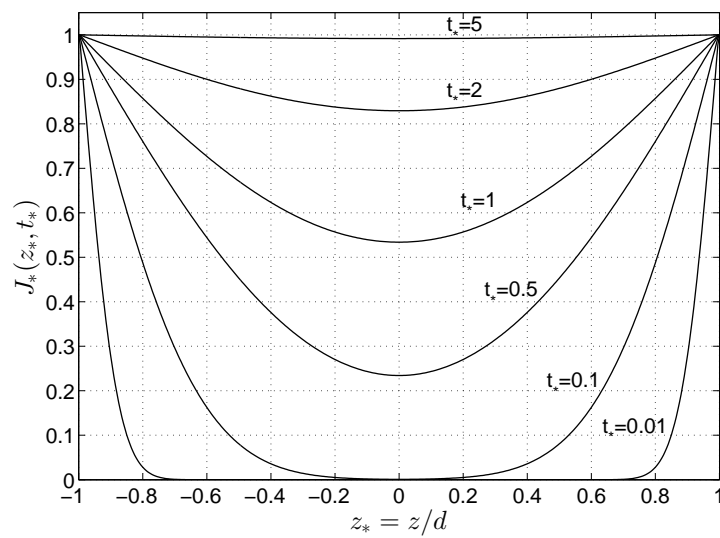
$$\xi(t) = 2b(1, t) \quad (4.17)$$

$$\psi(t) = \frac{1}{2} \int_{-1}^{+1} b^2(z, t) dz \quad (4.18)$$

The evaluation of Eq.4.17 and Eq.4.18 yields an analytical expression for the time-dependent Lorentz force $\xi(t_*)$ and power dissipation $\psi(t_*)$.



(a)



(b)

Figure 4.2.: Analytical solution of the magnetic flux density (a) and the eddy current density (b) for several instants of time.

$$\xi(t_*) = \left[1 - \frac{8}{\pi^2} \sum_{n=0}^{\infty} a(n) \exp^{-(2n-1)^2 t_*} \right] \quad (4.19)$$

$$\psi(t_*) = \int_{-1}^{+1} \left[1 - \frac{4}{\pi} \sum_n a(n) \cos(n\pi z_*) \exp^{-(2n-1)^2 t_*} \right]^2 dz_* \quad (4.20)$$

Here, $a(n)$ is defined as follows:

$$a(n) = \frac{(-1)^n}{(2n+1)} \quad (4.21)$$

Figure 4.3 shows the analytical solution for the time-dependent Lorentz force $\xi(t_*)$ and power dissipation $\psi(t_*)$. Both are equal to zero while the plate remains at rest. After a sudden jump in the velocity of the conductor, the Lorentz force and the Joule heat increase, and reach a steady value after a characteristic reaction time. From Eq.4.19 and Eq.4.20, we derive that the space harmonics damp at different rates. The harmonics damp faster for higher value of n . This fact is reasonable because it is sufficient to calculate only three terms in the series. Moreover, for $t > \tau$, it is sufficient to calculate only the first term of the series. Hence, the fundamental time constant τ , which is the longest time constant of the series, is the controlling time constant in process. It is defined as follows:

$$\tau = \frac{4d^2}{\lambda\pi^2} \quad (4.22)$$

The functions $\xi(t_*)$ and $\psi(t_*)$ allow us to determine the reaction times $T_{98\xi}^*$ and $T_{98\psi}^*$ which are defined via $\xi(T_{98\xi}^*) = 0.98$ and $\psi(T_{98\psi}^*) = 0.98$, i.e. as the time where the Lorentz force and the Joule heat have reached 98% of their asymptotic values. Our solution yields the nondimensional reaction times $T_{98\xi} = 3.689$ and $T_{98\psi} = 4.369$ which for practical purposes can be translated into dimensional reaction times as $T_{98\xi} =$

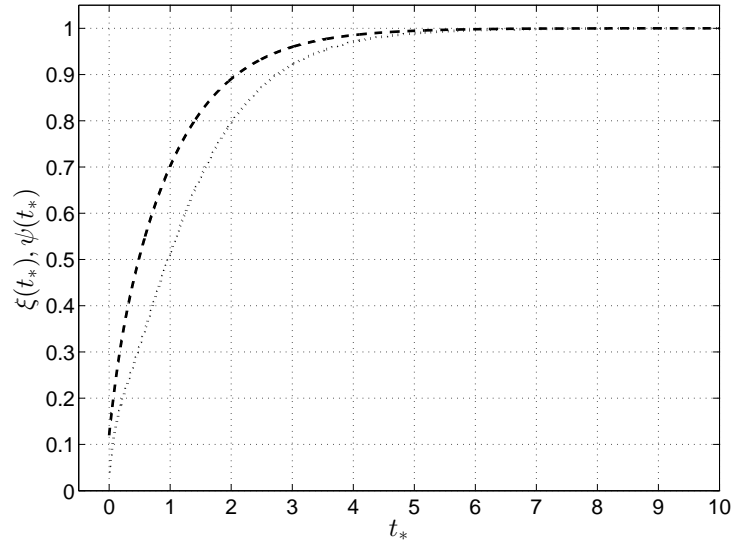


Figure 4.3.: Analytical solution for the time-dependent Lorentz force and Joule heat in the case of a sudden jump in the velocity of the plate. The dashed line indicates the Lorentz force, and the dotted line represents the Joule heat.

$3.689d^2/\lambda$ and $T_{98\psi} = 4.369d^2/\lambda$. The step response of a device is significant in dynamic processes. With the results of the study, it is possible to estimate the feasibility of LFV in dynamic flow measurement.

4.2. Numerical solution using finite difference method

In order to investigate the time-dependent Lorentz force and power loss for more sophisticated and realistic motion setups, a finite difference code has been applied to the one-dimensional partial differential diffusion equation. This code needs no further verification, because it is standard

in the treatment of such equations [88]. However, an explicit method is used. A first-order forward difference at time t_k and a second-order center difference for the space derivation z_i results in the recurrence equation as follows:

$$\frac{b_i^{k+1} - b_i^k}{\Delta t} = \lambda \frac{b_{i+1}^k - 2b_i^k + b_{i-1}^k}{\Delta z^2} \quad (4.23)$$

$$b_i^{k+1} = (1 - 2\theta)b_i^k + b_{i-1}^k + \theta b_{i+1}^k \quad (4.24)$$

$$\theta = \lambda \frac{\Delta t}{\Delta z^2} \quad (4.25)$$

Next, b_i^{k+1} can be obtained from the last time step, but this implies that boundary conditions at time $b_i^{k=0}$ and at positions $b_{i=0}^k$ and $b_{i=n}^k$ have to be known. Here, the boundary conditions are previously known and given as follow:

$$\left. \frac{\partial b_*}{\partial z_*} \right|_{z_*=\pm 1} \Rightarrow \frac{b_i^k - b_{i-1}^k}{\Delta z_*} = -1 \quad (4.26)$$

The explicit method has been selected because it is less numerically intensive in comparison with other finite difference methods such as the Implicit method or the Crank-Nicolson method. In addition, it is numerically stable and convergent whenever $\theta \leq 1/2$ [87].

Figure 4.4 shows the results of the numerical simulation for several motion setups of the plate. The solid line represents the velocity of the plate; the dashed line the Lorentz force and the dotted line the power loss. Four different motion setups have been considered, namely, step function, ramp, sinusoidal motion, and motion with finite acceleration. Here, the step function is used to check the validity of the numerical code. It can be seen in Figure 4.4 that Lorentz force and power loss show strong time-dependence in all cases of motion. However, the power dissipation reacts

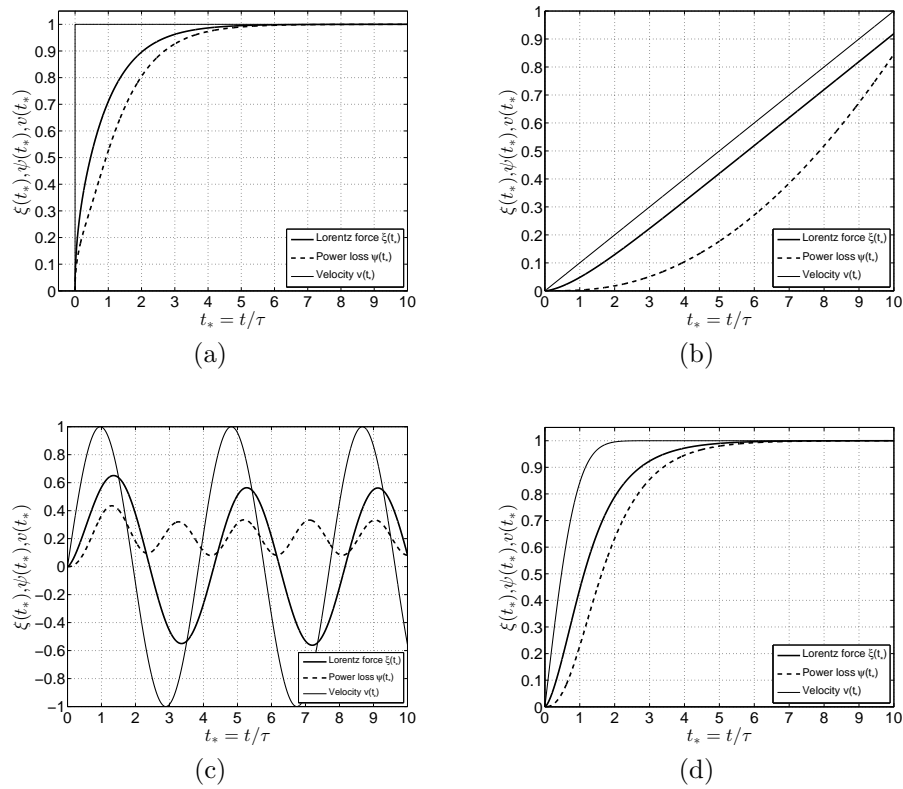


Figure 4.4.: Transient response for several motion setups: (a) Step function. (b) Ramp. (c) Sinusoidal excitation. (d) Finite acceleration of the plate with $\beta = 1$.

slower, $T_{98\psi}^* = 4.341$ than the Lorentz force $T_{98\xi}^* = 3.659$. In the case of a sudden jump in the velocity of the conductor, the time response is identical to the analytical solution. This demonstrates the validity of the numerical code. In Figure 4.4b the metal sheet is constantly accelerated and its velocity linearly increases with time. It can be seen that both Lorentz force and power dissipation have a smaller slope at the beginning. After a typical reaction time, the Lorentz force has the same slope as the velocity. In contrast, the Joule heat does not reach a constant slope because it depends on the square of the velocity. This fact is remarkable in the case of sinusoidal motion of the plate. Here the Joule heat doubles the frequency of the plate motion. Moreover, there is a phase shift in the case of sinusoidal motion. For $f \rightarrow 0$, the phase shift tends to be zero $\Delta\phi = 0$. For $\omega \rightarrow \infty$, the phase shift converges to $\Delta = -\pi/4$. The amplitude of the Lorentz force and power dissipation depend on the frequency. For $f = 0$, the amplitude is equal to the value in the case of a step function. For $\omega \rightarrow \infty$, the amplitude goes to zero. The case of sinusoidal motion is physically identical to the case of an alternating magnetic field. The higher the frequency, the smaller is the penetration depth of the magnetic field into the plate. Subsequently, the currents tend to crowd into the region near the surface. This region is called the skin layer, which has a skin depth $\delta = \sqrt{\frac{2\omega}{\lambda}}$. The literature provides an analytical solution for the sinusoidal motion [82].

Excitation in the form of an error function represents a realistic case of a finite accelerated motion for instance a linear drive with motion controller. The error-function is expressed as follows:

$$v(t_*) = \operatorname{erf} \left[\frac{t_*}{\beta} \right] \quad (4.27)$$

If β equals zero, then the error function shows identical characteristic as the step function. For large values of β the error-function has a

| β | T_{98v}^* | $T_{98\psi}^*$ | $T_{98\xi}^*$ |
|---------|-------------|----------------|---------------|
| 0 | 0 | 4.29 | 3.62 |
| 1 | 1.65 | 4.96 | 4.29 |
| 2 | 3.29 | 5.91 | 5.24 |
| 3 | 4.93 | 7.20 | 6.49 |
| 4 | 6.58 | 8.74 | 7.92 |

Table 4.1.: Comparison of the nondimensional response time of the input velocity T_{98v}^* , the Lorentz force $T_{98\xi}^*$, and the Joule heat $T_{98\psi}^*$ for different instants of β .

smaller slope (see. Figure 4.4d). The consequence of this motion setup causes larger reaction times (see table 4.1).

Finally, we give an example for a real sequence. The calculations are performed for an aluminum slab with a thickness of $d = 0.08m$ and an electrical conductivity of $\sigma = 36 \cdot 10^6 S/m$. The initial magnetic field has a induction of $B_0 = 0.3T$ and the slab moves with a velocity of $v = 2m/s$. It emphasizes that the reaction of the Lorentz force equals $T_{98} = 100ms$ for the considered properties (see Figure 4.5).

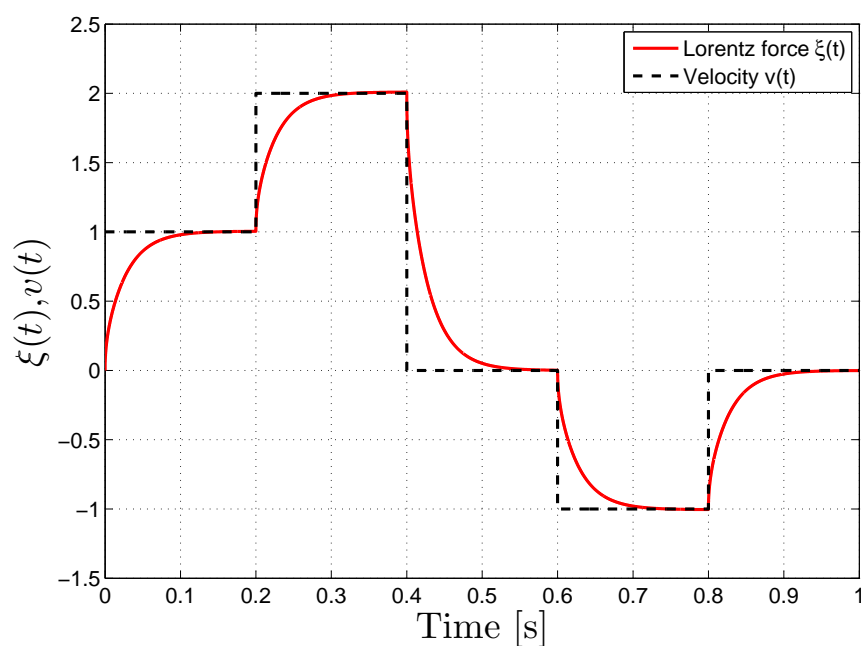


Figure 4.5.: Time-response of the Lorentz force $\xi(t)$ for an arbitrary velocity function $v(t)$. The calculations are performed for an aluminum sheet with a thickness of $d = 0.08m$ and an electrical conductivity of $\sigma = 36 \cdot 10^6 S/m$. The initial magnetic field has a magnitude of $B_0 = 0.3T$, and the metal sheet moves with a maximal velocity of $v = 2m/s$.

5. Laboratory experiments

This thesis is focused on the design and laboratory test of an LFF for pipe flows. Generally two different experimental setups have been built during the study period (see Figure 5.1). First, an experiment for the determination of the response time T_{98} was conducted. The aim of the first experiment is to get an overview of the order of magnitude and verify the results of the analysis in section 4. The second experiment was conducted to determine the calibration constant k . It operates automatically and is suitable for the calibration and sensitivity analysis of all kinds of LFFs in vertical applications.

5.1. Experimental investigation of the response time

5.1.1. Experimental setup

The investigation of the response time requires rapid changes in the mass flux at a given point in time. If all geometry conditions are kept constant, a sudden jump in the mass flux can be induced by a strong acceleration of the solid body. The solid body is made of an aluminum alloy (AlMgSi) with an electrical conductivity of $\sigma_{Al} = 21.34 \cdot 10^6 S/m$. It measures 65mm in diameter and 1000mm in length. The aluminum rod is fixed, but at time $t = 0s$, it is disconnected and accelerated by gravity $g = 9.81m/s^2$ from an altitude of $h = 450mm$. After a free fall time of $t \approx$

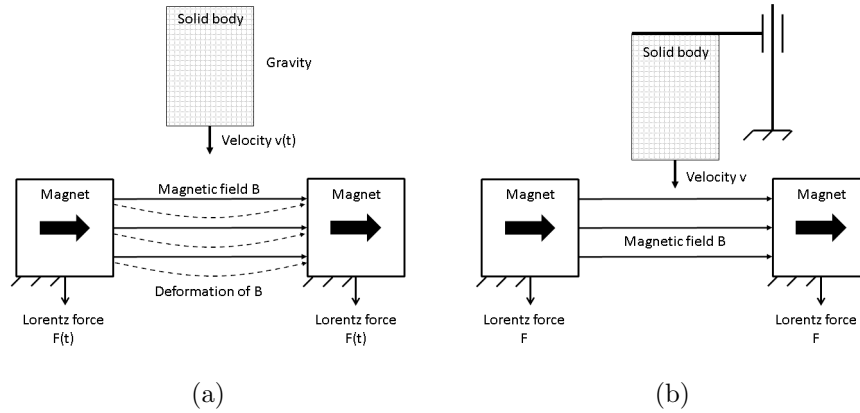


Figure 5.1.: Illustration of the two laboratory experiments. (a) Experiment for the determination of the response time of the LFF. A solid body is accelerated by gravity and passes the magnetic field. (b) Experiment for the determination of the calibration constant and sensitivity analysis. Here, a solid conductor moves with controlled motion.

350ms, the solid body reaches a final velocity $v = 2.95\text{m/s}$. After the free fall it hits the ground and stops motion immediately. This process has a high repeatability because gravitation is constant. Influence by friction can be neglected because linear bearings are used to guide the aluminum rod. When the solid body starts motion, it is already seeded with a magnetic field produced by two blocks of NdFeB. As discussed in section 4, the reaction time does not depend on the magnitude and the distribution of the applied magnetic field. Each block has a length of 100mm, a width of 60mm, and a height of 30mm. The magnets are arranged face to face at a distance of $s = 70\text{mm}$ and the direction of magnetization is perpendicular to the moving direction of the reference body.

The experimental setup has a modular construction (see Figure 5.2). Aluminum profiles (Henkel & Roth GmbH) are used for framework de-

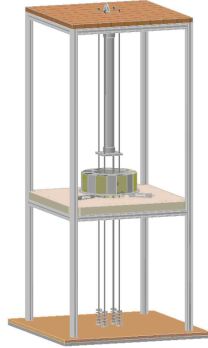


Figure 5.2.: Illustration of the experimental setup for investigation of the time-dependent Lorentz force.

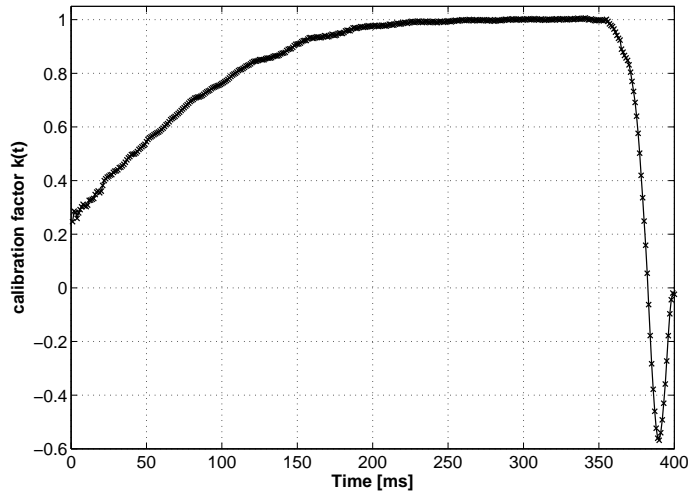
sign. A wooden panel at the top and bottom and a heavy aluminum plate in the middle realize high stiffness. The effect of torsion, transverse forces, and bending is moderate. To avoid damage when the rod hits the ground, a KMS damper system is used to absorb the energy of the impact. The force measurement system consists of three single point load cells (Lorenz-Messtechnik GmbH Type AL10) and three data processing units (Lorenz-Messtechnik GmbH Type USB-LCV). An analog/digital converter integrated in the unit has a sampling frequency of $f_s = 1000\text{Hz}$. A PC records all data in a CSV-file. Further data processing is done with Mathworks MATLAB. The measurement comprises 100 repetitions.

5.1.2. Results and discussion

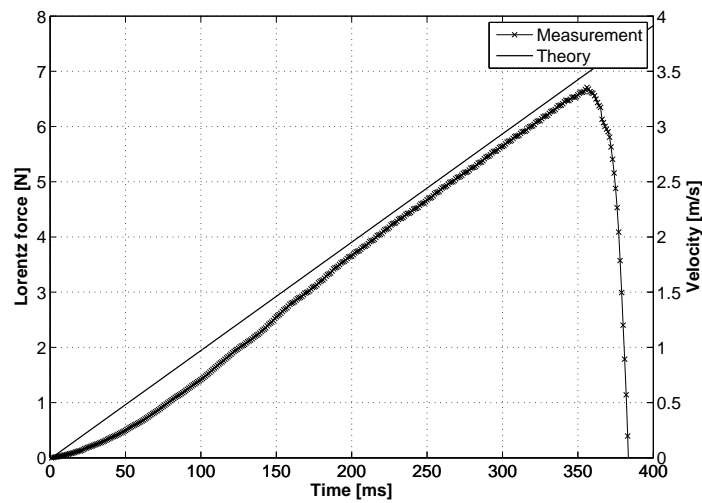
In summary, the experiment has high repeatability. The mean of all single measurements is calculated and referred to as a theoretical moving velocity, which can be easily calculated by $v(t) = g \cdot t$. Dividing the measured Lorentz force $F_L(t)$ by the theoretical velocity $v(t)$ of the aluminum rod gives a calibration factor $k(t_i)$ for each time step t_i . During the tran-

sient phase, the calibration factor varies in time and approaches to a constant value (see Figure 5.3a). If $k(t)$ remains constant, the transient phase is completed and the measured Lorentz force $F_L(t)$ follows the velocity $v(t)$. Figure 5.3b compares the input signal (velocity) and the output signal (Lorentz force). It can be seen, that there is a pronounced transient phase in the range of $0ms \leq t \leq 170ms$. After approximately 220ms the transient phase is almost complete and the Lorentz force follows the input signal with a constant slope. In the experiment, the transient phase takes twice as long as in the numerical calculation of the Lorentz force; but this arises from the combination of the single point load cells with the magnet system. In consequence, the response time of the LFF is the sum of the response times of the electromagnetic system (Lorentz force) T_{mag} and mechanical system (load cell) T_{mech} . The LFF can be described as a PT3-Element with a response time of $T_{98} = 220ms$ for the case of a moving aluminum rod with an electrical conductivity $\sigma = 20.53 \pm 0.06MS/m$ and a diameter of $d = 65.11 \pm 0.03mm$.

According to section 4, the duration of the transient phase of the Lorentz force depends on electrical conductivity and the diameter of the conductor. Note that liquid steel has an electrical conductivity of the order of $\sigma \approx 10^5 S/m$, which is considerably smaller than that of the solid aluminum rod. Then, the mechanical system results in the governing time constant. A good agreement can be observed on comparing these results with those obtained using a MATLAB Simulink model (see Figure 5.4). In the model we consider all determined material parameters for the load cells and the aluminum rod.

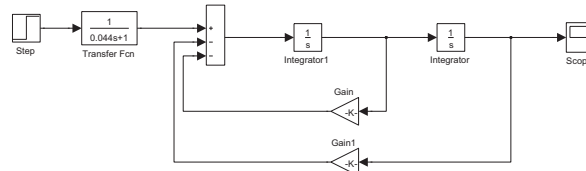


(a)

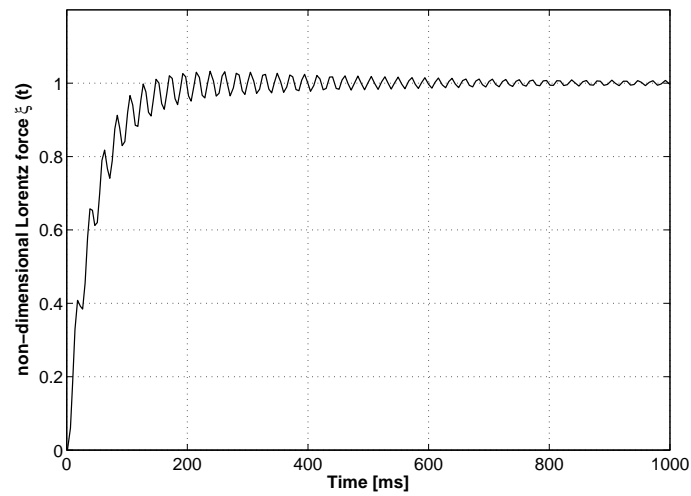


(b)

Figure 5.3.: Results of the experimental investigation of the time response of a Lorentz force flowmeter. The results were obtained using an aluminum rod with a diameter of 65mm and an electrical conductivity of $20.53 \cdot 10^6$ S/m. (a) Comparison between the theoretical velocity of the free fall of the body and the measured Lorentz force (b) Time-dependent calibration factor $k(t)$.



(a)



(b)

Figure 5.4.: Results obtained by MATLAB Simulink using the determined material properties of the load cells and the solid body. (a) Simulink block structure. (b) Time response of the LFF after a jump in the moving velocity.

5.2. Experimental investigation of calibration constant

Every measurement device needs to be calibrated to produce reliable data. The calibration of electromagnetic flowmeters has been investigated previously [89, 90], particularly for channel flows. In open channel flows, for instance, in aluminum launders, a calibration function $k(x_i)$ is required to calibrate the device. Here, the calibration function depends on different parameters x_i such as electrical conductivity, channel geometry, and the level of liquid metal in the channel [56, 91, 92]. Liquid metals often are hot, aggressive, and opaque[17]. Material properties which cause high costs when setting up a laboratory experiment for wet calibration of LFFs. Such a facility is currently under construction, but it is not ready for operation yet. There is a possibility for dry calibration of the LFF. This method was studied by V. Minchenya in 2011 [56] for open channel flows, and it is applicable to LFFs for pipe flows, too. Wang et al. studied the possibility of numerical calibration of a LFF for liquid metals with reasonable results [93].

5.2.1. Experimental setup

The setup of the dry calibration experiment of an LFF for pipe flows is strongly related to the experimental setup presented by M. Gramss [94]. A linear drive is used to move a circular solid body with a velocity $v(t)$ through the magnetic field of an LFF (see Figure 5.1b). A three-phase synchronous motor with speed a controller drives the spindle of a linear guide unit with a constant speed n . The maximal acceleration is $a_{max} = 20m/s^2$ and the maximal velocity is $v_{max} = 50mm/s$ because of the removable spindle of the trapezoidal screw thread. v_{max} could be increased using another spindle with a larger thread pitch. The high ac-

celeration of the linear drive theoretically provides a good opportunity to realize a step function for the velocity of the solid body. However, in practice, the velocity must be increased by ramp. Otherwise, the mechanical stress on the spindle would be cause vibrations during start process and subsequently lead to rapid fatigue of the material. Nevertheless, the slope of the ramp can be set as strong as possible. The linear drive is mounted on a rack made of aluminum profiles (Henkel and Roth HR50). The rack stands on four vibration absorbing pillars. The measurement table is located in front of the linear drive. The table stands on four vibration-absorbing pillars and is mounted with aluminum profiles (Henkel and Roth HR50). A heavy aluminum plate with a thickness of $\delta = 10mm$ and a cross section of $850mm \times 850mm$ is mounted on the top of the table. In the center is a circular recess clearance through which the solid body can pass the LFF. The aluminum plate is bored in order to mount load cells or the entire LFF on top of the plate. For the fundamental research on the dry calibration experiment, we use a special Halbach array (see Figure 5.5 and Figure B.5), which has been assembled in order to learn how to deal with. A resistive path sensor is installed to measure the traveled distance. The first derivative with respect to time provides the velocity of the reference body. To avoid damage in the event of a fault, we use inductive position switches on the upper and lower ends of the linear drive and two additional light barriers prevent collision.

The electric control cabinet for the linear drive was obtained from the company SCHEBA GmbH. However, for automation purposes, a new electric control cabinet was assembled (see Figure 5.6). Here, a special communication and automation system based on OPC-Server connection realizes communication among the dry calibration experiment, the control center of the steel plant, and the PC in the office. The experimental setup is fully automated. An IBA-Automation environment that

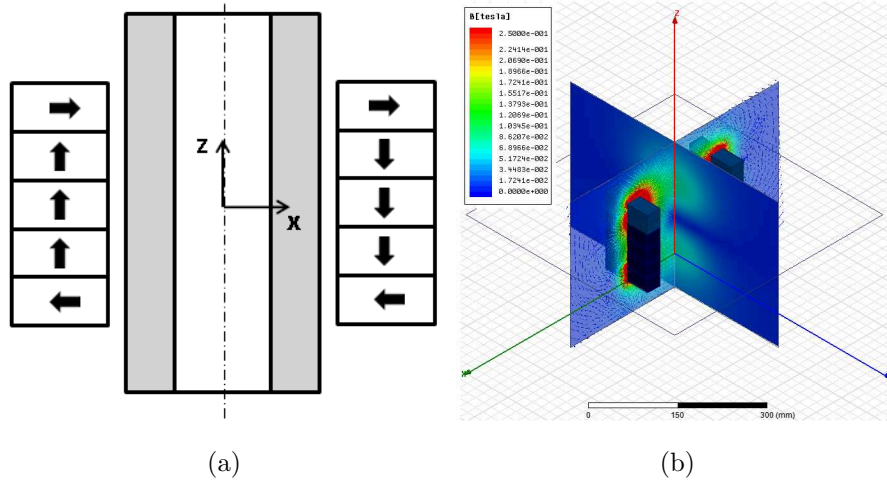


Figure 5.5.: Magnet system used in the dry calibration experiment: (a) Illustration of the magnet system and the magnetization pattern. (b) Isometric view of the FE model.

consists of an IBA-PDA, IBA-Padu-8U, and IBA Padu-8O realizes the required input and output signal for controlling the linear drive and data acquisition. A home-made electronic device, developed and built under my supervision by a Masters student Daniel Martschoke amplifies, smoothens and denoises the measurement signal [95]. There are different motion setups available, namely, step, ramp, sinusoidal motion with a frequency f , and a free programmable velocity characteristic to simulate real production processes.

The test is executed as follows: The solid body is moved to the initial position. Here the solid body is already seeded with the magnetic field. At $t = 0s$, the linear drive starts motion and moves downwards with constant velocity. After $\Delta t = 10s$, it stops motion and remains at rest for $\Delta t = 5s$. Finally, the linear drive reverses its moving direction and moves back to its initial position. The measurement comprises different

velocities in a range of $5\text{mm/s} \leq v \leq 50\text{mm/s}$ with a step size of $\Delta v = 5\text{mm/s}$. Moreover several diameters of the solid body and two different materials (aluminum and copper) have been used. Each measurement is done with at least 20 repetitions in order to analyze the uncertainty of the measurement. Data recording for this analysis starts automatically when the motor starts motion and is completed when the motor stops. Data processing is done using MATHWORKS MATLAB. The electrical conductivity of the solid body has been measured via Förster Sigmatest 2.069 (see Tables A.2 and A.1) and the diameter has been measured using a scale (see Tables A.3 and A.4).

5.2.2. Results and discussion

The dry calibration experiment turned out to be much more than an automatic calibration facility. It offers the opportunity to gain many insights into the complex processes behind LFV. The experimental results give clear information about the calibration factor. Moreover, it provides information about the relation between Lorentz force and the diameter of the SEN as well as information about the sensitivity against the off-center position. Figure 5.7 shows the results of the dry calibration experiment for several copper and aluminum rods. It can be seen that there is a linear correlation between Lorentz force and velocity in all considered variations. The Lorentz force obtained with a copper rod of the same size as the aluminum rod is higher than that of the aluminum rod by a factor of σ_{Cu}/σ_{Al} . These results agree with experiments of Gramss et al. [94], Alferenok et al. [96], and with the theory proposed by Thess et al. [17]. The comparison of experiment and simulation match closely with a maximal deviation of less than 3% for copper and less than 1% for aluminum. Of particular note is the fact that values obtained experimentally are higher than those obtained numerically. One

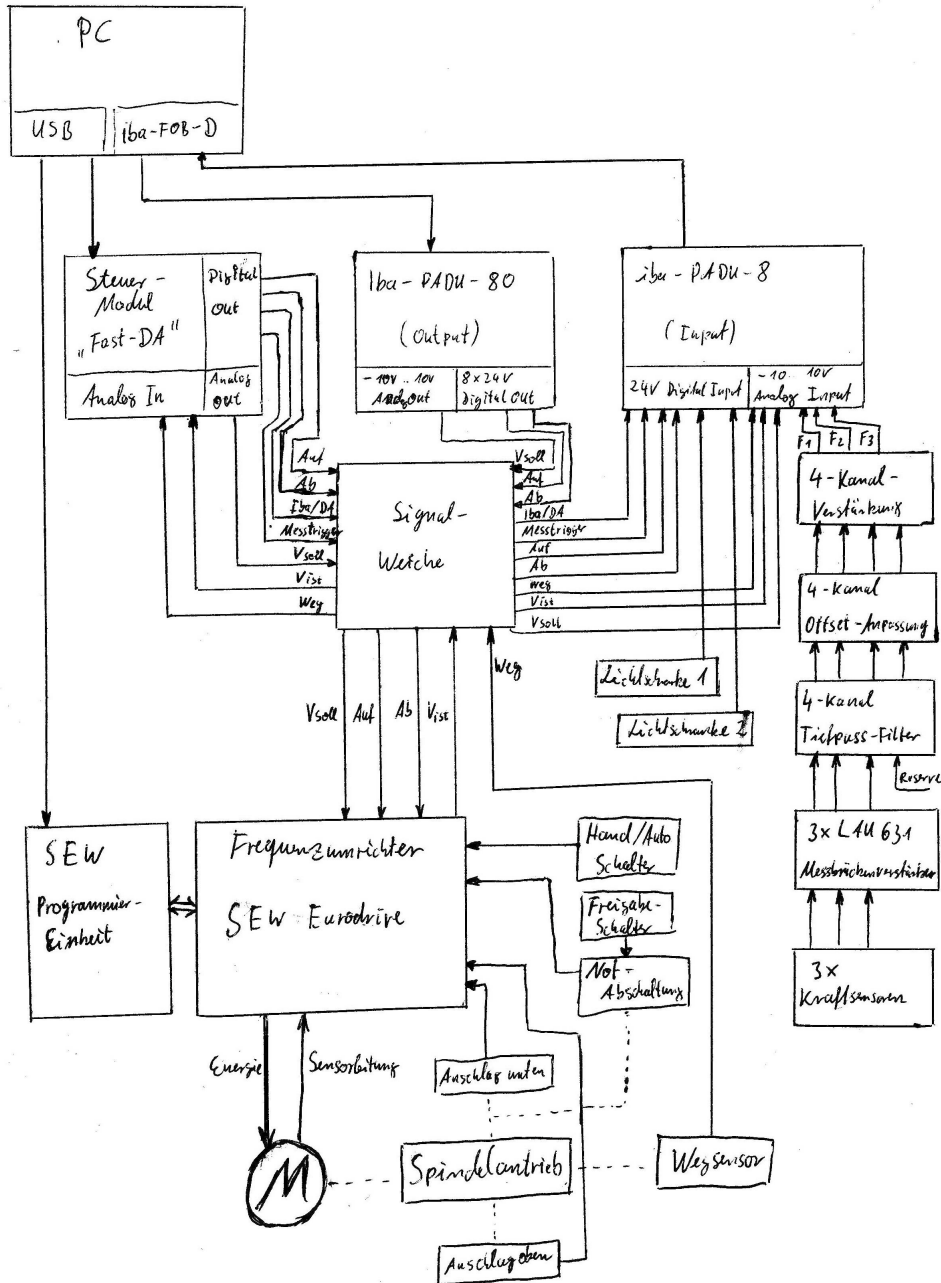
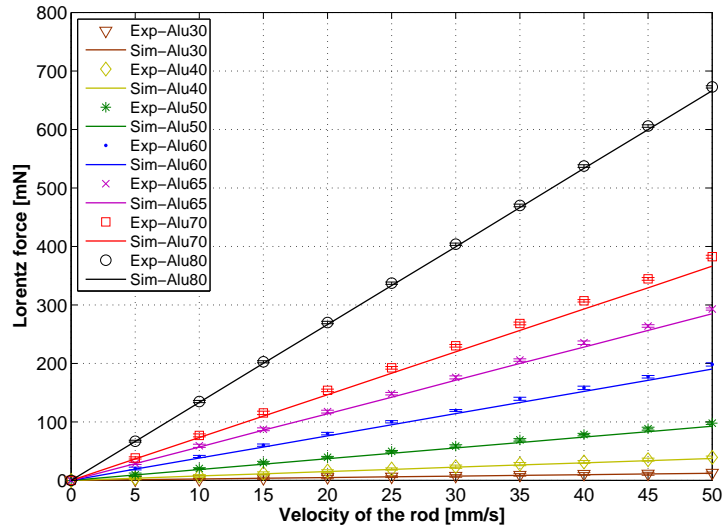


Figure 5.6.: Working flow of the OPC-Server structure for the calibration experiment. By courtesy of Daniel Martschoke [95].

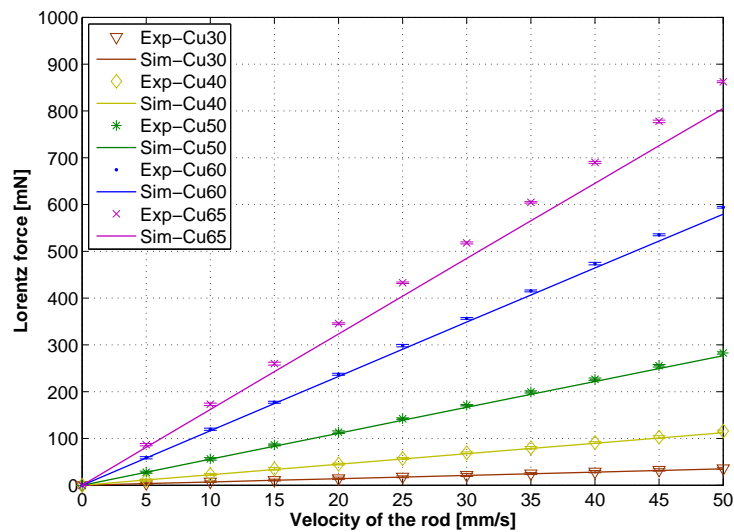
reason for this could be that the diameter of the rods deviates from the nominal value (see Tables A.4 and A.3). Another reason could be the position of the rod. After each test run, the rod is realigned using a scale. The positional accuracy is merely $\pm 1\text{mm}$. Moreover, there is an uncertainty in the measurement of the electrical conductivity of the solid body. The electrical conductivity has been carefully measured. Copper tends to form an oxide layer in an oxidizing environment and this layer influences the measurement (see Table A.2 and A.1). Finally, the magnets themselves could also cause deviation. The material properties residual inductance B_R and coercive field strength H_c , always vary within a batch. The distributors specify all material properties within a range (see Table A.5) and therefore all simulations use the mean value of the specified range. Table 5.1 lists the calibration constant k determined for different sizes of the copper and aluminum rod. The value of k is calculated using linear regression from the measurement data. The uncertainty of measurement is determined according to the "Guide to the Expression of Uncertainty in Measurement" published in 1993 [97]. We assume that $F = k \cdot v$ and $k = k(d, \sigma, B)$. Figure 5.8 compares the prescribed mass flux with the measured flux. A remarkable agreement can be observed.

Table 5.1.: Calibration factor k for aluminum and copper rods

| diameter [mm] | k_{Cu} [Ns/m] | k_{Al} [Ns/m] |
|---------------|---------------------|---------------------|
| 30 | 0.256 ± 0.0040 | 0.704 ± 0.0080 |
| 40 | 0.790 ± 0.0118 | 2.299 ± 0.0069 |
| 50 | 1.943 ± 0.0116 | 5.665 ± 0.0192 |
| 60 | $3,973 \pm 0.0188$ | 11.862 ± 0.0286 |
| 65 | $5,819 \pm 0.0169$ | 17.345 ± 0.0477 |
| 70 | $8,094 \pm 0.0710$ | |
| 80 | $13,596 \pm 0.0348$ | |

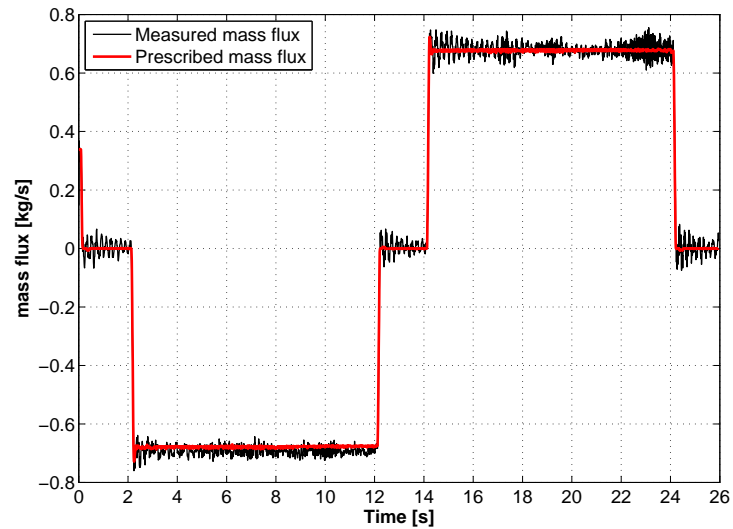


(a)

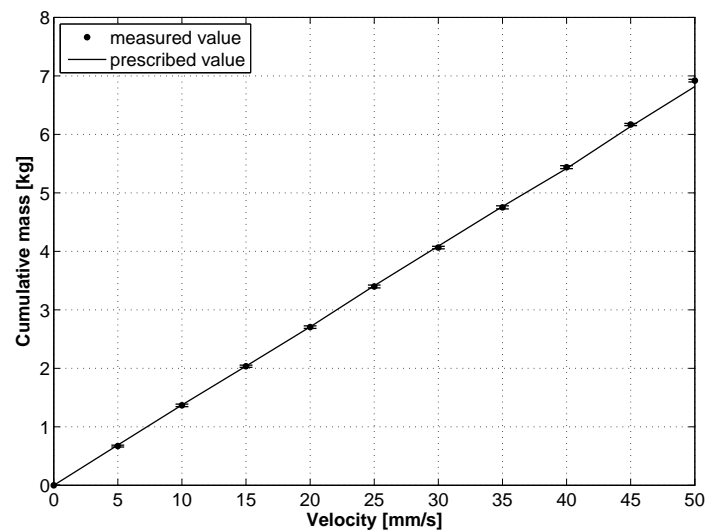


(b)

Figure 5.7.: Results of the dry calibration experiment for aluminum and copper rods of different diameters: (a) Calibration curves for the aluminum rods. (b) Calibration curves for the copper rods.



(a)

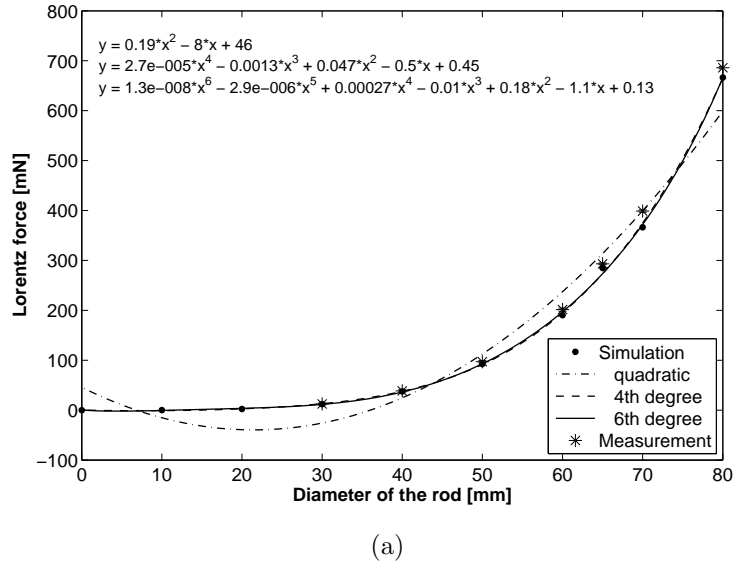


(b)

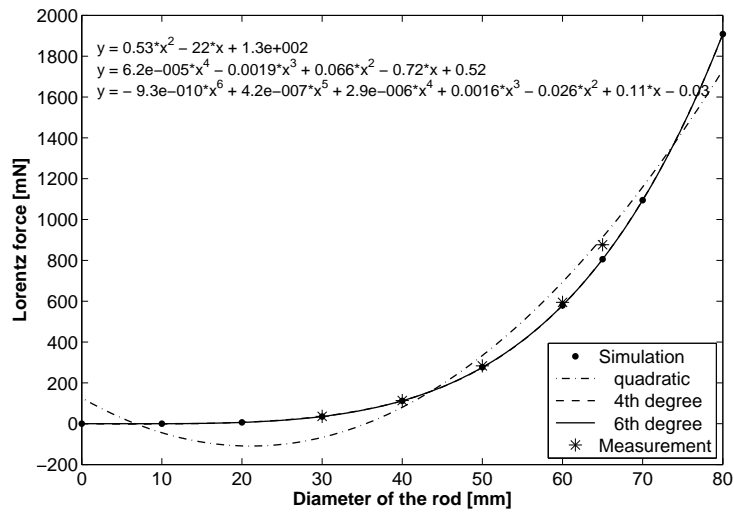
Figure 5.8.: Measured mass flux and cumulative mass compared with the prescribed value. (a) Mass flux of the 80mm aluminum rod moving with a velocity of 50mm/s. (b) Cumulative mass for several instants of velocity for the 80mm aluminum rod.

Figure 5.9 gives an overview about the relation between the Lorentz force and the diameter of the pipe. In Figure 5.9a and Figure 5.9b show the measured and simulated Lorentz force for several instants of d for aluminum and for copper respectively. Unfortunately, copper rods with $d = 70mm$ and $d = 80mm$ are not available at this time. However, five samples for copper might be sufficient to predict any reliable forecast. A highly nonlinear dependence could be observed for both materials. This is remarkable for the future device because a partially filled pipe seems to influence the measurement significantly. For example, in continuous casting liquid steel tends to form a kind of jet inside the SEN, and thus, the effect might be useful. If we assume a completely filled pipe, then it could be possible to measure the effect of clogging of the pipe. This offers a new LFV application that has great importance. Figure 5.9a and Figure 5.9b show different polynomial fits to approximate the relation. In contrast to the measurement, each curve starts with $d = 0mm$ and contains more samples. The measured values agree very well with the simulation, and we conclude the accuracy of the simulation for other diameters. As can be seen, at least a fourth degree polynomial fit is required for accurate approximation. One reason for the highly nonlinear relation between Lorentz force and the diameter of the pipe could be the distribution of the magnetic field. Note that the Lorentz force depends on the square of the magnetic induction, and again, the magnetic induction depends on the third power of the distance.

Figure 5.10 shows the results of the sensitivity analysis. The first plot shown in Figure 5.10a displays the prediction of the numerical simulation, and the second plot illustrates the measurement data. It can be seen that measurement and simulation agree very well. The differences between the simulation and the measurement could be based on a positional accuracy of $\pm 1mm$ after realignment. This magnet system is a special Halbach array and the response surface shows typical charac-



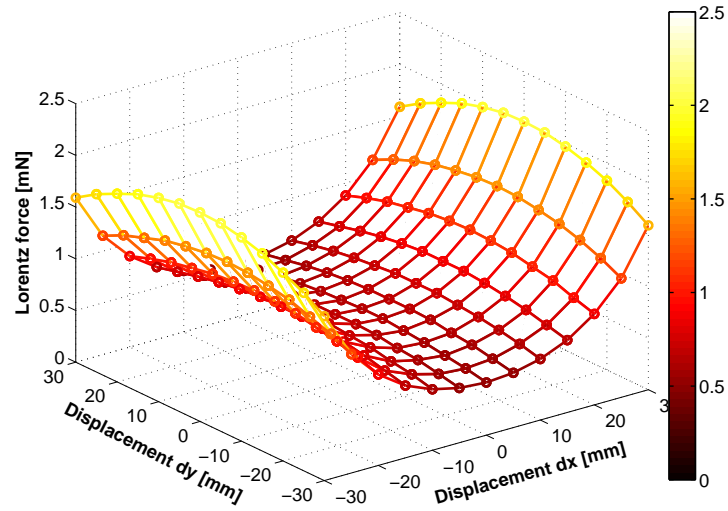
(a)



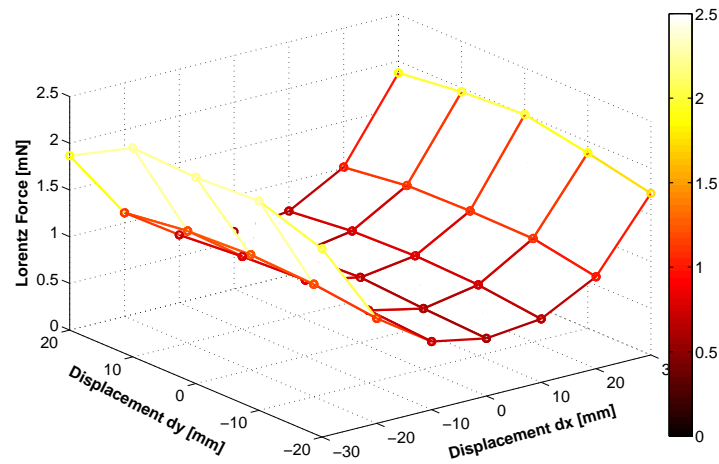
(b)

Figure 5.9.: Correlation between Lorentz force and diameter of the rod for a moving velocity of 50mm/s. (a) Experimental results compared with the numerical results and polynomial fitting for aluminum. (b) Experimental results compared with the numerical results and polynomial fitting for copper.

teristics for that kind of a magnet system. A displacement dx in the direction of the pol faces increases the Lorentz force significantly. At $dx = \pm 30mm$ the Lorentz force is more than three times higher than it is at $dx = 0mm$. In contrast, a displacement along the y-direction dy slightly decreases the Lorentz force. At $dy = \pm 20mm$, it reduces by a factor of 12%. These results corroborate the theoretical analysis described in section 3.1.3, and it seems that any kind of Halbach array is very sensitive against an off-axis position. Moreover, we can corroborate the hypothesis that this kind of magnet system needs large distances between the pol faces to exhibit its full potential and effectiveness. Therefore, a Halbach array seems to be suboptimal for LFV in continuous casting of steel and pipe application with large length scales.



(a)



(b)

Figure 5.10.: Sensitivity analysis for off-center position of the moving aluminum rod ($d=80\text{mm}$). The moving velocity is 50mm/s . (a) Results obtained by numerical simulation. (b) Results obtained in the experiment.

6. Plant test

The construction process of the device is not content of the PhD thesis, because it includes confidential documents such as technical drawings and remarkable know-how. A contract with industrial partners prohibits the publication of sensitive information. The plant tests are an additional performance done during the study period to verify the ideas of the conceptual study described in the previous chapters. Figure 6.1 shows a photograph of the first prototype of an LFF for pipe flows dedicated for application in continuous casting of steel. The plant test has been performed in close cooperation with our industrial partners.

A fully equipped LFF contains sensible and expensive components. Thus, it is advisable to test the housing and the cooling system first to avoid damage caused by overheating during the measurements. This section describes the two industrial tests. The first is the test of the cooling system and the second, the test of flow measurement.

6.1. Test of cooling and housing

6.1.1. Preparation for the test

The first prototype of an LFF for pipe flows with application in continuous casting of steel is of a circular shape and measures 460mm in diameter and 250mm in height (see Figure 6.1). The housing consists of five parts. Two identical aluminum plates with a thickness of $\delta = 40mm$ are used at the top and bottom of the device. In between, there are two

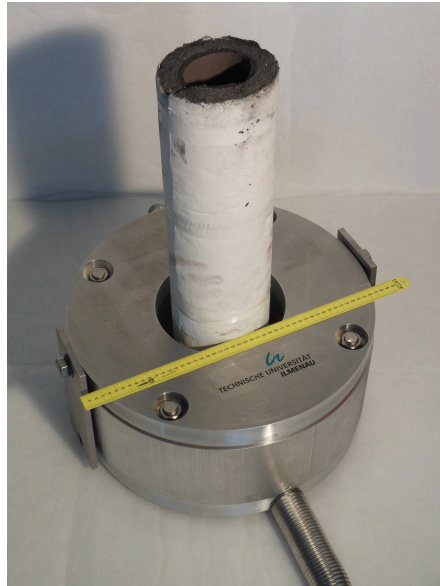


Figure 6.1.: Photograph of the first prototype of a Lorentz force flowmeter for pipe flows.

hollow cylinders: a large outer cylinder with a diameter of $D = 460\text{mm}$ and a smaller inner cylinder with a diameter of $D = 220\text{mm}$. Both have a wall thickness $\delta_{\text{wall}} = 10\text{mm}$. The inner cylinder fulfills two functions at the same time. First, it provides stability for the housing, and second it is main component of the cooling system. The cooling system is identical to proposal 2 in section 3.2.3. Because the inner tube is close to the SEN, the operators believe that aluminum is an unsuitable candidate for constructing the device. Should the cooling system be damaged, the cooling air could freeze the SEN (clogging). Consequently, the caster sequence could be interrupted, which is very expensive for the operator. For that reason, this component is made of stainless steel (1.4301) with a melting temperature of $T = 1550^\circ\text{C}$ to avoid phase transition in the event of direct contact between the SEN and the device. Both aluminum plates are bolted together using threaded stainless steel rods (M20), and

they encapsulate the outer and inner cylinders. At the junction between the inner ring and the top plate as well as at the junction between the inner ring and the bottom plate, a heat resistant seal is used to realize airtightness. Finally, two rectangular plates made of weldable steel are used on the left and right sides of the device to connect it to the tundish. The plates have a length of 260mm and protrude approximately 10mm over the top surface of the cover plate to be as close as possible. The connection of the cooling system to the air supply requires a long high-pressure hose owing to the long distances. A removable connection is chosen in order to disconnect the device in the event of an emergency. Here, a high-pressure hose and fittings from Argus Fluidtechnik GmbH with a heat protection system delivered by ANAMET Europe AG are used. The first 12m of the heat resistant data cable (Leoni AG) and high-pressure hose from the device to the link are fully covered with the heat protection material. In addition, a flexible stainless steel tube is used to cover the first 3m to protect against drops of liquid steel. After 12m there is a link where the data cable and the pressure supply can be disconnected during the casting sequence. Then, a second 12m section of data cable connects the device with the electrical cabinet. Within the first twelve meter section the data cable is directly fixed on the high-pressure hose to minimize influences from heating up the cable. The electrical control cabinet has a power supply with a voltage transformer (AC $230\text{V}/\text{DC } 24\text{V}$). All transducers operate with a supply voltage of $U_s = 24\text{V}$. The box contains three universal transducers (KNICK VarioTransP1) and three temperature transducers (LKM Electronics). A voltage signal is produced by the sensors. In the electrical control cabinet, the signals are transformed to a $4 - 20\text{mA}$ signal. An IBA PADU-8I converts the signal and an IBA PDA records them. Voltage signals tend to be perturbed by electromagnetic fields, and the longer the cable, the higher is the effect.

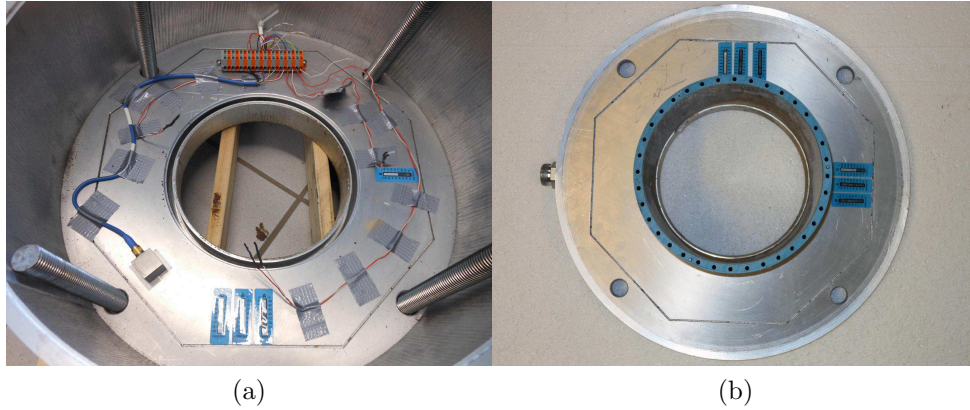


Figure 6.2.: View of the device after the first test run: (a) Top view of the base plate with outer ring. (b) Top view of the cover plate with inner ring upside down.

6.1.2. Results and conclusion

The first test successfully demonstrates the feasibility of cooling the device using pressurized air at an initial core temperature of 20°C . During the test, temperature measuring strips at different positions on the device indicate the maximum temperature. Inside the device, there are three indicators along the perimeter of the inner ring (left (Ind1), right (Ind2), and on the opposite side of the air inlet (Ind3)), two at the top surface of the bottom plate (left (Ind4) and on the opposite side of the inlet (Ind5)), and two at the lower surface of the cover plate (left (Ind6) and on the opposite side of the inlet (Ind7)). Outside indicators are located at the top surface of the cover plate (Ind8), on the big ring (Ind9), and on the lower surface of the bottom plate (Ind10).

Table 6.1 gives an overview of the maximum temperatures recorded during the first industrial test. Ind4 and Ind5 show 45°C and 49°C , respectively, both of which are well under the limit of 60°C . The indicators Ind1, Ind2, and Ind3 measure temperatures in a range of

Table 6.1.: An overview of the maximal observed temperatures at various positions on the device.

| | opposite outlet | left of inlet | opposite inlet | right of inlet |
|---------|-----------------|---------------|----------------|----------------|
| cover | 129°C | 116°C | - | - |
| ring | - | 88°C | 65°C | 82°C |
| bottom | - | 46°C | 49°C | - |
| outside | ≤ 204°C | 71°C | - | 127°C |

65°C ≤ T ≤ 90°C. These values agree very well with the values estimated from the numerical simulation discussed in section 3.2.3 and with the data obtained by the thermocouples (see Table 6.2), which are located along the perimeter of the inner cylinder at the same positions as those of the temperature measuring strips (Temp1, Temp2 and Temp3). From Table 6.2, it can be seen that the temperature significantly changes during the caster sequence. At the beginning, all thermocouples measure the same initial temperature of slightly more than 20°C. The temperature increases continuously during preheating. As can be seen in Figure 6.3, the slope of all thermocouples is almost identical, but the magnitude differs. According to the numerical simulation (see Figure 3.18a) we expect a temperature hotspot on either side of the air inlet (Ind1 and Ind2), but with identical magnitude. One reason for this could be an inaccurate alignment of the device. This leads to a very heterogeneously distributed air gap between the SEN and the LFF. In consequence, one side is exposed to considerably larger heat flux than the other side. This fact is supported by the results of the temperature measuring strips, which indicate different temperatures too. After preheating, a slide gate opens and liquid steel flows from the ladle in the tundish through the submerged entry nozzle into the mold. During the the first few minutes, the mold bursts into flames until a stable layer of casting powder covers the

mold level. The temperature rapidly increases and immediately drops down after casting powder has been applied. When the caster operates at steady state, the temperature continuously increases and approaches a stable value ($Temp1 \approx 85^\circ C$, $Temp2 \approx 73^\circ C$, and $Temp3 \approx 63^\circ C$). The maximal temperatures measured by the thermocouples occur after disconnection of the air supply at the end of the caster sequence. The highest temperature observed by the indicators is $130^\circ C$ at the top surface of the cover plate (Ind8). This is the surface directly under the tundish. To reduce the heat transfer, we propose to extend the rectangular plates by a minimum of 20mm. Basically, the cooling system works and is feasible for providing sufficiently low temperatures inside the device. However, the cooling system works at maximum power at all times, and there are no reserves to react in the event of an increasing thermal load. Moreover, the temperature distribution has strong gradients, particularly along the perimeter of the ring and in the radial direction on the bottom plate. Here, an optimization is strongly recommended.

Table 6.2.: An overview of the temperatures observed during the caster sequence at different time steps.

| Time | Process step | Temp 1 | Temp 2 | Temp3 |
|-------------|----------------------------|---------------|---------------|--------------|
| 13:30 | Start of preheating | $21^\circ C$ | $22^\circ C$ | $21^\circ C$ |
| 15:30 | End of preheating | $60^\circ C$ | $65^\circ C$ | $68^\circ C$ |
| 15:35 | After start of casting | $63^\circ C$ | $68^\circ C$ | $79^\circ C$ |
| 15:40 | Stable casting process | $60^\circ C$ | $65^\circ C$ | $75^\circ C$ |
| 16:33 | Ladle change | $62^\circ C$ | $72^\circ C$ | $85^\circ C$ |
| 17:42 | Remove blanketing material | $65^\circ C$ | $80^\circ C$ | $95^\circ C$ |
| 18:00 | After switch off cooling | $110^\circ C$ | $115^\circ C$ | $90^\circ C$ |

The results obtained by using a triaxial capacitive accelerometer (Kistler AG Type 8395A2) show that shocks and vibration occur during the caster sequence. However, their magnitude is low and we expect no

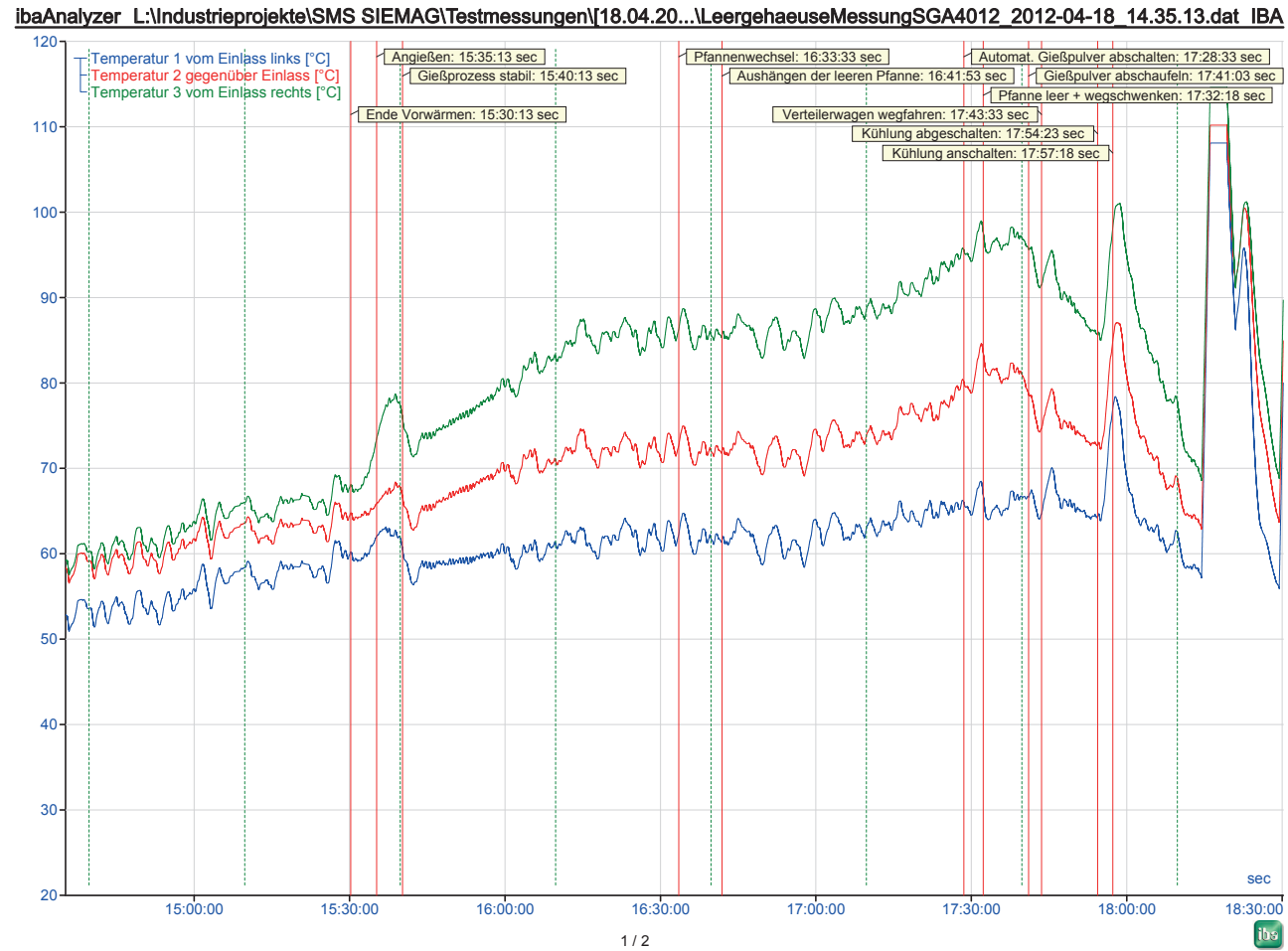


Figure 6.3.: Curve progression of the temperature along the perimeter during the caster sequence.

remarkable influences on the Lorentz force signal. Some events, for example ladle change, induce shocks, but the exact time of these events is known and could be attributed to peaks in the signals. Moreover, the test provides a considerable amount of information about the infrastructure in the steel plant. It is worse to adjust the device for welding. The device needs a kind of support to realize a constant air gap. This is important for cooling and for LFV.

6.2. Test of flow measurement

6.2.1. Preparation for the test

In the second test, a fully equipped LFF is used to measure the mass flux of liquid steel through the submerged entry nozzle. The device is identical to the one used in the first test. Some modifications based on the experiences from the first test are implemented. The rectangular steel plates are extended, and the air gap between cover the plate and the tundish increases to 30mm. In between, a layer of insulating material is added to reduce the heat flux from the tundish.

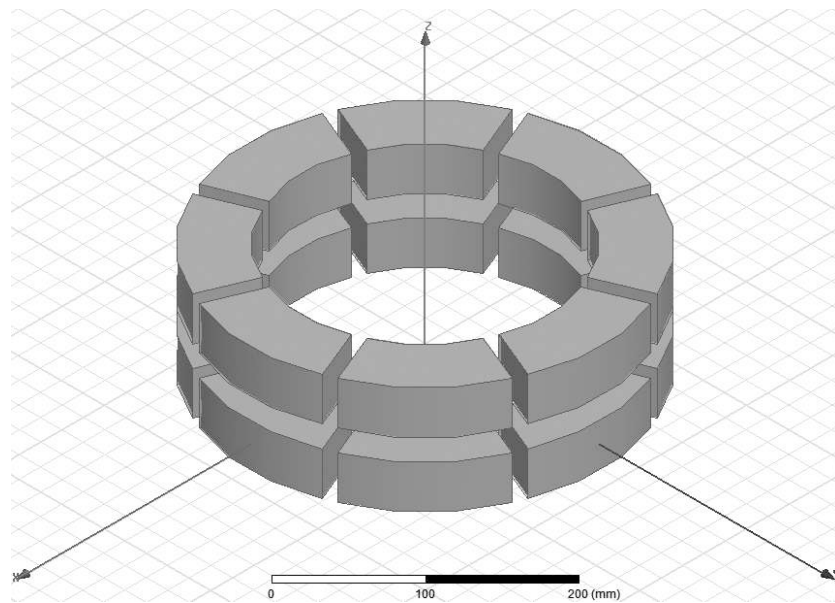
This time, the device contains three single point load cells (SCAIME AL15). Each load cell has a nominal load of 15kg to carry the weight of the magnet system and realize sufficient overload capacity. On the basis of the discussion in section 3.1.3, it is advisable to use a Halbach cylinder with 16 trapezoidal segments to achieve optimal results, but the assembly of the segments is difficult with the tools available in the laboratory. It needs hydraulic presses to achieve the high magnetic forces. In consideration of this limitations a simplified magnet system with a Maxwell coil magnetization based on proposal 3 has been built (see Figure 6.4b). The magnet system has an inner radius of $R_i = 115mm$, an outer radius of $R_o = 150mm$, and a height of $h = 120mm$ including the framework.

The distance between the rings is $s = 20\text{mm}$. Each ring consists of eight ring segments made of NdFeB with a quality of N52. The total weight including the framework, screws, and nuts sums up to 28kg. The magnet system is mounted on the load cells by a support ring made of stainless steel (1.4301) for exact load transmission. Again, the load cells are fixed by screws (M6) on the base plate. The electrical cabinet is extended by an additional data cable (14 wires) to implement the three force sensors by using the four-wire technique. The thermocouples operate by using the two-wire technique. Moreover, three additional transducers (SOEMER LAU 73.1) are used to convert the voltage output of the force sensors into a $4 - 20\text{mA}$ signal. Figure 6.5a shows the calibration curve of the force sensors and Figure 6.5b shows the calibration curve of the LFF determined using the dry calibration facility. We calculate the calibration constant by using linear regression and $k = 3.18\text{N} \cdot \text{s}/\text{m}$. In order to calculate the mass flux, we have to apply the scaling law (Eq.3.5) and multiply the signal with the mass density and the cross section of the SEN.

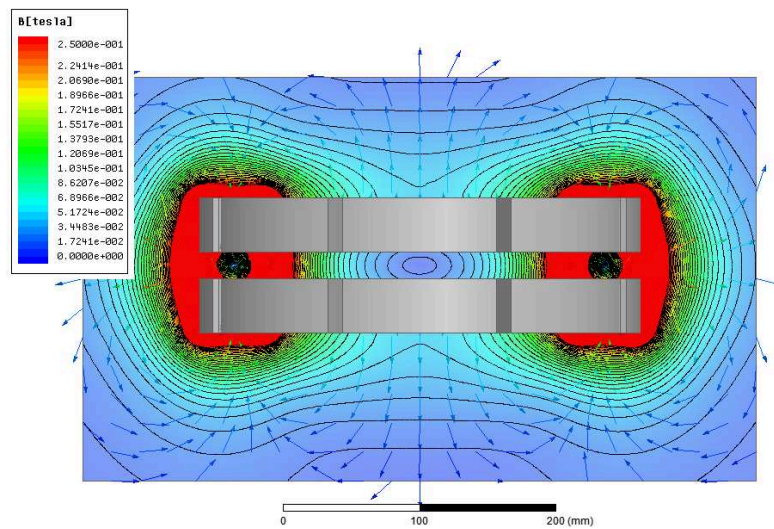
$$\dot{m}_{st}(t) = \frac{\rho_{st} \cdot \pi \cdot d^2}{4 \cdot k} \cdot \frac{\sigma_{st}}{\sigma_{Al}} \cdot F_L(t) \quad (6.1)$$

6.2.2. Results and conclusion

The flow measurement method of LFV produces a weak yet measurable signal. A translation of the measured Lorentz force in terms of mass flux is not possible, because many different types of interference act as noise to the signal. Basically, we determine the interferences as mechanical, electromagnetic, and thermal perturbations. Mechanical disturbances are vibrations and shocks during the casting process. For example, shocks occur during the ladle change or when foundrymen work with ferromagnetic tools next to the device. Another source for shocks

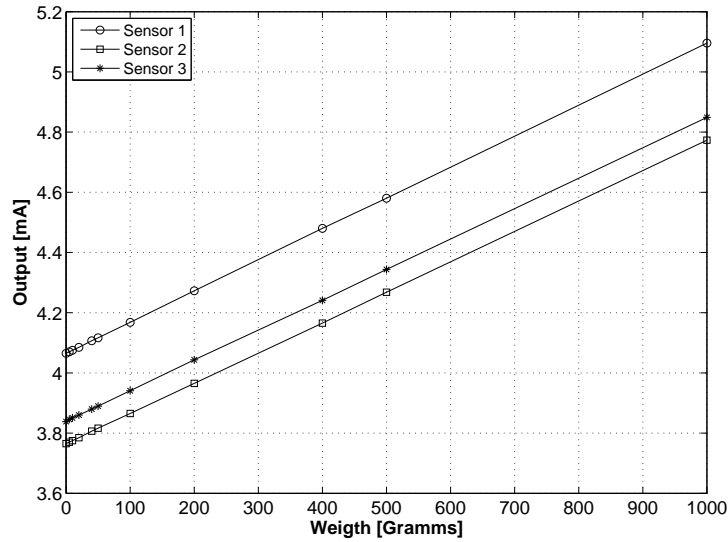


(a)

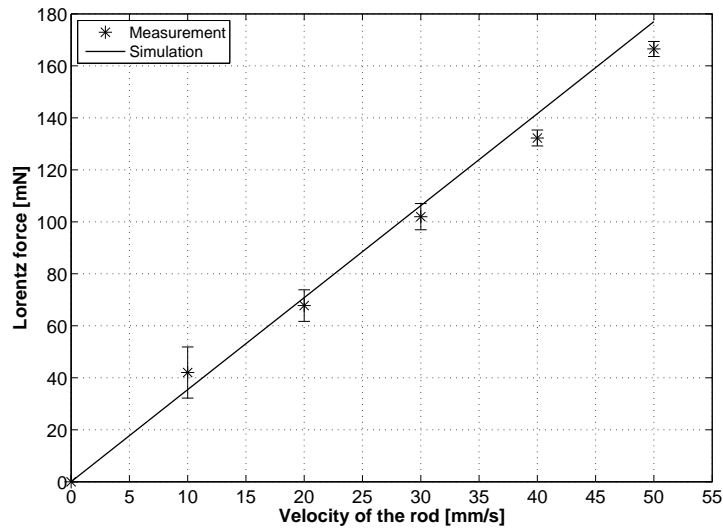


(b)

Figure 6.4.: Magnet system used for industrial test. A Maxwell Coil with distance $S=20\text{mm}$ (a) Screen shot of the numerical simulations. (b) Distribution of the magnetic field.



(a)



(b)

Figure 6.5.: Calibration of the LFF for pipe flows: (a) Calibration of the single point load cells SCAIME AL15. (b) Measured calibration curve of the prototype of a Lorentz force fowmeter for pipe flows compared to numerical results.

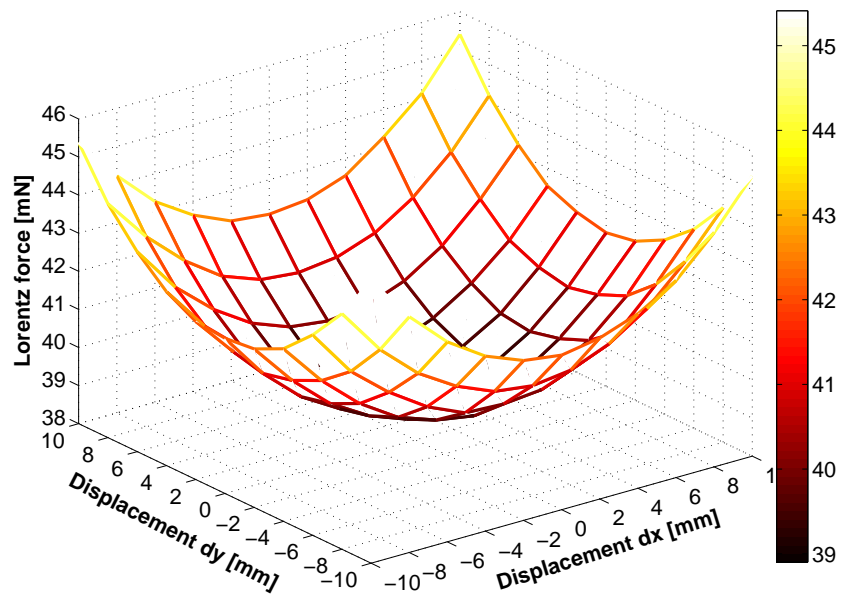


Figure 6.6.: Response surface of the Lorentz force for when the device is located in an off-axis position. The results are obtained by numerical simulations using a moving velocity of 10mm/s and an electrical conductivity of $22 \cdot 10^6 S/m$.

is the tundish movement that occur every 15min. Vibrations are caused by the air flow inside the cooling system and by the jet of liquid steel, which flows from the ladle into the tundish. All these mechanical disturbances can be identified and addressed to the corresponding events using the exact system time.

Thermal influences are dominant and heavily disturb the measurement. This time the air inside the device is heated from $21^{\circ}C$ to more than $65^{\circ}C$. Therefore the conditions seem to be different from those in the first test. Indeed, the diameter of the SEN is larger than in the first test, and the air gap between the device and the SEN reduces almost to zero. In consequence, all components slightly heat up inside the device. From the measurement, we conclude that temperature changes directly lead to a variation in the offset of the force sensors. Immediately after preheating, the temperature increases and force shows a temperature-related offset shift. Thermocouple 1 is located on the inner ring opposite the air inlet (Temp1), thermocouple 2 is located at the inner ring left of the air inlet (Temp2), and the third thermocouple (Temp3) is located on the right side of the air inlet in the gap between the magnet system and the housing (this is different from that in the first test). The temperature gradients cause mechanical stress on different parts of the device. Force sensor 1 drifts in the positive direction, and force sensor 2 in the negative direction. We suppose that the base plate is distorted by the temperature gradients.

Electromagnetic perturbations can be observed during the measurement. In the steel plant, huge electrical drives are used to transport the strand or to realize mold oscillation. Moreover, the caster operates with an electromagnetic mold level detector (VUHZ), which is located close to the device at the top edge of the mold. A Fourier transform of the measured force signal yields clear peaks at a frequency of $f = 2.5Hz$

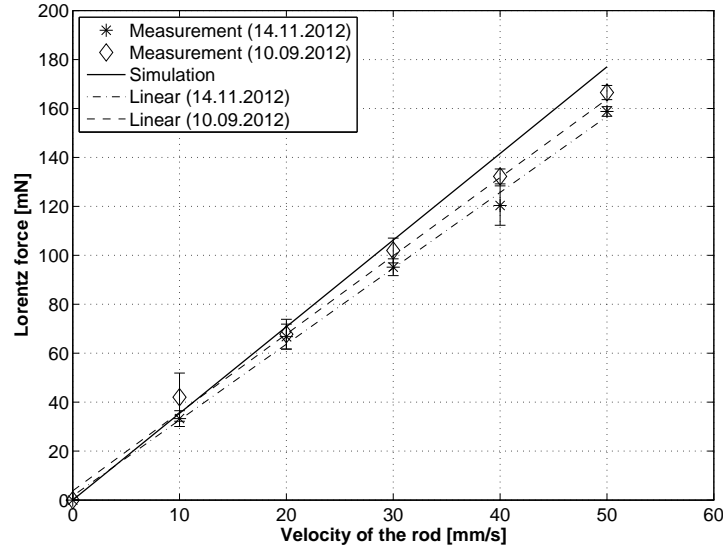


Figure 6.7.: Calibration of the load cells of type Scaime AL15 in the prototype.

and $f = k \cdot 10Hz$ with $k = 1, 2, \dots, n$. The frequency of $k \cdot 10Hz$ could be either from the voltage supply or from the natural frequency of the load cells.

A very important result is shown in Figure 6.7. Here, we compare the calibration curve before ($k = 3.18N \cdot s/m$) and after the test ($k = 3.36N \cdot s/m$). It can be seen that the test slightly affect the calibration constant of the device. However, the results are adequate, considering the rough handling of the device by the technicians. For example, during dismantling, the equipment is hit with a sledgehammer.

From the second test, we conclude that many influences disturb the measurement. The device needs to be redesigned to implement all experiences gained during the tests.

7. Summary and outlook

7.1. Summary

LFV is a non-contact flow measurement method based on the principles of magnetohydrodynamics. Because of the interaction of an externally applied magnetic field with a moving electrical conductor, eddy currents within the conductor lead to a Lorentz force, which drags the magnetic-field generating system along the flow direction. This force linearly depends on the velocity of the moving conductor and can be measured using an accurate force sensor. The measurement devices are called Lorentz force flowmeters.

The measurement of flow velocities in hot and aggressive fluids such as metal melts or glass melts is a widely unsolved problem. The solution to this problem is not restricted to academic interests. There is also a huge demand for reliable flow measurement devices in the industry. For instance, in continuous casting of steel a reliable, accurate and fast flow measurement method is required for efficient mold level control.

This PhD thesis describes the design and laboratory tests of an LFF for pipe flows. Owing the relevant industrial demand, the first prototype has been constructed for mold level control of a thick slab caster. In order to improve the current mold level control, the operators request a resolution of 1% of the time average mass flux \dot{m} and a response time of $T_{98} \leq 100ms$. Moreover, the devices must not disturb the production process. Therefore a maximal construction space of

$500\text{mm} \times 500\text{mm} \times 260\text{mm}$ is available. The investigations discussed in the present PhD theses are straightforward with a strong focus on the design and laboratory tests. In addition plant tests are performed to demonstrate the feasibility of the device under industrial conditions. Basically, it turns out that LFV is feasible for continuous casting of steel and other applications in metallurgy. The preferred cooling system (proposal 2) is feasible for maintaining the temperature inside the device at a moderate level of $T \leq 60^\circ\text{C}$. The cooling has no effect on solidification and it does not result in clogging of the SEN. Moreover, the electromagnetic mold level detection system (VUHZ) and the LFF do not influence each other. In detail, all of the different magnet systems proposals produce a considerable Lorentz force. After optimization using finite element method (FEM), it can be demonstrated that the most efficient magnet system is a Halbach cylinder with 16 trapezoidal segments made of NdFeB material with a quality of N52. During the the present study, two remarkable experiments were carried out. The first experiment investigated the response time T_{98} of the LFF and the second experiment focused on calibration and the investigation of sensitivity. Both experiments yielded significant results. The results of the first experiment indicate that the response time of an LFF is governed by two subsystems, namely, the magnet system and the force measurement system. The magnet system shows typical characteristics of a first-order transfer function and the force measurement system is known as a second-order transfer function. Combining both, these systems give a third-order transfer function with a response time of $T_{98} \approx 220\text{ms}$ in the case of solid aluminum rod with a diameter of 65mm and single point load cells made of aluminum. Keeping in mind that the response time depends on several material properties such as the electrical conductivity of the moving conductor, the diameter of the pipe, the spring constant, and the damping factor of the load cells, it could be possible to reduce the

response time to approximately $100ms$ in the case of liquid steel. From the second experiment, we obtain the calibration factor k of the device. Moreover, a strong nonlinear correlation between the Lorentz force and the diameter of the pipe could be found. The experiment gives information about the sensitivity when the device is located in an off-axis position in the x-y plane. It emphasizes that an off-axis position has an influence on the Lorentz force and a displacement of $\Delta x = \Delta y = 10mm$ to produce a measurable change in the Lorentz force.

7.2. Outlook

The first prototype of an LFF for pipe flows has been successfully tested in the laboratory and partially tested under industrial conditions in a steel plant. The results are promising but some improvements have to be made in the future. The results of the plant tests show that the measurement signal is greatly influenced by temperature gradients, mechanical shocks and vibrations, and electromagnetic noise. A redesign of the entire device is planned. For this redesigning process a detailed structural FEM analysis that considers the temperature distribution in the device should be performed.

Appendix

A. Tables

Table A.1.: Electrical conductivity of the aluminum rods [MS/m]

| Nr. | 80mm | 70mm | 65mm | 60mm | 40mm | 50mm | 30mm |
|-------------|-------|-------|-------|-------|-------|-------|-------|
| 1 | 20.28 | 19.51 | 20.41 | 19.07 | 19.41 | 19.96 | 20.08 |
| 2 | 20.28 | 19.46 | 20.60 | 19.18 | 19.47 | 19.88 | 20.12 |
| 3 | 20.26 | 19.44 | 20.58 | 19.13 | 19.44 | 19.98 | 20.15 |
| 4 | 20.24 | 19.41 | 20.60 | 19.06 | 19.46 | 19.98 | 20.10 |
| 5 | 20.25 | 19.35 | 20.50 | 19.11 | 19.45 | 20.00 | 20.12 |
| 6 | 20.20 | 19.48 | 20.56 | 18.96 | 19.43 | 19.83 | 20.01 |
| 7 | 20.20 | 19.45 | 20.55 | 18.94 | 19.45 | 19.83 | 20.09 |
| 8 | 20.21 | 19.37 | 20.47 | 18.93 | 19.42 | 19.85 | 20.00 |
| 9 | 20.19 | 19.45 | 20.53 | 18.95 | 19.39 | 19.84 | 20.06 |
| 10 | 20.21 | 19.41 | 20.49 | 18.94 | 19.37 | 19.80 | 20.03 |
| Mean | 20.23 | 19.43 | 20.53 | 19.03 | 19.43 | 19.90 | 20.08 |
| STD | 0.04 | 0.05 | 0.06 | 0.09 | 0.03 | 0.08 | 0.05 |

Table A.2.: Electrical conductivity of the copper rods [MS/m].

| Nr. | 65mm | 60mm | 40mm | 50mm | 30mm |
|-------------|-------|-------|-------|-------|-------|
| 1 | 58.33 | 58.36 | 59.02 | 58.28 | 58.26 |
| 2 | 58.01 | 58.68 | 59.02 | 57.82 | 58.19 |
| 3 | 58.34 | 58.61 | 58.99 | 58.18 | 58.28 |
| 4 | 58.55 | 58.97 | 59.01 | 57.99 | 58.47 |
| 5 | 58.27 | 58.40 | 59.01 | 58.01 | 58.40 |
| 6 | 58.48 | 58.54 | 59.20 | 57.84 | 58.09 |
| 7 | 58.48 | 58.84 | 59.20 | 57.84 | 57.83 |
| 8 | 58.36 | 58.41 | 58.91 | 57.87 | 57.94 |
| 9 | 58.44 | 58.68 | 58.62 | 57.95 | 57.75 |
| 10 | 58.27 | 58.71 | 58.62 | 57.74 | 57.54 |
| Mean | 58.35 | 58.62 | 58.96 | 57.95 | 58.08 |
| STD | 0.15 | 0.20 | 0.20 | 0.17 | 0.30 |

Table A.3.: Diameter of the aluminum rods [mm]

| Nr. | 80mm | 70mm | 65mm | 60mm | 50mm | 40mm | 30mm |
|------|--------------|--------------|--------------|--------------|--------------|--------------|--------------|
| 1 | 79.97 | 70.53 | 65.17 | 60.22 | 50.14 | 40.19 | 30.06 |
| 2 | 79.93 | 70.59 | 65.15 | 60.27 | 50.05 | 40.16 | 30.05 |
| 3 | 79.88 | 70.62 | 65.11 | 60.20 | 50.08 | 40.13 | 30.05 |
| 4 | 79.89 | 70.60 | 65.12 | 60.12 | 50.02 | 40.22 | 30.06 |
| 5 | 79.92 | 70.71 | 65.07 | 60.22 | 50.08 | 40.18 | 30.07 |
| 6 | 80.01 | 70.62 | 65.09 | 60.16 | 50.13 | 40.17 | 30.06 |
| 7 | 79.88 | 70.66 | 65.10 | 60.32 | 50.07 | 40.16 | 30.12 |
| 8 | 79.92 | 70.61 | 65.08 | 60.31 | 50.08 | 40.18 | 30.16 |
| 9 | 79.99 | 70.58 | 65.08 | 60.16 | 50.15 | 40.16 | 30.15 |
| 10 | 80.02 | 70.65 | 65.15 | 60.14 | 50.02 | 40.15 | 30.12 |
| Mean | 79.94 | 70.62 | 65.11 | 60.21 | 50.08 | 40.17 | 30.09 |
| Std | 0.05 | 0.05 | 0.03 | 0.07 | 0.04 | 0.02 | 0.04 |

Table A.4.: Diameter of the copper rods [mm]

| | 80mm | 70mm | 65mm | 60mm | 50mm | 40mm | 30mm |
|------|--------------|--------------|--------------|--------------|--------------|--------------|--------------|
| 1 | 80.59 | 70.46 | 65.65 | 60.11 | 50.02 | 40.13 | 30.06 |
| 2 | 80.56 | 70.45 | 65.64 | 60.15 | 50.09 | 40.09 | 30.07 |
| 3 | 80.57 | 70.51 | 65.66 | 60.15 | 50.06 | 40.12 | 30.05 |
| 4 | 80.55 | 70.52 | 65.68 | 60.02 | 50.03 | 40.10 | 30.06 |
| 5 | 80.54 | 70.41 | 65.71 | 60.03 | 50.07 | 40.09 | 30.05 |
| 6 | 80.64 | 70.44 | 65.83 | 60.02 | 50.01 | 40.16 | 30.06 |
| 7 | 80.72 | 70.50 | 65.68 | 60.14 | 50.02 | 10.12 | 30.09 |
| 8 | 80.69 | 70.49 | 65.71 | 60.10 | 50.05 | 40.07 | 30.07 |
| 9 | 80.52 | 70.50 | 65.72 | 60.15 | 50.03 | 40.05 | 30.06 |
| 10 | 80.67 | 70.46 | 65.69 | 60.10 | 50.07 | 40.05 | 30.10 |
| Mean | 80.61 | 70.47 | 65.70 | 60.10 | 50.05 | 37.10 | 30.07 |
| STD | 0.07 | 0.03 | 0.05 | 0.05 | 0.03 | 8.99 | 0.02 |

Table A.5.: Properties of NdFeB [Source: www.supermagnete.de].

| Quality | Br | | bHc | | iHc | | (BxH)max | | Tc |
|------------|-----------|-----------|------------|----------|-------|--------|----------|----------------------|-------|
| | [kG] | [T] | [kOe] | [kA/m] | [kOe] | [kA/m] | [MGOe] | [kJ/m ³] | [°C] |
| N30 | 10.8-11.2 | 1.08-1.12 | 9.8-10.5 | 780-836 | ≥ 12 | ≥ 955 | 28-30 | 223-239 | ≤ 80 |
| N33 | 11.4-11.7 | 1.14-1.17 | 10.03.2011 | 820-876 | ≥ 12 | ≥ 955 | 31-33 | 247-263 | ≤ 80 |
| N35 | 11.7-12.1 | 1.17-1.21 | 10.8-11.5 | 860-915 | ≥ 12 | ≥ 955 | 33-35 | 263-279 | ≤ 80 |
| N38 | 12.2-12.6 | 1.22-1.26 | 10.8-11.5 | 860-915 | ≥ 12 | ≥ 955 | 36-38 | 287-303 | ≤ 80 |
| N40 | 12.6-12.9 | 1.26-1.29 | 10.5-12.0 | 860-955 | ≥ 12 | ≥ 955 | 38-40 | 303-318 | ≤ 80 |
| N42 | 12.9-13.2 | 1.29-1.32 | 10.8-12.0 | 860-955 | ≥ 12 | ≥ 955 | 40-42 | 318-334 | ≤ 80 |
| N45 | 13.2-13.7 | 1.32-1.37 | 10.8-12.5 | 860-995 | ≥ 12 | ≥ 955 | 43-45 | 342-358 | ≤ 80 |
| N48 | 13.7-14.2 | 1.37-1.42 | 10.8-12.5 | 860-995 | ≥ 12 | ≥ 955 | 45-48 | 358-382 | ≤ 80 |
| N50 | 14.0-14.6 | 1.40-1.46 | 10.8-12.5 | 860-995 | ≥ 12 | ≥ 955 | 47-51 | 374-406 | ≤ 80 |
| N52 | 14.2-14.7 | 1.42-1.47 | 10.8-12.5 | 860-995 | ≥ 12 | ≥ 955 | 48-53 | 380-422 | ≤ 80 |
| 27H | 10.2-10.6 | 1.02-1.06 | 9.5-10.1 | 756-804 | ≥ 17 | ≥ 1353 | 25-27 | 199-215 | ≤ 120 |
| 30H | 10.8-11.2 | 1.08-1.12 | 10.1-10.6 | 804-844 | ≥ 17 | ≥ 1353 | 28-30 | 223-239 | ≤ 120 |
| 33H | 11.4-11.7 | 1.14-1.17 | 10.03.2011 | 820-876 | ≥ 17 | ≥ 1353 | 31-33 | 247-263 | ≤ 120 |
| 35H | 11.7-12.1 | 1.17-1.21 | 10.8-11.5 | 860-915 | ≥ 17 | ≥ 1353 | 33-35 | 263-279 | ≤ 120 |
| 38H | 12.2-12.6 | 1.22-1.26 | 10.8-11.5 | 860-915 | ≥ 17 | ≥ 1353 | 36-38 | 287-303 | ≤ 120 |
| 40H | 12.6-12.9 | 1.26-1.29 | 10.08.2012 | 860-955 | ≥ 17 | ≥ 1353 | 38-40 | 303-318 | ≤ 120 |
| 42H | 12.9-13.2 | 1.29-1.32 | 10.08.2012 | 860-955 | ≥ 17 | ≥ 1353 | 40-42 | 318-334 | ≤ 120 |
| 44H | 13.2-13.6 | 1.32-1.36 | 10.08.2013 | 860-1035 | ≥ 17 | ≥ 1353 | 42-44 | 334-350 | ≤ 120 |
| 48H | 13.7-14.2 | 1.37-1.42 | 10.8-12.5 | 860-995 | ≥ 17 | ≥ 1353 | 45-48 | 358-382 | ≤ 120 |

B. Figures

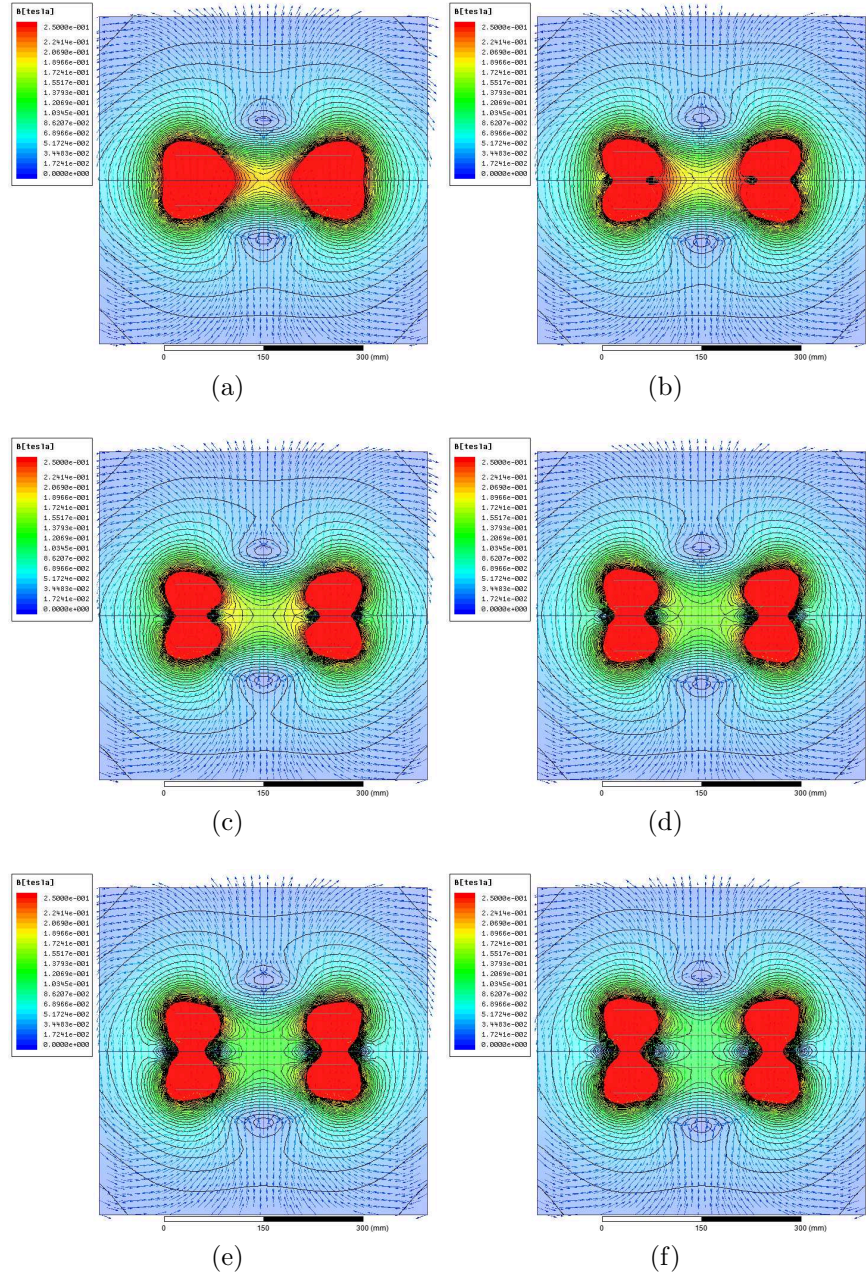


Figure B.1.: Distribution of the magnetic field of a Helmholtz Coil for several instants of S . (a) $S=0\text{mm}$ (b) $S=10\text{mm}$ (c) $S=20\text{mm}$ (d) $S=30\text{mm}$ (e) $S=40\text{mm}$ (f) $S=50\text{mm}$.

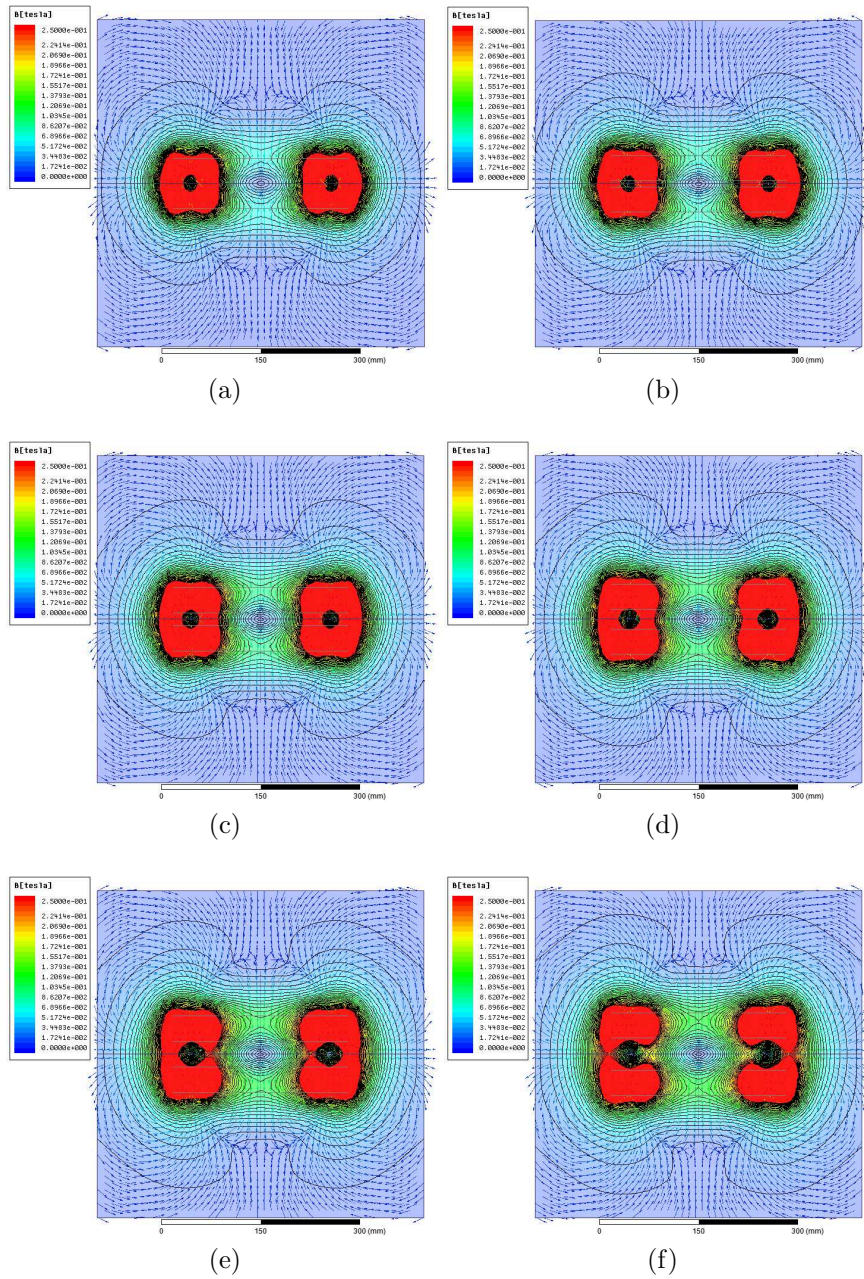
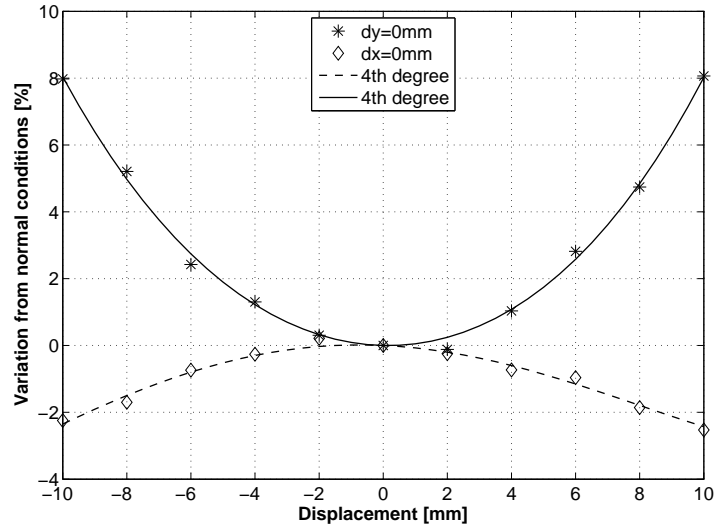
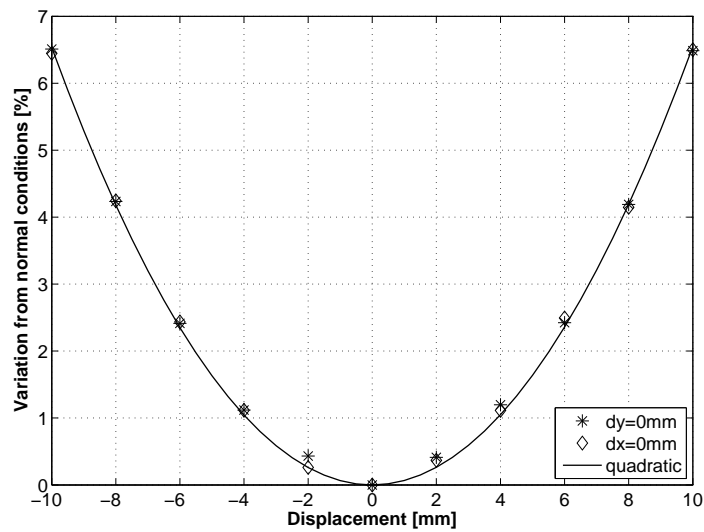


Figure B.2.: Distribution of the magnetic field of a Maxwell Coil for several instants of S . (a) $S=0\text{mm}$ (b) $S=10\text{mm}$ (c) $S=20\text{mm}$ (d) $S=30\text{mm}$ (e) $S=40\text{mm}$ (f) $S=50\text{mm}$.

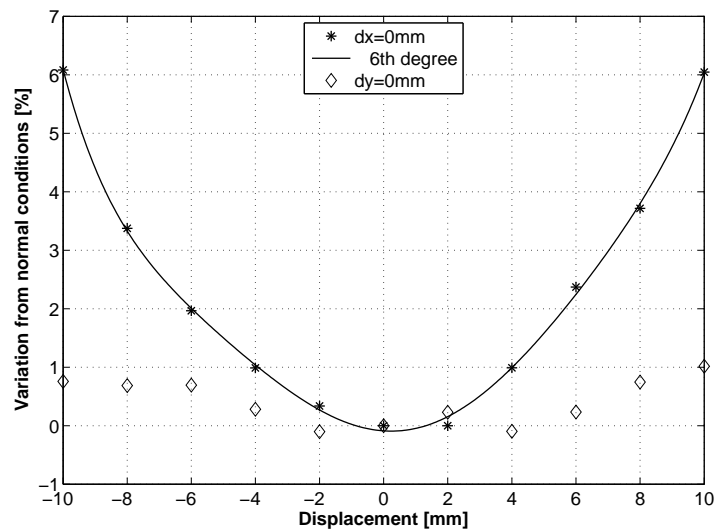


(a)

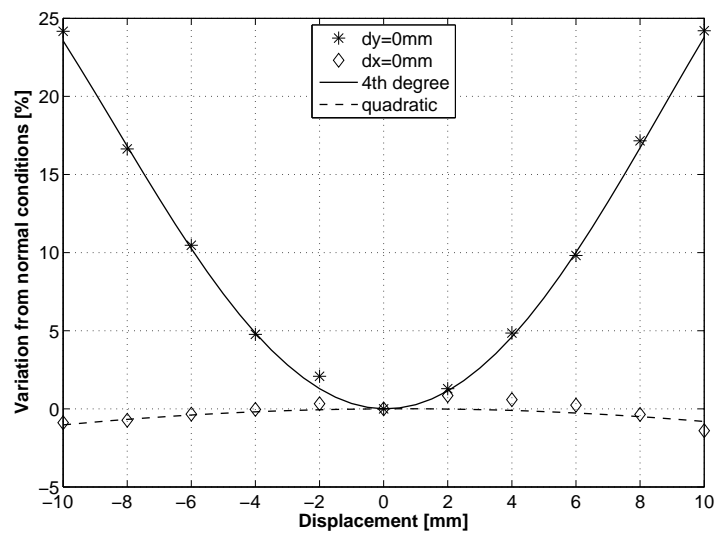


(b)

Figure B.3.: Results of the sensitivity analysis of the magnet systems.
 (a) Magnet with iron yoke (b) Ring magnet system



(a)



(b)

Figure B.4.: Results of the sensitivity analysis of the magnet systems.
(a) Halbach Cylinder (b) Halbach Array

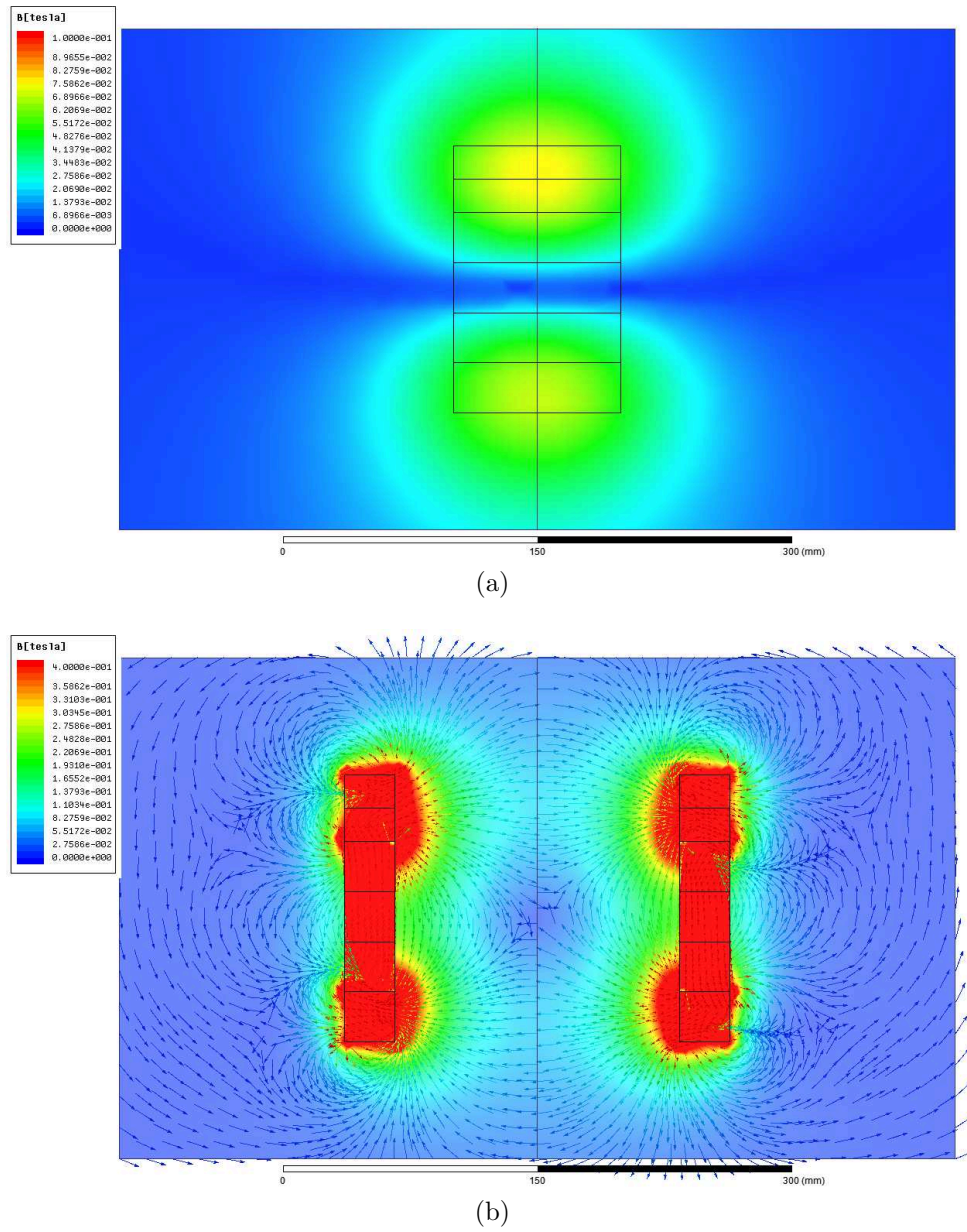


Figure B.5.: Results of the sensitivity analysis of the magnet systems.
 (a) Magnet with iron yoke (b) Ring magnet system (c) Halbach Cylinder (d) Halbach Array

Bibliography

- [1] J. Czarske and S. Eckert. Messtechnik in der Magnetofluidodynamik. *TM-Tech. Mess.*, 79(9):387–388, 2012.
- [2] M. Faraday. Experimental researches in electricity. *Phil. Trans. R. Soc. Lond.*, 122:125–162, 1832.
- [3] J. A. Shercliff. *The Theory Of Electromagnetic Flow-Measurement*. Cambridge University Press, Cambridge, 1 edition, 1962.
- [4] P. A. Davidson. *An Introduction to Magnetohydrodynamics*. Cambridge University Press, Cambridge, 1 edition, 2001.
- [5] J. A. Shercliff. *A Textbook of Magnetohydrodynamics*. Pergamon Press, New York, 1 edition, 1965.
- [6] H. K. Moffatt. *Magnetic Field Generation in Electrically Conducting Fluids*. Cambridge University Press, Cambridge, 1 edition, 1978.
- [7] J. C. Maxwell. A dynamical theory of the electromagnetic field. *Phil. Trans. R. Soc. Lond.*, 155:459–512, 1865.
- [8] J. D. Jackson. *Classical Electrodynamics*. John Wiley Sons, New York, 3 edition, 1999.
- [9] R. P. Feynman, R. B. Leighton, and M. Sands. *Lectures on Physics (The Definitive Edition) Vol.II*. Addison Wesley, Massachusetts, 2 edition, 2005.
- [10] H. H. Woodson and J. R. Melcher. *Electromechanical Dynamics*, volume 1. John Wiley Sons, New York, New York, 1 edition, 1968.
- [11] R. P. Feynman, R. B. Leighton, and M. Sands. *Lectures on Physics (The Definitive Edition) Vol.I*. Addison Wesley, Massachusetts, 2 edition, 2005.
- [12] J. Hemp. Theory of eddy currents in electromagnetic flowmeters. *J. Phys. D: Appl. Phys.*, 24(3):244, 1991.
- [13] R. Klein. *MHD experiments on quasi two-dimensional and three-dimensional liquid metal flows*. PhD thesis, Coventry University, 2010.

-
- [14] O. Darrigol. *Electrodynamics from Ampere to Einstein*. Oxford University Press, Oxford, 1 edition, 2000.
- [15] E. Votyakov and A. Thess. Interaction of a magnetic dipole with a slowly moving electrically conducting plate. *J. Eng. Math.*, 77:147–161, 2012.
- [16] A. Thess, E. Votyakov, B. Knaepen, and O. Zikanov. Theory of the Lorentz force flowmeter. *New J. Phys.*, 9(299), 2007.
- [17] A. Thess, E. Votyakov, and Y. Kolesnikov. Lorentz force flowmeter. *Phys. Rev. Lett.*, 96(16), 2006.
- [18] Y. Kolesnikov, C. Karcher, and A. Thess. Lorentz force flowmeter for liquid aluminum: Laboratory experiments and plant tests. *Metall. Mater. Trans. B*, 42:441–450, 2011.
- [19] R. Klein, C. Weidemann, X. Wang, M. Gramß, A. Alferenok, A. Thieme, Y. Kolesnikov, C. Karcher, and A. Thess. Contactless flow measurement of liquid metals using Lorentz force velocimetry. *TM-Tech. Mess.*, 79(9):394–398, 2012.
- [20] C. Weidemann, A. Thess, D. Lieftucht, and M. Reifferscheid. Application of Lorentz force velocimetry in continuous casting of steel. In *Proceedings of the 5th International Congress on the Science and Technology of Steelmaking*, 2012.
- [21] C. Heinicke. Measurement of local velocities in turbulent liquid metal duct flows using Lorentz force velocimetry. In *Proceedings of the International Scientific Colloquium*, pages 233–238, 2011.
- [22] C. Heinicke. *Local Lorentz Force Velocimetry for liquid metal duct flows*. PhD thesis, Ilmenau University of Technology, 2012.
- [23] I. Rahneberg, F. Hilbrunner, and T. Fröhlich. Novel concept of a high precision 6-dof force/torque transducer. In *Proceedings of the International Scientific Colloquium*, pages 233–238, 2011.
- [24] M. Kirpo, S. Tympel, T. Boeck, D. Krasnov, and A. Thess. Electromagnetic drag on a magnetic dipole near a translating conducting bar. *J. Appl. Phys.*, 109(11):113921, 2011.
- [25] S. Tympel, D. Krasnov, T. Boeck, and J. Schumacher. Laminar magnetohydrodynamic duct flow in the presence of a magnetic dipole. *PAMM*, 11(1):671–672, 2011.

-
- [26] G. Pulugundla. *Numerical Modelling of Liquid Metal Flows Interacting with Strongly Inhomogeneous Magnetic Fields*. PhD thesis, Ilmenau University of Technology, 2012.
- [27] A. Alferenok. *Numerical simulation and optimization of the magnet system for the Lorentz Force Velocimetry of low-conducting materials*. PhD thesis, Ilmenau University of Technology, 2012.
- [28] M. Werner and B. Halbedel. Optimization of ndfeb magnet arrays for improvement of Lorentz force velocimetry. *IEEE Trans. Magn.*, 48(11), 2012.
- [29] M. Werner. *Design, Optimierung, Realisierung und Test von passiven Magnet-systemen für die Lorentzkraftanemometrie an Elektrolyten*. PhD thesis, Ilmenau University of Technology, 2012.
- [30] A. Wegfraß, C. Diethold, M. Werner, T. Fröhlich, B. Halbedel, F. Hilbrunner, C. Resagk, and A. Thess. A universal noncontact flowmeter for liquids. *Appl. Phys. Lett.*, 100(19):194103, 2012.
- [31] A. Wegfraß, C. Diethold, M. Werner, A. Alferenok, C. Resagk, T. Fröhlich, B. Halbedel, U. Lüdtke, and A. Thess. Contactless flow measurement of electrolytes using Lorentz force velocimetry. *TM-Tech. Mess.*, 79(9):399–402, 2012.
- [32] A. Wegfraß, C. Diethold, M. Werner, C. Resagk, T. Fröhlich, B. Halbedel, and A. Thess. Flow rate measurement of weakly conducting fluids using Lorentz force velocimetry. *Meas. Sci. Technol.*, 23(10):105307, 2012.
- [33] A. Wegfraß. *Experimentelle Untersuchungen zur Anwendbarkeit der Lorentzkraft-Anemometrie auf schwach leitfähige Fluide*. PhD thesis, Ilmenau University of Technology, 2012.
- [34] A. Viré, B. Knaepen, and A. Thess. Lorentz force velocimetry based on time-of-flight measurements. *Phys. Fluids*, 22(12):125101, 2010.
- [35] D. Jian and C. Karcher. Electromagnetic flow measurements in liquid metals using time-of-flight Lorentz force velocimetry. *Meas. Sci. Technol.*, 23(7):074021, 2012.
- [36] D. Jian, C. Karcher, X. Xu, A. Deng, E. Wang, and A. Thess. Development of a non-contact electromagnetic surface velocity sensor for molten metal flow. In *Proceedings of the 7th International Congress on Electromagnetic Processing of Materials*, October 2012.
- [37] J. Priede, D. Buchenau, and G. Gerbeth. Single-magnet rotary flowmeter for liquid metals. *J.Appl.Phys.*, 110, 2011.

-
- [38] J. Priede, D. Buchenau, and G. Gerbeth. Force-free and contactless sensor for electromagnetic flowrate measurements. *Magnetohydrodynamics*, 45(3):451–458, 2009.
- [39] D. Buchenau, G. Gerbeth, and J. Priede. Contactless flow rate measurements in metallic melts. *TM-Tech. Mess.*, 79(9):389–393, 2012.
- [40] J. Priede, D. Buchenau, G. Gerbeth, and S. Eckert. Verfahren und Anordnung zur kontaktlosen Messung des Durchflusses elektrisch leitfähiger Medien, 2009. Patent.
- [41] J. Priede, D. Buchenau, and G. Gerbeth. Contactless electromagnetic phase-shift flowmeter for liquid metals. *Meas. Sci. Technol.*, 22(5):055402, 2011.
- [42] S. Eckert and G. Gerbeth. Application of the ultrasound doppler method for flow measurements in liquid metals. *TM-Tech. Mess.*, 79(9):410–416, 2012.
- [43] F. Stefani, G. Gerbeth, T. Gundrum, and T. Wondrak. Principles and applications of the contactless inductive flow tomography. *TM-Tech. Mess.*, 79(9):417–423, 2012.
- [44] R. P. Uhlig, M. Zec, M. Ziolkowski, H. Brauer, and A. Thess. Lorentz force sismometry: A contactless method for electrical conductivity measurements. *J. Appl. Phys.*, 111(9):094914, 2012.
- [45] R. P. Uhlig, M. Zec, H. Brauer, and A. Thess. Lorentz force eddy current testing: a prototype model. *J. Nondestruct. Eval.*, pages 1–16, 2012.
- [46] B. Petkovic, J. Haueisen, M. Zec, R. P. Uhlig, H. Brauer, and M. Ziolkowski. An approximation method for crack reconstruction in Lorentz force eddy current testing. In *12th International Workshop on Optimization and Inverse Problems in Electromagnetism*, September 2012.
- [47] R. P. Uhlig. *About the Identification of Material Defects in Metallic Materials Using Lorentz Force Eddy Current Testing Fundamentals, Metrological Implementation and Verification of Results*. PhD thesis, Ilmenau University of Technology, 2012.
- [48] M. Zec. *Theory and Numerical Modelling of Lorentz Force Eddy Current Testing*. PhD thesis, Ilmenau University of Technology, 2012.
- [49] E. du Treemolet de Lacheisserie, D. Gignoux, and M. Schlenker. *Magnetism: Fundamentals*. Springer Verlag, New York, 1 edition, 2004.
- [50] E. du Treemolet de Lacheisserie, D. Gignoux, and M. Schlenker. *Magnetism: Materials and applications*. Springer Verlag, New York, 1 edition, 2005.

-
- [51] E. Kallenbach, R. Eick, P. Quendt, T. Stroela, K. Feindt, and M. Kallenbach. *Elektromagnete: Grundlagen, Berechnung, Entwurf und Anwendung*. Vieweg Verlag, Wiesbaden, 3 edition, 2008.
- [52] J. F. Herbst and J. J. Croat. Neodymium-iron-boron permanent magnets. *J. Magn. Magn. Mater.*, 100(13):57 – 78, 1991.
- [53] M. Kramer, R. Mc Callum, I. Anderson, and S. Constantinides. Prospects for non-rare earth permanent magnets for traction motors and generators. *JOM Journal of the Minerals, Metals and Materials Society*, 64(7):752–763, 2012. 10.1007/s11837-012-0351-z.
- [54] G. Mueller and C. Groth. *FEM fuer Praktiker: Grundlagen*, volume 1. Expert-Verlag, Renningen, 8 edition, 2007.
- [55] W. Schaetzing. *FEM fuer Praktiker: Elektrotechnik*, volume 4. Expert-Verlag, Renningen, 2 edition, 2009.
- [56] V. Minchenya, C. Karcher, Y. Kolesnikov, and A. Thess. Calibration of the Lorentz force flowmeter. *Flow Meas. Instrum.*, 22(3):242 – 247, 2011.
- [57] F. Mach, P. Karban, and I. Dolezel. Induction heating of cylindrical nonmagnetic ingots by rotation in static magnetic field generated by permanent magnets. *J. Comput. Appl. Math.*, 236(18):4732 – 4744, 2012.
- [58] H. Kronmueller and S. Parkin. *Handbook of Magnetism and Advanced Magnetic Materials*, volume 1. John Wiley & Sons, Amsterdam, 1 edition, 2007.
- [59] C. Stelian, A. Alferenok, U. Lüdtke, Y. Kolesnikov, and A. Thess. Optimization of a Lorentz force flowmeter by using numerical modeling. *Meas. Sci. Technol.*, 47(3):273–282, 2011.
- [60] O. Traisigkhachol, L. Rissing, and H. H. Gatzel. A concept for characterization and analysis of the readout of soft magnetic thin-films. *ECS Trans.*, 16(45):269–282, 2009.
- [61] E. R. Andrew, M. Kempka, S. Sagnowski, and E. Szczesniak. *Novel Gradient Coils for Magnetic Resonance Microscopy*, pages 683–693. Wiley-VCH Verlag, 2007.
- [62] K. Halbach. Design of permanent multipole magnets with oriented rare earth cobalt materials. *Nucl. Instrum. Methods*, 169(1):1–10, 1980.
- [63] K. Halbach. Physical and optical properties of rare earth cobalt magnets. *Nucl. Instrum. Methods*, 187(1):109–117, 1981.

-
- [64] J. Mallinson. One-sided fluxes – a magnetic curiosity? *IEEE Transactions on Magnetism*, 9(4):678 – 682, dec 1973.
- [65] Z. Q. Zhu and D. Howe. Halbach permanent magnet machines and applications: a review. *IEE Proc.-Electr. Power Appl.*, 148(4):299–308, 2001.
- [66] K. Halbach. Some concepts to improve the performance of dc electromagnetic wigglers. *Nucl. Instrum. Meth. A*, 250(1):115–119, 1986.
- [67] A. Aleferenok and U. Luedtke. Optimization of the magnet system for the Lorentz force velocimetry of low conducting materials. In *Proceedings of the 3rd International Conference on Engineering Optimization*, 2012.
- [68] M. Werner, E. Raedlein, and B. Halbedel. Numerical study of magnet systems for Lorentz force velocimetry in electrically low conducting fluids. In *Proceedings of the International Scientific Colloquium*, pages 233–238, 2010.
- [69] M. Werner and B. Halbedel. Anwendung von Halbacharrays in der Lorentzkraftanemometrie. In *Proceedings of Workshop Elektroprozessechnik*, 2011.
- [70] P. von Boeckh and T. Wetzel. *Heat Transfer: Basics and Practice*. Springer, Heidelberg, 1 edition, 2011.
- [71] F. P. Incropera, D. P. DeWitt, T. L. Bergman, and A. S. Lavine. *Fundamentals of Heat and Mass Transfer*. John Wiley and Sons, New York, 6 edition, 2006.
- [72] *VDI-Wärmeatlas*. Springer-Verlag, Heidelberg, 2006.
- [73] X. Wei-Chau. *Differential Equations for Engineers*. Cambridge University Press, Cambridge, 1 edition, 2010.
- [74] E. Hering and H. Steinhart. *Taschenbuch der Mechatronik*. Hanser Fachbuchverlag, Muenchen, 1 edition, 2005.
- [75] Bodo Heimann, Wilfried Gerth, and Karl Popp. *Mechatronik*. Hanser Fachbuchverlag, Muenchen, 2 edition, 2003.
- [76] H. Walter. *Grundkurs Regelungstechnik: Grundlagen für Bachelorstudiengänge aller technischen Fachrichtungen und Wirtschaftsingenieure*. Vieweg + Teubner Verlag, Wiesbaden, 2 edition, 2009.
- [77] J. R. Taylor. *Classical Mechanics*. University Science Books, 1 edition, 2005.
- [78] P.H. Roberts. *An Introduction to Magnetohydrodynamics*. Cambridge University Press, Cambridge, 1 edition, 1967.

-
- [79] R. Moreau. *Magnetohydrodynamics*. Kluwer Academic Publishers, Dordrecht, 1 edition, 1990.
- [80] R. L. Parker. Reconnexion of lines of force in rotating spheres and cylinders. *P. Roy. Soc. Lond. A. Mat.*, 291(1424):60–72, 1966.
- [81] M. Perry and T. Jones. Eddy current induction in a solid conducting cylinder with a transverse magnetic field. *IEEE T. Magn.*, 14(4):227 – 232, jul 1978.
- [82] H. H. Woodson and J. R. Melcher. *Electromechanical Dynamics*, volume 2. John Wiley Sons, New York, New York, 1 edition, 1968.
- [83] R. S. Peckover and N. O. Weiss. Convection in the presence of magnetic fields. *Comput. Phys. Commun.*, 4(3):339 – 344, 1972.
- [84] E. C. Bullard, C. Freedman, H. Gellman, and J. Nixon. The westward drift of the earth’s magnetic field. *Phil. Trans. R. Soc. Lond. A*, 243(859):67–92, 1950.
- [85] P. H. Roberts and G. A. Glatzmaier. Geodynamo theory and simulations. *Rev. Mod. Phys.*, 72:1081–1123, 2000.
- [86] A. Gailitis, O. Lielausis, E. Platacis, G. Gerbeth, and F. Stefani. The riga dynamo experiment. *Surv. Geophys.*, 24:247–267, 2003.
- [87] J. Crank. *The Mathematics of Diffusion*. Oxford University Press, Oxford, 2 edition, 1975.
- [88] J.W.Thomas. *Numerical Partial Differential Equations: Finite Difference Methods*. Springer US, New York, 2 edition, 1998.
- [89] A. Michalski. Dry calibration procedure of electromagnetic flowmeters for open channels. *IEEE Trans. Instrum. Meas.*, 49(2):434, 2000.
- [90] R. Baker R. Al-Rabeh. On the ability to dry calibrate an electromagnetic flowmeter. *J. Phys. E: Sci. Instrum.*, 19:203, 1986.
- [91] V. Minchenyaa, C. Karcher, Y. Kolesnikov, and A. Thess. Calibration of the Lorentz force flowmeter. In *Proceedings of the international scientific colloquium Modeling for electromagnetic processing*, pages 303–306, October 2008.
- [92] V. Minchenya, Ch. Karcher, Y. Kolesnikov, and A. Thess. Dry calibration of the Lorentz force flowmeter. *Magnetohydrodynamics*, 45(4):569–578, 2009.
- [93] X. Wang, Y. Kolesnikov, and A. Thess. Numerical calibration of a Lorentz force flowmeter. *Meas. Sci. Technol.*, 23(4):045005, 2012.

- [94] C. Karcher M. Gramß. Calibration of a Lorentz force flowmeter. In *Proceedings of the 56th International Scientific Colloquium*, September 2011.
- [95] Daniel Martschoke. Automatisierung eines Versuchsstandes zur Trockenkalibrierung von Lorentzkraft-Anemometern. Master's thesis, Ilmenau University of Technology, 2012.
- [96] A. Alferenok, M. Werner, M. Gramß, U. Luedtke, and B. Halbedel. Numerical optimization of the magnet system for the Lorentz force velocimetry of electrolytes. *Int. J. Appl. Electrom.*, 38(2-3):72–92, 2012.
- [97] DIN. *Guide to the expression of uncertainty in measurement*. Deutsches Institut für Normung e.V., Berlin, 1 edition, 1995.

List of Figures

| | |
|---|----|
| 2.1. Principle of Lorentz force velocimetry. | 3 |
| 3.1. Isometric view of the FEM model. A tiny permanent magnet located at a distance of 85mm above a moving aluminum rod. The aluminum rod has a diameter of 80mm and length of 1000mm. The moving velocity is 10mm/s. | 18 |
| 3.2. Proposal 1: Permanent magnet with iron yoke. (a) Illustration of proposal 1 including the direction of magnetization. (b) Screen shot of the FEM model. The colored domains indicate magnitude of the magnetic induction. | 19 |
| 3.3. Results of the numerical simulation for proposal 1. (a) Illustration of the magnitude of the magnetic induction along the x-, y- and z-axes. (b) 3D plot of the Lorentz force for off-center position dx and dy of the moving rod. | 21 |
| 3.4. Proposal 2: Ring magnet. (a) Illustration of proposal 2 including the direction of magnetization. The ring is magnetized perpendicular to the x-y plane. (b) Screen shot of the FEM model. The colored domains indicate magnitude of the magnetic induction. | 23 |
| 3.5. Results of the numerical simulation for proposal 2. (a) Illustration of the magnitude of the magnetic induction along the x-, y-, and z-axes. (b) 3D plot of the Lorentz force for off-center position dx and dy of the moving rod. | 24 |
| 3.6. Proposal 3: Halbach cylinder. (a) Illustration of the magnetization pattern of a Halbach cylinder. (b) Screen shot of the FEM model. The colored domains indicate magnitude of the magnetic induction. | 26 |
| 3.7. Results of the numerical simulation for proposal 3. (a) Illustration of the magnitude of the magnetic induction along the x-, y- and z-axis. (b) 3D plot of the Lorentz force for off-center position dx and dy of the moving rod. | 28 |
| 3.8. Proposal 4: Halbach array. (a) Illustration of the magnetization pattern of a classical Halbach array as proposed by K. Halbach. (b) Screen shot of the FEM model. The colored domains indicate magnitude of the magnetic induction. | 29 |

| | |
|--|----|
| 3.9. Results of the numerical simulation for proposal 4. (a) Illustration of the magnitude of the magnetic induction along the x-, y-, and z-axes. (b) 3D plot of the Lorentz force for off-center position dx and dy of the moving rod. | 31 |
| 3.10. Sketch of the possible magnetization patterns for two single rings. (a) Magnetization pattern of Maxwell coil. (b) Magnetization pattern of Helmholtz coil. (c) Magnetization pattern of inverse Maxwell coil. | 32 |
| 3.11. Results of the optimization of proposal 2. The simulations are performed with a velocity of 10mm/s and an electrical conductivity of $22 \cdot 10^6 S/m$. (a) Magnetization pattern of Maxwell coil. (b) Magnetization pattern of Helmholtz coil. | 34 |
| 3.12. Sketch of the magnetization pattern of Halbach cylinders with different number of segments. (a) Halbach cylinder with 8 segments. (b) Halbach cylinder with 12 segments. (c) Halbach cylinder with 16 segments. | 35 |
| 3.13. Optimization of Lorentz force generation using Halbach cylinder magnet system. Three magnetization patterns with 8, 12, and 16 trapezoidal segments. | 37 |
| 3.14. Infrared photograph of a thick slab caster. It illustrates the thermal situation during the casting process. | 39 |
| 3.15. Thermal equivalent network for the cooling of the device. Heat fluxes from the SEN to the device and heat transportation. | 41 |
| 3.16. Temperature distribution of proposal 1: (a) Inner areas of the device. (b) Outer area of the device. | 45 |
| 3.17. Velocity distribution of proposal 1: (a) Velocity streamlines. (b) Velocity at the middle of the cooling system. | 46 |
| 3.18. Temperature distribution of proposal 2: (a) Inner areas of the device. (b) Outer area of the device. | 48 |
| 3.19. Velocity distribution of proposal 2: (a) Velocity streamlines. (b) Velocity at the middle of the cooling system. | 49 |
| 3.20. Temperature distribution of proposal 3: (a) Inner areas of the device. (b) Outer area of the device. | 51 |
| 3.21. Velocity distribution of proposal 2: (a) Velocity streamlines. (b) Velocity at the middle of the cooling system. | 52 |
| 3.22. Experimental setup for the investigation of spring constant and damping factor of a load cell. | 55 |
| 3.23. Force-deflection curve of a Siemens SIWAREX WL260 single point load cell. | 55 |
| 3.24. Investigation of the damping characteristics of a Siemens SIWAREX WL260 load cell. (a) Raw data of the measurement drawn all in one plot to demonstrate the good repeatability. (b) Decaying characteristic of the load cell plotted on logarithmic scale. | 56 |

| | | |
|-------|---|----|
| 4.2. | Analytical solution of the magnetic flux density (a) and the eddy current density (b) for several instants of time. | 66 |
| 4.4. | Transient response for several motion setups: (a) Step function. (b) Ramp. (c) Sinusoidal excitation. (d) Finite acceleration of the plate with $\beta = 1$ | 70 |
| 5.1. | Illustration of the two laboratory experiments. (a) Experiment for the determination of the response time of the LFF. A solid body is accelerated by gravity and passes the magnetic field. (b) Experiment for the determination of the calibration constant and sensitivity analysis. Here, a solid conductor moves with controlled motion. | 76 |
| 5.2. | Illustration of the experimental setup for investigation of the time-dependent Lorentz force. | 77 |
| 5.3. | Results of the experimental investigation of the time response of a Lorentz force flowmeter. The results were obtained using an aluminum rod with a diameter of 65mm and an electrical conductivity of $20.53 \cdot 10^6$ S/m. (a) Comparison between the theoretical velocity of the free fall of the body and the measured Lorentz force (b) Time-dependent calibration factor $k(t)$ | 79 |
| 5.4. | Results obtained by MATLAB Simulink using the determined material properties of the load cells and the solid body. (a) Simulink block structure. (b) Time response of the LFF after a jump in the moving velocity. | 80 |
| 5.5. | Magnet system used in the dry calibration experiment: (a) Illustration of the magnet system and the magnetization pattern. (b) Isometric view of the FE model. | 83 |
| 5.6. | Working flow of the OPC-Server structure for the calibration experiment. By courtesy of Daniel Martschoke [95]. | 85 |
| 5.7. | Results of the dry calibration experiment for aluminum and copper rods of different diameters: (a) Calibration curves for the aluminum rods. (b) Calibration curves for the copper rods. | 87 |
| 5.8. | Measured mass flux and cumulative mass compared with the prescribed value. (a) Mass flux of the 80mm aluminum rod moving with a velocity of 50mm/s. (b) Cumulative mass for several instants of velocity for the 80mm aluminum rod. | 88 |
| 5.9. | Correlation between Lorentz force and diameter of the rod for a moving velocity of 50mm/s. (a) Experimental results compared with the numerical results and polynomial fitting for aluminum. (b) Experimental results compared with the numerical results and polynomial fitting for copper. | 90 |
| 5.10. | Sensitivity analysis for off-center position of the moving aluminum rod ($d=80$ mm). The moving velocity is 50mm/s. (a) Results obtained by numerical simulation. (b) Results obtained in the experiment. | 92 |

| | | |
|------|---|-----|
| 6.1. | Photograph of the first prototype of a Lorentz force flowmeter for pipe flows. | 94 |
| 6.2. | View of the device after the first test run: (a) Top view of the base plate with outer ring. (b) Top view of the cover plate with inner ring upside down. | 96 |
| 6.3. | Curve progression of the temperature along the perimeter during the caster sequence. | 99 |
| 6.4. | Magnet system used for industrial test. A Maxwell Coil with distance $S=20\text{mm}$ (a) Screen shot of the numerical simulations. (b) Distribution of the magnetic field. | 102 |
| 6.5. | Calibration of the LFF for pipe flows: (a) Calibration of the single point load cells SCAIME AL15. (b) Measured calibration curve of the prototype of a Lorentz force flowmeter for pipe flows compared to numerical results. | 103 |
| 6.6. | Response surface of the Lorentz force for when the device is located in an off-axis position. The results are obtained by numerical simulations using a moving velocity of 10mm/s and an electrical conductivity of $22 \cdot 10^6 \text{S/m}$ | 104 |
| 6.7. | Calibration of the load cells of type Scaime AL15 in the prototype. . . | 106 |
| B.1. | Distribution of the magnetic field of a Helmholtz Coil for several instants of S . (a) $S=0\text{mm}$ (b) $S=10\text{mm}$ (c) $S=20\text{mm}$ (d) $S=30\text{mm}$ (e) $S=40\text{mm}$ (f) $S=50\text{mm}$ | 118 |
| B.2. | Distribution of the magnetic field of a Maxwell Coil for several instants of S . (a) $S=0\text{mm}$ (b) $S=10\text{mm}$ (c) $S=20\text{mm}$ (d) $S=30\text{mm}$ (e) $S=40\text{mm}$ (f) $S=50\text{mm}$ | 119 |
| B.3. | Results of the sensitivity analysis of the magnet systems. (a) Magnet with iron yoke (b) Ring magnet system | 120 |
| B.4. | Results of the sensitivity analysis of the magnet systems. (a) Halbach Cylinder (b) Halbach Array | 121 |
| B.5. | Results of the sensitivity analysis of the magnet systems. (a) Magnet with iron yoke (b) Ring magnet system (c) Halbach Cylinder (d) Halbach Array | 122 |

List of Tables

| | |
|---|-----|
| 4.1. Comparison of the nondimensional response time of the input velocity T_{98v}^* , the Lorentz force $T_{98\xi}^*$, and the Joule heat $T_{98\psi}^*$ for different instants of β | 72 |
| 5.1. Calibration factor k for aluminum and copper rods | 86 |
| 6.1. An overview of the maximal observed temperatures at various positions on the device. | 97 |
| 6.2. An overview of the temperatures observed during the caster sequence at different time steps. | 98 |
| A.1. Electrical conductivity of the aluminum rods [MS/m] | 113 |
| A.2. Electrical conductivity of the copper rods [MS/m]. | 113 |
| A.3. Diameter of the aluminum rods [mm] | 114 |
| A.4. Diameter of the copper rods [mm] | 114 |
| A.5. Properties of NdFeB [Source: www.supermagnete.de]. | 115 |

Nomenclature

| | |
|-------------------------------------|---|
| α | Heat transfer coefficient [$W/m^2 \cdot K$] |
| \bar{v} | Mean velocity [m/s] |
| \ddot{x} | Acceleration (second time derivative of the space coordinate x) [m/s^2] |
| δ_{mag} | Thickness of the permanent magnet [mm] |
| δ_{st} | Thickness of the iron yoke [mm] |
| \dot{m} | Mass flux [kg/s] |
| \dot{m}_{st} | Mass flux of liquid steel [t/min] |
| \dot{x} | Velocity (first time derivative of the space coordinate x) [m/s] |
| ϵ_0 | Electric field constant, permittivity of free space |
| η | Damping factor [$N \cdot /m$] |
| $\frac{\partial}{\partial t}$ | Partial derivative with respect to time [s] |
| $\frac{\partial}{\partial t}$ | Partial derivative with respect to time [s] |
| γ | Nondimensional shape factor |
| λ | Magnetic diffusivity [V/m] |
| λ_{hc} | Thermal conductivity [$W/m \cdot K$] |
| μ_0 | Magnetic field constant, permeability of vacuum |
| dA | Differential vector element of surface area A, with infinitesimally small magnitude and direction normal to surface [m^2] |
| ds | Differential vector element of path length tangential to the path/curve [m] |
| ϕ_{mag} | Magnetization direction of an Halbach cylinder expressed in terms of degrees [$^\circ$] |
| ρ | Free charge density (not including bound charge) [C/m^3] |
| σ | Electrical conductivity [S/m] |
| τ | Characteristic time constant |
| Δt | Time step [ms] |
| $\vec{\psi}$ | Nondimensional power dissipation |
| $\vec{\xi}$ | Nondimensional Lorentz force |
| \vec{B} | Distribution of the primary magnetic field [T] |
| \vec{B} | Magnetic flux density vector [T] |
| \vec{b} | Distribution of the secondary magnetic field [T] |
| \vec{D} | Electric displacement vector [C/m^2] |
| \vec{E} | Electric field vector [V/m] |
| \vec{F}_L | Lorentz force [N] |
| \vec{f}_L | Lorentz force density [N/m^3] |

| | |
|-----------------------|--|
| \vec{F}_{mag} | Magnetic force acting between magnets [N] |
| \vec{H} | Auxiliary magnetic field [A/m] |
| \vec{j} | Eddy current distribution [A/m ²] |
| \vec{Q} | Power dissipation [W] |
| \vec{q} | Volumetric power dissipation rate [W/m ³] |
| \vec{r} | Position vector [mm] |
| a_{max} | Maximal acceleration of the linear drive [m/s ²] |
| B_0 | Magnitude of the primary (homogenous) magnetic field [T] |
| c | Spring constant [N/m] |
| d | Thickness of a body [mm] |
| <i>DFG</i> | Deutsche Forschungsgemeinschaft |
| f | Frequency [Hz] |
| F_L | Magnitude of the Lorentz force vector [N] |
| F_{mag} | Magnitude of the magnetic force acting between magnets [N] |
| f_s | Sampling frequency [Hz] |
| j_L | Free current density (not including bound current) [A/m ²] |
| k | Calibration constant |
| L_c | Characteristic length scale |
| <i>LFF</i> | Lorentz force flowmeter |
| <i>LFS</i> | Lorentz Force Sigmometer |
| <i>LFV</i> | Lorentz force velocimetry |
| <i>MHD</i> | Magnetohydrodynamics |
| μ_r | Relative permeability |
| n | Speed of the electric drive [1/min] |
| R | Thermal resistance [K/W] |
| Rm | Magnetic Reynolds number |
| t | Time coordinate [s] |
| T_1 | Temperature of the SEN surface [°C] |
| T_2 | Temperature of the tundish surface [°C] |
| T_3 | Temperature of molten steel [°C] |
| T_4 | Temperature of the slag blanket [°C] |
| T_{98} | time needed to achieve 98% of the final value |
| T_{98}^* | Nondimensional reaction time |
| T_C | Curie temperature of a magnet [°C] |
| T_f | Core temperature of the cooling fluid [K] |
| T_S | Surface temperature [°C] |
| $v(t)$ | Time-depending velocity [m/s] |
| v_0 | Initial velocity [m/s] |
| v_{max} | Maximal velocity of the linear drive [m/s] |

Abschlusserklärung

Erklärung

(gemäß Anlage 1 der Siebten Änderung der Promotionsordnung der TU Ilmenau - Allgemeine Bestimmungen)

Ich versichere, dass ich die vorliegende Arbeit ohne unzulässige Hilfe Dritter und ohne Benutzung anderer als der angegebenen Hilfsmittel angefertigt habe. Die aus anderen Quellen direkt oder indirekt übernommenen Daten und Konzepte sind unter Angabe der Quelle gekennzeichnet.

Bei der Auswahl und Auswertung folgenden Materials haben mir die nachstehend aufgeführten Personen in der jeweils beschriebenen Weise entgeltlich/unentgeltlich geholfen:

1. **Herr Prof. André Thess** (Leiter Fachgebiet Thermo- und Magnetofluidynamik an der Technischen Universität Ilmenau: Fachliche Betreuung während der Promotionszeit.) → unentgeltlich
2. **Herr Stefan Buhl** (Studentische Hilfskraft an der Technischen Universität Ilmenau: Unterstützung bei der numerischen Simulationen der Kühlsysteme mit ANSYS CFX. Insbesondere die Implementation der von mir vorgegebenen Modelle und Randbedingungen in ANSYS CFX.) → unentgeltlich
3. **Herr Daniel Martschoke** (Masterarbeit und Studentische Hilfskraft an der Technischen Universität Ilmenau: Unterstützung bei der Automatisierung der Kalibriereinrichtung für Lorentzkraft-Anemometer.

Insbesondere bei der Programmierung der Motorsteuerung.) → unentgeltlich

4. **Universitätswerkstatt** (Fertigung von Bauteilen für den Prototyp des Lorentzkraft-Anemometers anhand von mir erstellter technischer Zeichnungen.) → unentgeltlich
5. **Editage - English Language Editing Services** (Sprachkorrektur; Ausschließlich Bearbeitung von Rechtschreibung und Grammatik. Es wurden **keine** inhaltlichen Änderungen, Ergänzungen oder weitere Beiträge durch die Editoren vorgenommen.) → entgeltlich

Weitere Personen waren an der inhaltlich-materiellen Erstellung der vorliegenden Arbeit nicht beteiligt. Insbesondere habe ich hierfür nicht die entgeltliche Hilfe von Vermittlungs- bzw. Beratungsdiensten (Promotionsberater oder anderer Personen) in Anspruch genommen. Niemand hat von mir unmittelbar oder mittelbar geldwerte Leistungen für Arbeiten erhalten, die im Zusammenhang mit dem Inhalte der vorgelegten Dissertation stehen.

Die Arbeit wurde bisher weder im In- noch im Ausland in gleicher oder ähnlicher Form einer Prüfungsbehörde vorgelegt.

Ich bin darauf hingewiesen worden, dass die Unrichtigkeit der vorstehenden Erklärung als Täuschungsversuch bewertet wird und gemäß §7 Abs.10 der Promotionsordnung den Abbruch des Promotionsverfahrens zur Folge hat.

Ilmenau, den 19.12.2012

Christian Weidermann